University of Sussex

Towards a portable single ion optical clock

Callan M. Jobson

Submitted for the degree of Doctor of Philosophy
University of Sussex
Sep 2020

Declaration

I hereby declare that this thesis has not been and will not be, submitted in whole or in part to another University for the award of any other degree.

Signature:

Callan Mckenzie Jobson

28th June 2021

UNIVERSITY OF SUSSEX

Callan Mckenzie Jobson, Doctor of Philosophy

Towards a portable single ion optical clock

Summary

Atomic clocks based on optical transitions have been shown to achieve the most precise measurement of time to date, far exceed the current gold standard of microwave atomic clocks. With current capabilities of Microwave clocks starting to bottle neck systems such as global navigation constellations, telecommunications networks and reference systems for scientific research. Optical clocks would allow these systems to continue to develop giving far superior timing solutions. However, current optical clocks have large spatial footprints, high power consumption, and complex operational procedures. For this reason they have yet to be deployed outside of the scientific community.

The work in this thesis sets out to address these issues by utilising advancements in fibre optics. The integration of fiber optics allows the spatial footprint to be drastically reduced. Fibers integrated directly into an ion trap eliminates the need for optical windows and the surrounding optics needed for beam delivery, thus also reducing the sensitivity to vibration. Alongside this a highly compact laser system utilising commercial developments in fiber optic components is realised. This laser system contains all the lasers needed to photo-ionise, cool, state detect and quench the ion, all within the volume of four litres. Furthermore this laser system is shown to photo-ionise, cool and quench a trapped ion without active feedback. This is ongoing work towards a portable optical atomic clock housed inside a 4U rack mounted unit.

Acknowledgements

The work in this thesis was done in the ITCM group at the university of Sussex. It was done under the supervision of Professor Matthias Keller between 2015 and 2020. I am extremely grateful to everyone who has supported me over this time, from my colleagues and friends to the lunch ladies in the bridge.

First and foremost I would like to thank Professor Matthias Keller for giving me this opportunity and teaching me over these years. His leadership, guidance, and patience throughout my PhD made learning what it should be, fun!

To the ITCM group of old and new, I would like to thank you all for making this experience as enlightening as it was. Xavi thank you for your constant support over the time we worked together, for your friendship, and for putting up with everything along the way. You really made it a laugh. Nathan you may have only been with us for six months, but you have had a lasting impact. I wish you and your family all the best. To Costas and your sofa sized heart. I love you, never change. Sam thank you for all the fun conversations from scalable quantum computing to the musical stylings of Armin van Buuren. I wish you all the luck with your PhD and the future beyond. Laura I wish you all the best with your PhD and hope your next position will not be in a lab by your self! Tom, good luck and enjoy the Schnitzel! Hamzah good luck with your future path. Corentin, David and Traverse good luck with your PhDs. To everyone that came before (Samir, Amy, Markus, Jack, Hiroki, Ezra, Gurpreet, Arijit) thank you for making the lab enjoyable whilst you were there. Finally I would like to thank Alan Butler for the discussions, insight into machining and approachable nature. See you at the square and compass!

To all my climbing friends, thank you for giving me a place to de-stress and refocus. There are so many of you I wish to thank, but not enough space to write. To George and Elaina, thank you for your space to write and laugh.

Simone Lang. I cannot ever put into words how grateful I am for all your support of the years, especially over these last difficult months. You have broken the darkest skies with the sunlight of your smile.

To my Dad and Wendy, this is for you.

Contents

List of Tables

List of Figures

Chapter 1

Clocks, what and why they tick

Time: *indefinite continued progress of existence and events in the past, present, and future regarded as a whole.* - The Oxford English Dictionary

Time seems to only flow in one direction from past to present to future. This concept can be formulated in entropy and how disorder spreads. The nature of this linear progression along time giving rise to change gives fundamental insight into the inner workings of the world. This makes time critical to measure. To measure a system's evolution in time we must take information before and after an event and compare. For this a reference of time must be established akin to a ruler. This is called a clock.

A clock, at its most basic, consists of a reference, an oscillator and a counter. The reference defines the unit of time so that every clock is consistent, this is based on a natural phenomena that remains predictable (earth's rotation, solar cycle, atomic resonance). The oscillator acts as the comb of lines on times ruler giving defined steps of measurement (seconds, minutes, hours, days..). Finally the counter indicates at which point along times ruler it is (13:34 02/04/2020). This is how time is measured from its inception till today, with the key difference being the speed and accuracy of the constituents has changed as technology has progressed. The clock gives us the tool to understand, predict and react.

Clocks have given us the ability to test our understanding of the laws of nature and its boundaries. The measurement of time allows us to circumvent the globe and the universe. Clocks are the backbone of the digital age allowing humanity to cheat geographic boundaries and bring the knowledge of our entire species into the palm of our hands. With every step forward in the ability to gauge time accurately, make it more accessible, and disseminate it to others, humanity has progressed. This is why clocks have been at the

forefront of development for 8000 years from basic lunar cycles to its current pinnacle of optical atomic clocks[5].

1.0.1 A brief history of (atomic) time

The foundations of using natural vibrations of atoms as a time standard dates back to James Clerk Maxwell[6] in 1873 where Maxwell suggested that *"A more universal unit of time might be found by taking the periodic time of vibration of the particular kind of light whose wavelength is the unit of length"*. Lord Kelvin (attributed to Maxwell) championed this idea in 1879[7], going further by linking the natural vibrations of light with the natural spectra of atoms which would give a *"perfectly inverible unit of length"*. But at this time there was no way of realising such an experiment. It was not taken up seriously until Isidor Isaac Rabi made progress in the field of magnetic resonance[6, 8] during which he explored the idea of the interaction between an atomic beam and a microwave field. The first working atomic clock used an ammonia absorption line at 23870.1 MHz, it was designed by Harold Lyons in 1949 and achieved an uncertainty of two parts in 10^8. At the time quartz oscillators were at approximately one part in 10^8[8]. Although the ammonia clock did not exceed the day's standard, it worked as a proof of concept for later experiments.

The real breakthrough came with caesium in 1955. When Louis Essen and Jack Parry[9] developed a caesium clock that was one part in 10^9. This was based on Rabi's magnetic resonance techniques showing that for the first time celestial bodies need not be the ultimate reference. The international system of unit (SI) of time in 1955 was defined by a quartz oscillator referenced to the earth's rotation. It was well understood that the rotation of the earth was not as accurate as that of the solar orbit, but realising a second in the period of the solar orbit meant quartz oscillators were at their very limit. The question of what would be the best reference of time was ever changing but since the invention of the clock it had always relied on celestial periodicities: Solar orbit, lunar cycle, day night cycle, but celestial bodies periodicities become messy the more accuracy is demanded. Along with this, the inability to compare like systems as they are unique to our observations isnt possible. Atoms offered a reference that was not only repeatable but inherently used higher frequency of operation. The work of Maxwell, Kelvin, Rabi, Lyons, Essen and Parry all cumulated in 1967 with their combined vision of the second being redefined by an atomic reference. The 9192631770 oscillations of the hyperfine splitting in caesium 133[10]. This was the first time the second was defined to a non celestial action and it remains in this definition today.

Microwave caesium standards dominated precision measurement for over 50 years. The techniques being refined and the changes in the hardware moving forward steadily increasing the accuracy of the standard. Today caesium is still used but the way it is probed has been upgraded. Caesium fountains were the biggest leap in the caesium standard. The fountain increased the interrogation time of the atoms allowing for more accurate measurements of the hyperfine splitting. These fountains act as the primary reference for all meteorology institutes across the world with accuracies as low as 2.5 parts in 10^{16}[11]. Most of the caesium fountains are bespoke to the research institute they originate from making all the fountains ever so slightly different. A comparison allows each system's understanding to be tested as well as our combined understanding of what constitutes the SI second to be realised. Taking all the clocks and creating a weighted average acts to smooth out local uncertainties, thus building an ultimate ruler for which each standard can be compared. This weighted average is achieved by the Bureau International des Poids et Measures (BIPM) in Sevres, France[12]. This signal is disseminated in the form of two timing standards International Atomic Time (TAI) and Coordinated Universal Time (UTC). TAI acts as an unchanged weighted mean of the caesium standard defining the SI second. UTC has the same time base as TAI but is adjusted to the rotation of the earth integrating leap seconds[13].

Microwave clocks are not the pinnacle of time keeping. Optical transitions in atoms have been the next logical progression, with higher frequencies offering the possibility to access more stability. Work on developing an optical oscillator referenced to an atom has been ongoing since the early 1960's, with the development of the laser first published by Theodore Maiman[14]. With work on the laser driven by the demand for it to be smaller, to have a higher output and to maintain longer coherence, the laser became a useful tool for scientists to perform optical spectroscopy. In the 1970's a series of groups started to produce the first realisation of a laser stabilised to an atomic reference in the form of Iodine stabilised helium neon laser[15, 16, 17]. The work by Wolfgang Paul in the 1950s on molecular beam physics evolved into ion trapping[18]. Ion trapping was championed in the 1970's by two groups, one led by David Wineland and the other by Hans Dehmelt. These two groups pioneered laser cooling of trapped ions with Dehmelt, Paul and Wineland receiving Nobel prizes for their work[19, 20]. One of the bigger problems with optical clocks was the inability to use standard electronics to count the periods of the optical frequency. Since the 1970's, the main was to utilised a complex cascade of second harmonic generation processes[21] which was incredibly complicated and hard to

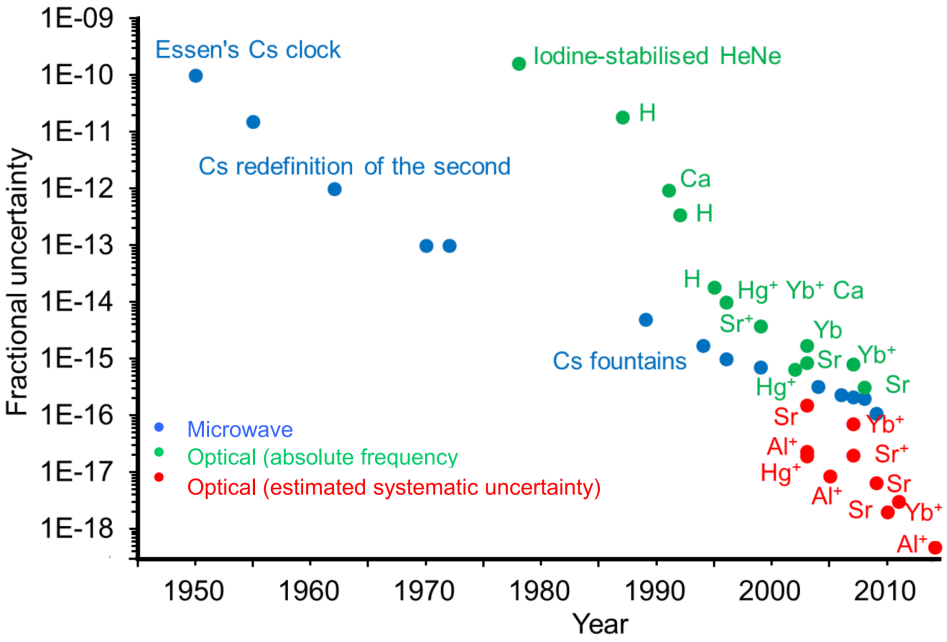

Figure 1.1: Atomic clock progress over the past 70 years[1].

maintain. This all changed with an invention by Hall and Hänsch in 2000[22] which five years later earned them a Nobel prize in physics[23], the frequency comb[22]. This allowed the optical spectrum to be geared down into the microwave domain relatively simply and reliably. This was key to making optical clocks a competitor to the much more reliable microwave clocks. Optical clocks progression has shown a much steeper trend than that of microwave clocks. This has lead them to exceeded microwave standards in performance with fractional uncertainties currently less than one part in 10^{18}[24] (see figure 1.1). With optical clocks playing a role in UTC and with their ever maturing technology brings them closer to becoming the new definition for the SI second[25][1].

1.0.2 Accuracy and stability

Accuracy and stability parametrise an atomic clock's performance. The accuracy of the clock is how much the average frequency is offset to the true value of the frequency. This deviation is rooted in the combination of all the different frequency shifts that act to differ the clock's frequency away from the true value. For an optical atomic clock these shifts are influenced by the atoms coupling to: electric fields, magnetic fields, motional induced shifts, gravitational fields, collisional and system noise effects[3]. The true value of the inaccuracy comes from the uncertainty on each of these shifts. With each shift that can be

[1] if only we could decide on which species to use...

understood, measured and compensated, the clocks accuracy wont be effected. The error for which these shifts are compensated ultimately defines the inaccuracy of the clock.

The stability of the clock is how much the frequency changes over time. Drifts and noise are parasitic to the stability of the clock and are sought out to be reduced. If a clock's stability was given as $1 \cdot 10^{-9}\ s^{-1}$ its signal would differ from the average value by no more than one nano second every second. If we were to take this and average the system over a long period of time we could reduce this number, however that isn't the entire picture. Drifts and noise couple to the system in different time intervals. This is why stability of a clock is quoted over a time period $1/\sqrt{\tau}$ where τ is the period of time averaged over. The stability of a clock is plotted against an increasing τ, with this plot exposing some key components of the drift and noise of the clock. The different slopes of the Allan deviation indicate certain types of noise coupling to the clock (see figure 1.2)[2]. A slope of (-1) shows white phase noise or flicker phase noise, which is commonly caused by electronic noise on detection/feedback loops. (-0.5) is characteristic of white frequency noise. (0) is due to flicker frequency noise and this indicates the noise floor. (0.5) random walk frequency noise. The clocks stability improves with greater averaging time until it reaches the noise floor after which the stability gets worse. This can be due to the oscillators physical environment changing. The total fractional instability of an atomic clock can be expressed as[26].

$$\sigma(\tau) = \frac{\Delta\nu}{\nu}\frac{\eta}{(S/N)}\sqrt{\frac{T}{\tau}} \tag{1.1}$$

Here $\Delta\nu$ is the linewidth of the atomic transition, ν is the resonator frequency, (S/N) is the signal to noise ratio, T is the probe time, τ the total averaging time, and η is dependent on the probing technique called the numerical constant of order unity. From this equation it can be seen how influencing certain aspects of the clock can be used to reduce the overall instability. For example increasing the signal to noise reduces the overall instability, which brings out a key design optimisation parameter. From this equation it can also be seen how optical frequencies benefit over microwave frequencies. By increasing ν with relatively similar $\Delta\nu$, the overall instability reduces. Both the accuracy and the fractional frequency instability project the clocks performance.

1.0.3 How an optical clock ticks

Optical atomic clocks consist of the same three building blocks that make up every clock but with more accurate constituents[3] (see figure 1.3). The oscillation is generated by an ultra stable laser which is coupled to an atomic reference. The atomic reference is based

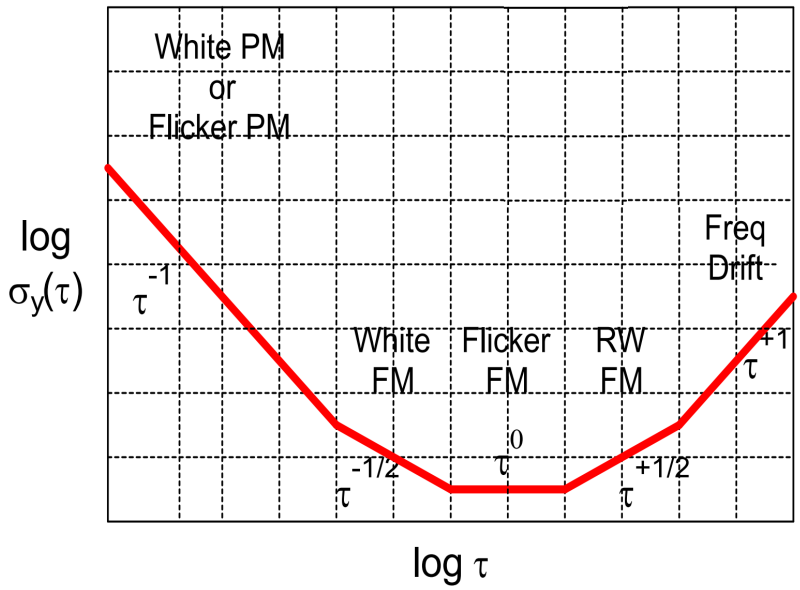

Figure 1.2: This shows a generalised Allan deviation plot, highlighting the different types of noise and how they are indicated by the Allan deviations slope[2].

on an electronic transition with comparable stability of the laser (around one hertz). The ultra stable laser is tuned to resonate with the atom's electronic state shelving the electron, then using a series of other laser acts to read out whether this shelving was successful. A feedback loop is implemented based on the result to steer the frequency and maintain resonance with the atom. This couples the laser to the atom, taking the highly stable atomic transition and coupling it to the short term stability of the laser. Finally, the laser's periods are counted using a frequency comb. This takes the optical $\approx 10^{15} s^{-1}$ frequency of the stabilised laser and gears it down to the microwave domain whilst maintaining the accuracy. Microwaves can be used via standard electronics allowing broad distribution and use for the clock.

Clock laser

Current ultra stable lasers can exceed the line width of most atomic species reference transitions (clock transitions) with short term stabilities down to less than one hertz[27] [2]. This is achieved by frequency locking a moderately stable laser (MHz-kHz in a ms) to a ultra low expansion (ULE) high quality factor optical cavity[28, 29]. The optical cavity acts as an extremely narrow-band optical filter. With the laser coupled to the cavity the frequency is tuned into resonance, a transmitted or reflected signal from the cavity is used in conjunction with a Pound Drever Hall locking method[30] to stabilise the laser.

[2] exception being the ytterbium ion octupole transition

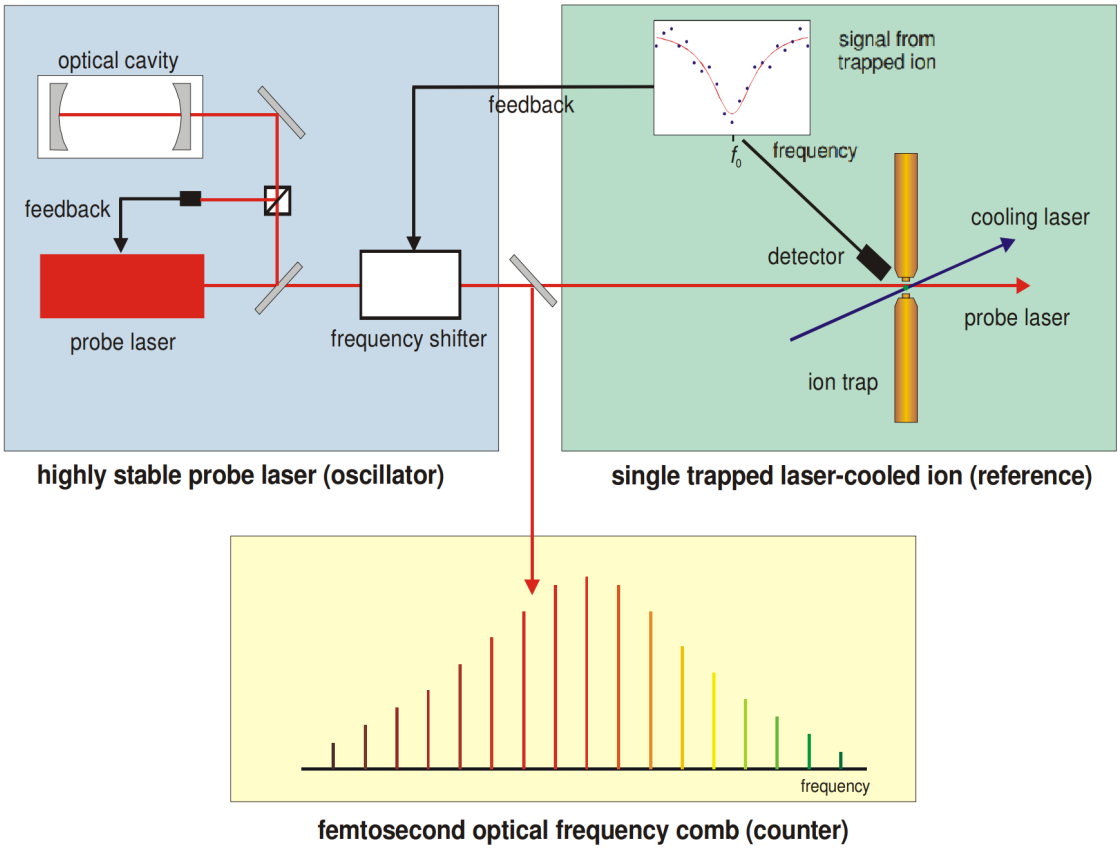

Figure 1.3: *Elements of an optical atomic clock, and the relationship between them. (This illustration is for the case of a trapped ion optical clock, but similar relation exists between the subcomponents of a clock based on cold neutral atoms.)*[3].

This transfers the short term stability of the optical cavity to the laser. ULE cavities drift, usually achieving a noise floor in a few seconds of averaging and then begin to show random walk frequency noise[31]. This rise in instability comes from four key areas: electronic effects from the locking, acoustic and systemic vibrations transmitted through the cavity due to the environment, thermal noise on the cavity length and Brownian noise on the mirror coatings. Even with modern compensation methods these still play the biggest effect on the clock lasers stability.

Atomic reference

A big debate in optical clocks has been in the atoms and what state to use them in. There are two types of approaches atomic ensembles and single ions, both with an abundance of promising species.

Atoms can be trapped in large optical lattices that confine each atom via the dipole interaction along a three dimensional interference pattern. The abundance of atoms allows one shot read out making the signal to noise vary favourable. However the dipole interaction is extremely weak and trap lifetimes are in the low seconds worth of confinement. These systems require multiple different loading and cooling stages with complex running procedures[32]. Atoms trapped in an optical lattice are susceptible to a number of shifts[33, 34, 35]. Zeeman shifts, first and second order depending on whether fermionic or bosonic isotopes are used. Stark shifts in the form of black body radiation shifts, dc shifts due to stray charges, ac stark shifts from the probe beam and lattice lasers. First and second order Doppler shifts. Tunnelling effects, collisional effects and gravitational red shifts. All of these have to be measured and compensated for.

A single trapped ion offers a near perfect physical system. Ions are trapped using the coulomb interaction, allowing for much higher confinement with trap lifetimes in excess of months. This makes ions much less complicated to work with in comparison to trapped atoms. The down side of single ions is they require repeatable measurement cycles to gain a statistical significant measurement of the laser resonance signal. There is a finite speed for which an ion can be detected and then reset. This bounds the speed in which a signal can be acquired and thus feedback to the laser. The systematic shifts present an ion trap[36, 37] are Zeeman shifts due to external magnetic fields. Electric quadrupole shift, due to coupling of the electric quadrupole moment of the ions state with any residual electric field at its position. Second order Doppler shifts due to residual micro-motion and thermal motion of the ion. Stark shifts from micro-motional induced effective field

perturbation, black body radiation from the surrounding structure, and ac stark shifts from the clock laser and also can occur from the needed lasers used for cooling and state readout.

Candidates for each system tend to be judged on their susceptibility to systemic shifts, their translational stability, and their complexity to implement. For example aluminium ion clocks are the current holders of the most accurate measurement[24] but due to aluminium not having an accessible cooling transition magnesium must be used to sympathetically cool the aluminium ions. This makes the trapping and the state detection more complex.

Optical frequency combs

Optical frequency combs offer a tool that allows for relatively[21] simple gearing of the optical periods into the more commonly used microwave domain[22]. A frequency comb generates an equally spaced comb of laser frequencies formed commonly by mode locked laser. This tool allows not only multiple different frequency to be compared (if within the span of the comb) but with tooth spacings of the frequency comb tending to be in the microwave domain, this allows a mapping of the stability on the optical frequency to be geared to the microwave domain. This gives clocks the tool to effectively count the periods of the atomic referenced laser.

1.0.4 Why go smaller

In the modern age, time is at the heart of technological development and scientific discovery. Technology strives to be faster, smaller, lighter, and consume less power. Where as science always strives for the uncompromisingly fastest, the highest resolution, the closest to the boundaries of what is possible. Atomic clocks are relied upon for both, scientific endeavours and the commercial world. Atomic clocks can be found in global navigation, resilient communication, autonomous vehicles (land sea and air), gravitational sensing, quantum communication and computation. All of these fields would benefit from more accurate commercially available atomic clocks.

With the demand for faster and higher bandwidth communication, the accuracy requirements for those clocks goes up. An example of this is with telecommunication systems, these rely heavily on global navigation satellite systems (GNSS) backed up with best market available microwave caesium standards for timing synchronization. GNSS is reliant on atomic clocks, for example the Galileo constellation is at the technological forefront of

GNSS satellites. Galileos timing signals are synchronised by a rubidium reference coupled to a hydrogen masers supported by ground based steering by UTC[38, 39]. For current generations of wireless communication (2G, 3G, 4G, 5G) these backup caesium microwave clocks timing is sufficient, but for next generations with more masts, higher speeds and higher bandwidth requirements, these backup systems will struggle to cope in the case of a GNSS outage[40]. The need for commercially available portable high accuracy optical atomic clocks could be the solution.

GNSS has been revolutionary for navigation. It is so widely used today and relied upon but it is unprotected in the way that it is disseminated. Satellites are prone to jamming and spoofing[41, 42]. To solve this a more robust constellation could be launched or the current ones upgraded, but this is an expensive task. The use of a ground based system would allow for more dynamic network more easily upgradable and more resilient. These systems would benefit from the highest accuracy in time keeping solutions.

The forefront of scientific research is underpinned by the available technology of its time. Commercially available optical references would allow for easier access to highly stable lasers needed in quantum computing, gravitational sensing, radio astronomy[43].

The next generation of portable atomic clocks is needed. The obvious step is taking the most accurate atomic clocks and work to make them smaller, more robust and fully autonomous, so everyone can benefit from this current pinnacle in precision.

1.0.5 This Thesis

In this thesis I set out the foundations for a portable optical atomic clock based on a single calcium ion. A portable optical atomic clock is realised by reducing the free space of the large lab sized systems and incorporating recent progress in fiberoptic technologies that allow the free space of a normal atomic clock to be heavily suppressed. This thesis goes through the design, fabrication and preliminary testing of the highly compact laser system required to trap and cool a single ion. Furthermore the design and fabrication of a fully fiber integrated monolithic ion trap is realised within the volume <2l. These developments are key stepping stones towards a highly portable rack mounted (4U) optical atomic clock. The design aim for the entire project is to develop a compact portable optical clock that is robust for practical real world use. This clock being less than 20 liters in volume, less than 100 kilograms in weight, consume less than 200 watts of electrical power, and have a fractional frequency uncertainty less than one part in 10^{14}. The solutions have been developed by my self, Dr Xavier Fernandez Gonzalvo, Dr Nathan Gemmell and supervisor

Professor Matthias Keller.

Compact fiber integrated laser system: The laser modules and all the electronics were designed by Professor Keller. I have built the compact laser modules utilising commercially available components for use in the laser system. The final laser system was built by Dr Gonzalvo. This laser system contains all the needed lasers and control electronics to photo ionise trap and cool the ion. This system is housed in a package that is less than two litres. Currently, there is no comparable laser system as compact commercially available.

Laser system test: I tested the laser modules for short term stability and medium term drifts with Dr Gonzalvo taking the long term data of the laser modules and the full laser system. We managed to load, trap and cool an Ion exclusively with this laser system.

Fiber integrated Ion trap: Using experience we gained in our previous design and build that under went three iterations of development. We worked on a complete redesign of the trap structure where by we used new methods for beam delivery and electrode fabrication and alignment allowing a monolithic ion trap to be realised. This trap has been fabricated and is under test. This work was done by Dr Gonzalvo, Professor Keller, and myself.

Noval fiber feedthrough: I worked on the research and development of a compact adjustable fiber feedthrough that allowed for a UHV seal on fiber optics that didn't rely on epoxies. These feedthroughs unlocked the ability to have in vacuum deliverable fibers for beam delivery and florescence collection systems for the compact ion trap. My work was based on previous developments of the feedthroughs made in the ITCM group

The thesis is broken into the following chapters:

Chapter 2 gives a theoretical break down on the principles of ion trapping and laser cooling. As well as going through the calcium ion, why we chosen to use it and what systematic shifts it suffers from.

Chapter 3 Shows the design and fabrication of the fiber integrated laser system, with results of its stability and use in trapping of a single ion.

Chapter 4 Breaks down the design and fabrication of the fiber integrated ion trap highlighting the fabrication techniques.

Chapter 5 Concludes the results and current progress of the project comparing it with the overall project goals and gives a breakdown on what the future of the system holds.

Chapter 2

The theory of trapping & cooling a single Ca^{40+}

The work described in this thesis uses a single calcium-40 ion trapped in a RF "Paul" trap at its core. In this chapter the theoretical background for ion trapping, laser cooling and a breakdown of the calcium-40 ion is described. This chapter is broken down into several sections. A description of Ion trapping with time varying electric fields, how this gives rise to certain types of Ion motion and how a realistic trap differs. An overview of a classical field interacting with a 2-level bound system showing how cooling can be realised under several slightly different techniques and a calculation of the Doppler cooling limit for calcium. The calcium-40 ion level scheme is shown with all the relevant transitions for clock operation, after which the systematic shifts are highlighted and there relative impact on the potential system.

2.1 Ion trapping

There are two common version of ion traps in use today[44]. The Penning trap (named after Frans Michel Penning by its inventor Hans G. Dehmelt) for which static electric and magnetic fields are superimposed to trap ions in an orbit. The Paul trap (named after its inventor Wolfgang Paul) where time varying electric fields are used to create a pseudo harmonic trap. For there work the 1989 nobel prize was awarded to both Paul and Dehmelt[19].

2.1.1 Paul trap

To trap an ion the system will have to satisfy that a small perturbation of the particle from the systems center would result in a restorative force being applied back. This can be understood that the traps force would point towards the equilibrium position. This results in the total flux of the field around the equilibrium position being negative (known as a sink). Considering a three dimensional harmonic potential ϕ in Cartesian coordinates.

$$\phi(x, y, z) = \phi_0(\alpha x^2 + \beta y^2 + \gamma z^2) \tag{2.1}$$

Where ϕ_0 is the potential amplitude and α, β, and γ are individual constants. Solving using Laplaces equation $\nabla^2\phi = 0$ requires $\alpha + \beta + \gamma = 0$. This shows that generating a local minimum in 3 dimensions where $\alpha+\beta+\gamma > 0$ with static fields is forbidden. This is known as Earnshaws theorem[45]. The simple 3D solution to the Laplace equation where $\alpha = \beta = 1$ and $\gamma = -2$ is stable in the x and y dimensions and is unstable in z. This type of potential is known as a saddle potential. The way this anti-trapping is overcome is by using a non-static field for which the general potential should look like

$$\phi_0 = U_{dc} + V_{ac}cos(\Omega t) \tag{2.2}$$

The potential is composed of a static part and a time varying part. Where U_{dc} and V_{ac} are amplitudes of the DC and AC parts respectively and Ω is the drive angular frequency. The use of the time varying potential allows a coupling of the anti trapping dimension and one of the trapping dimensions. As the potential is varied the saddle potential is inverted making what was anti trapping into trapping and vise versa. This creates an effective harmonic potential.

Paul traps electrode configuration define the potential in which the ions are trapped and these are not limited to Pauls original design. Paul traps have a wide verity of electrode geometry's. Electrode geometry's have been optimised to allow for trapping long ion strings[46], single ions[36, 37], structures that allow coherent shuttling of ions through complex paths[47]. These systems have all originated from the trap considered by Paul which gives radial symmetry about the trap axis. Pauls original trap consists of two facing hyperbolic electrodes where their focuses are aligned to the center of the geometry these are called *end cap electrodes*. A third electrode which is a hyperbolic ring, surrounds the other end cap electrodes with its focus also aligned to the center of the geometry. A time varying electric field is applied to the end cap electrodes and the ring electrode is held at ground potential. The potential in such a hyperbolic trap is given by

$$\phi = \frac{\phi_0}{r_0^2 + 2z_0^2}(r^2 - 2z^2) \tag{2.3}$$

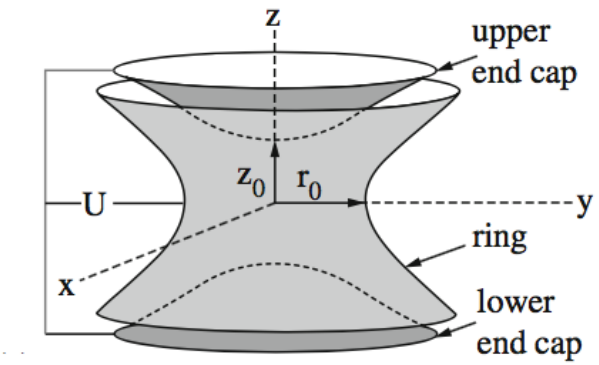

Figure 2.1: An example of Pauls original design. Consisting of 2 end cap electrodes facing each other with a ring electrode surrounding them. Coordinate space with x, y, z axis highlighted and $\boldsymbol{r}$. U is the oscillating potential applied to the electrodes. This original figure is from[4].

2.1.2 The Mathieu equation

The equation of motion of a charged particle in such a potential is described by:

$$m\frac{d^2i}{dt^2} = \frac{2e}{r_0^2 + 2z_0^2}(U_{dc} + V_{ac}cos(\Omega t))i \tag{2.4}$$

Where $i = \{r, z\}$ indicates the ions position in each dimension. This equation has the form of a Mathieu equation

$$\frac{d^2x}{d\tau} + (a - 2qcos(2\tau))z = 0 \tag{2.5}$$

The Mathieu equations has stable solutions for certain values of a and q. The solutions for which are not derived in this text but can be found in[48]. Figure 2.2 highlights the lowest stability region for which values of a and q must satisfy. There are further areas where stability can be reached but these become more complex to implement. In this work the lowest stability region is used.

Transforming equation 2.4 into the form above, with $\tau = \Omega t/2$ gives parameters a and q

$$a_r = \frac{-8eU_{dc}}{m\Omega^2(r_0^2 + 2z_0^2)} \qquad q_r = \frac{4eV_{ac}}{m\Omega^2(r_0^2 + 2z_0^2)} \tag{2.6}$$

$$a_z = \frac{16eU_{dc}}{m\Omega^2(r_0^2 + 2z_0^2)} \qquad q_z = \frac{-8eV_{ac}}{m\Omega^2(r_0^2 + 2z_0^2)} \tag{2.7}$$

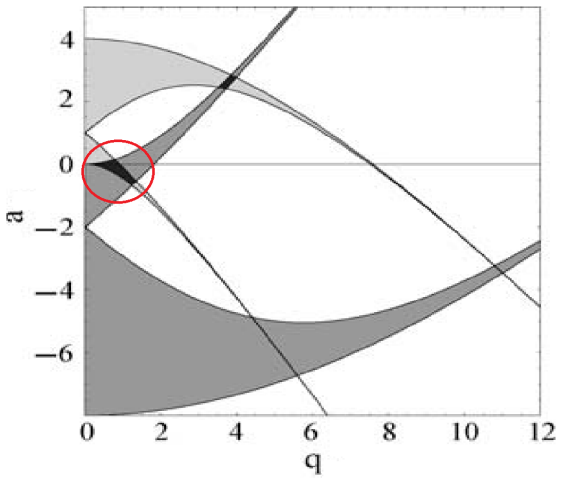

Figure 2.2: Shows the stability region for an ideal Paul trap. The red circle highlighting the first stability region. This original figure is from[4].

2.1.3 Secular frequency and micromotion

Taking $(a_i, q_i) << 1$ The ions position can be shown to first order approximation as

$$i(t) = A_i cos(\omega_i t)\left[1 - \frac{q_i}{2} cos(\Omega t)\right] \tag{2.8}$$

Where A_i is the amplitude of displacement of the ion in direction i. A is taken to be small. Equation 2.8 is broken down into two terms. The first, time dependent solely on ω_i which is referred to as the secular frequency.

$$\omega_i \approx \frac{\Omega}{2}\sqrt{a_i + \frac{q_x^2}{2}} \tag{2.9}$$

The secular frequency is smaller than the trap drive frequency when working within the first stability region. The other term in equation 2.8is much smaller due to its dependence on q_i which is taken to be $q_i \ll 1$. This term is driven at the trap drive frequency and can be seen to interact stronger as the ions is displaced from the trap center, in this case by the secular motion. This small motion driven by the trap drive and dependent on the ions displacement caused by the secular motion is called its intrinsic micromotion.

Consider now the ion is trapped but a static field is present. The ions rest position is now displaced due to this static field modifying the ions dynamics. This additional static field can be caused due to stray charges forming around the trap geometry called patch potentials.

$$i(t) = (A_{0_i} + A_i cos(\omega_i t))\left[1 - \frac{q_i}{2} cos(\Omega t)\right] \tag{2.10}$$

Where

$$A_{0_i} = \frac{eE_{dc} \cdot u_i}{m\omega_i^2} \tag{2.11}$$

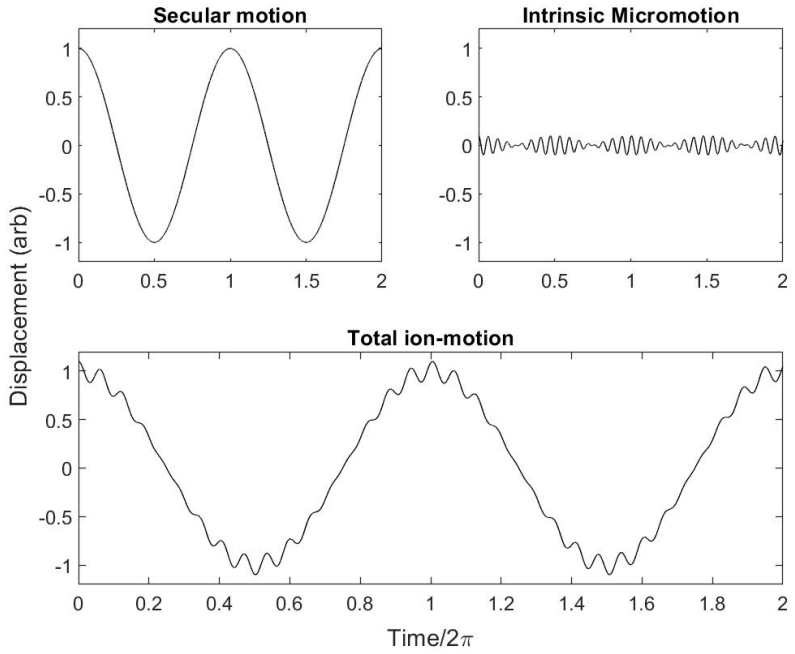

Figure 2.3: Modelling the ions motion. This figure highlights the 2 components of the ion motion. Top left shows a plot of the secular motion driven periodically in ω. Top right shows the intrinsic micromotion (the fast oscillation) contained within the slower secular motion. Bottom shows the total ion motion. For all plots $q = 0.2$.

This additional motion is driven again at the trap drive frequency and interacts stronger when displaced further from the trap center but this motion is only dependent on static electric field that the ion sees. This is referred to as excess micromotion. Ion motion is generally not wanted as this broadens the ions transitions. Excess micromotion can be compensated by applying a local static field to counteract the unwanted field and moving the ion back to its trap center.

2.2 Atom light interactions

For the use of a high precision reference the underlying fundamental properties of the ion want to be exploited. Meaning the ion wants to be considered with as little to no distortion to its fundamental dynamics. In the ideal case, the ion would be isolated from unmeasurable perturbations that would distort the transition. In reality a system is designed to reduce these interactions or measure them so the uncertainty of the transition is as small as possible.

The most influential interaction is the ions motion or temperature. The ions motion acts to shift on short time scales and broaden in longer scales the natural transition. To get

the most out of this system the motional state must be reduced, this is achieved by laser cooling. Laser cooling was investigated by two separate groups Hansch and Schawlow[49], and Wineland and Dehmelt[50] in 1975. It was later shown experimentally in 1978 by Wineland, Drullinger and Walls[51]. The principle is to reduce the velocity of the atoms via the use of radiative forces. For Doppler cooling this involves using a probing laser that is detuned from the ions natural transition. The ions electronic excitation can only occur when its motional induced Doppler shift brings the laser into resonance. This causes a coupling between its motional state and its electronic state. This can be used and exploiting spontaneous emission reduce the ions thermal motion drastically the limit of which is proportional to the transitions linewidth. Further variations of this technique have been shown to cool ions down to less than a micro kelvin producing Bose-Einstein condensates[52].

The detail of laser cooling is embedded in how the ion interacts with the perturbating electromagnetic field. These atom-light interactions are at the core of any optical atomic or ionic trapped system. For this reason a good picture should be explored to ground any further work. In this section atom light interactions are reviewed and a more thorough work through of laser cooling is shown.

2.2.1 Classical field interaction with a bound two level system

This approach describes a quantised atomic state interacting with a classical field and is referred to as the semi-classical model. An atoms electronic state can be excited to higher allowed states by resonant excitation. Considering two arbitrary electronic states; a ground state $|g\rangle$ and an excited state $|e\rangle$ where they are both eigenstates of the Hamiltonian $\hat{H}_{atom}$.

$$\hat{H}_{atom}|g\rangle = E_g|g\rangle \qquad \hat{H}_{atom}|e\rangle = E_e|e\rangle \tag{2.12}$$

E_g/E_e are both eigenenergys of the respective states. The transition frequency is the difference between the two states and can be expressed as

$$\omega_{eg} = \frac{1}{\hbar}(E_e - E_g) \tag{2.13}$$

With the atomic wavefunction being formed as a superposition of the states

$$\boldsymbol{\psi}(\boldsymbol{r}, t) = c_g|g\rangle + c_e|e\rangle \tag{2.14}$$

where c_e and c_g are complex coefficients. Taking this atom and interacting it with an electromagnetic field. The Hamiltonian describing the atom and the interaction is formed of two terms

$$\hat{H} = \hat{H}_{atom} + \hat{H}_{in} \tag{2.15}$$

Where $\hat{H}_{atom}$ is the unperturbed atom and H_{in} describes the atoms interaction with the field. The interaction Hamiltonian can be expressed as

$$\hat{H}_{in} = \hat{\mu} \cdot \boldsymbol{E}(\boldsymbol{r}, t) \tag{2.16}$$

Where $\hat{\mu}$ is the electromagnetic transition dipole moment operator for a two level system

$$\hat{\mu} = \langle \psi(\boldsymbol{r}, t) |\, e \cdot \vec{r} \,| \psi^*(\boldsymbol{r}, t) \rangle = e \int \psi^*(\boldsymbol{r}, t) \vec{r} \psi(\boldsymbol{r}, t) d\boldsymbol{r} \tag{2.17}$$

Now taking the interacting field to be a monochromatic travelling wave of the standard form

$$\boldsymbol{E}(\boldsymbol{r}, t) = E_0 \hat{\boldsymbol{\epsilon}} cos(\boldsymbol{k} \cdot \boldsymbol{r} - \omega_f t + \phi) \tag{2.18}$$

Where E_0 is the fields amplitude, $\hat{\boldsymbol{\epsilon}}$ is the unit vector along the polarisation of the field, $\boldsymbol{k}$ is the wave vector, ω_f is the field frequency, and ϕ is a constant phase. The atomic states evolution will be described by the time dependent Schrödinger equation[45]

$$i\hbar\dot{\psi} = (\hat{H}_{atom} + \hat{H}_{in})\psi \tag{2.19}$$

The notation of a dot above a parameter indicates a derivative with respect to time for example $\dot{\psi} = \frac{d\psi}{dt}$. Substituting the waveform from equation 2.14 into the time-dependent Schrödinger equation, simplifying the ground state energy to be $E_g \equiv 0$ along with some rearrangement gives 2 coupled equations

$$i\hbar\dot{c_g} = \mu_{ge} c_e \tag{2.20}$$

$$i\hbar\dot{c_e} = \mu_{eg} c_g + \hbar\omega_{eg} c_e \tag{2.21}$$

Where $\mu_{eg} = \mu^*_{eg}$. This now gives us two equations coupling the coefficients c_e and c_g. To make things easier setting $c'_e \equiv c_e e^{i\omega_{eg}t}$ and $c'_g \equiv c_g$ compresses the previous equations into a more manageable format.

$$i\hbar\dot{c'_g} = \mu_{ge} c'_e e^{-i\omega_{eg}t} \tag{2.22}$$

$$i\hbar\dot{c'_e} = \mu_{eg} c'_g e^{i\omega_{eg}t} \tag{2.23}$$

Using the dipole approximation (neglecting the spatial variation of the light due to it being much larger than the atom) allows the interaction operator to be simplified

$$\mu_{eg} = -eE_0 \langle e |\, r \,| g \rangle \, cos(\boldsymbol{k} \cdot \boldsymbol{r} - \omega_L t + \phi) \tag{2.24}$$

$$= -\hbar\Omega_0 cos(\boldsymbol{k} \cdot \boldsymbol{r} - \omega_L t + \phi) \tag{2.25}$$

Where ω_L is the interacting fields frequency, it is a good point to separate this from the on resonant transition frequency ω_{ge} as the difference of these fields plays a roll. Ω_0 is called the on resonant Rabi frequency ($\omega_L = \omega_{ge}$) of the form

$$\Omega_0 = \frac{eE_0 \langle e| r |g\rangle}{\hbar} = \frac{E_0 \cdot \boldsymbol{\mu}_{ge}}{\hbar} \tag{2.26}$$

The Rabi frequency describes the strength of coupling between the atomic dipole and the electric field of the light wave. Taking equations 2.20, 2.21 and inserting them into equations 2.24, 2.25

$$i\dot{c_g'} = \frac{\Omega_0^*}{2} c_e' \left(e^{i(\boldsymbol{k}\cdot\boldsymbol{r} - [\omega_{eg}+\omega_L]t+\phi)} + e^{-i(\boldsymbol{k}\cdot\boldsymbol{r} + [\omega_{eg}-\omega_L]t+\phi)} \right) \approx \frac{\Omega^*}{2} c_e' e^{-i(\boldsymbol{k}\cdot\boldsymbol{r} - \Delta\omega t+\phi)} \tag{2.27}$$

$$i\dot{c_e'} = \frac{\Omega_0}{2} c_g' \left(e^{i(\boldsymbol{k}\cdot\boldsymbol{r} + [\omega_{eg}-\omega_L]t+\phi)} + e^{-i(\boldsymbol{k}\cdot\boldsymbol{r} - [\omega_{eg}+\omega_L]t+\phi)} \right) \approx \frac{\Omega}{2} c_g' e^{i(\boldsymbol{k}\cdot\boldsymbol{r} - \Delta\omega t+\phi)} \tag{2.28}$$

Where $\Omega = \sqrt{(\Delta\omega)^2 + \Omega_0^2}$ is the general Rabi frequency where the laser has a small detuning. $\Delta\omega = \omega_{eg} - \omega_L$ is the detuning between these frequency's. Using the rotating wave approximation allows us to discard the fast oscillating terms ($\omega_{eg} + \omega_L$). This approximation is valid when the light is close to resonance and the powers are considered to be small. Giving the initial condition that at $t = 0$ the state is in the ground state ($c_g' = 1$ and $c_e' = 0$) the time dependence for the excited state can be shown as

$$|c_e'|^2 = \frac{|\Omega_0|^2}{\Omega^2} sin^2\left(\frac{\Omega}{2}t\right) \tag{2.29}$$

The ground state oscillates at the same frequency but π out of phase $|c_g'|^2 = 1 - |c_e'|^2$. This flip-flopping of states is called Rabi oscillations or Rabi flops. When the laser is brought to resonance ($\Delta\omega = 0$) it can be seen that if that interacting field is stopped after a half period of the Rabi frequency the states can be unitarily swapped. This type of pulse is called a π pulse and is a common way of shelving the electronic state. Another interesting manipulation of the state is using a pulse equal to that of $\frac{\pi}{2}$ this generates the state $\frac{1}{\sqrt{2}}(|g\rangle + i\,|e\rangle)$ a superposition state which is a key building block in quantum computing[53].

The description as far has shown what the state will do when interacting with an electric field whereby a state can be stimulated into an excited state and also stimulated to emit. But this lacks the complete picture as based on this alone an atom could be placed in an excited state until stimulated to decay this does not happen in nature as an excited state will spontaneously decay after some time.

2.2.2 Spontaneous emission

The atoms inability to shelve an electron indefinitely is characterised by a spontaneous decay also called spontaneous emission. Spontaneous emission emits in a random direc-

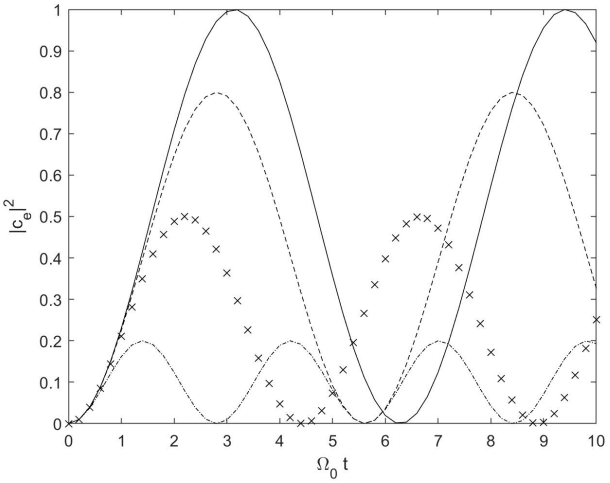

Figure 2.4: Rabi oscillations. The population of a the excited state $|c'_e|^2$ of a 2 level system as a function time when interacting with a electric field. Each plot showing a different detuning. solid line $\Delta\omega = 0$, dashed $\Delta\omega = 0.5\Omega_0$, crosses $\Delta\omega = \Omega_0$, dot dash $\Delta\omega = 2\Omega_0$.

tion and cannot be understood with classical physics, requiring a quantum mechanical approach. Spontaneous emission needs to be introduced into our picture of the 2 level atom and to do this the density matrix $\hat{\rho}$ is introduced.

$$\hat{\rho} = \begin{pmatrix} \rho_{gg} & \rho_{ge} \\ \rho_{eg} & \rho ee \end{pmatrix} = \begin{pmatrix} |c'_g|^2 & c'_g c'^*_e \\ c'_e c'^*_g & |c'_e|^2 \end{pmatrix} \tag{2.30}$$

Where ρ_{gg}, ρ_{ee} are the populations in $|g\rangle$and $|e\rangle$ respectively and ρ_{eg}, ρ_{ge} are the coherence terms between the states. The time evolution $\frac{d\hat{\rho}}{dt}$ of the density operator is defined by the Optical Bloch Equations (OBE). To introduce spontaneous emission to the system equation 2.29 is modified to include a decay term Γ the resulting OBE are shown

$$\frac{d\rho_{gg}}{dt} = \Gamma\rho_{ee} + \frac{i}{2}(\Omega^* e^{-i\Delta t}\rho_{eg} - \Omega e^{i\delta t}\rho_{ge}) \tag{2.31}$$

$$\frac{d\rho_{ee}}{dt} = -\Gamma\rho_{ee} - \frac{i}{2}(\Omega^* e^{-i\Delta t}\rho_{eg} - \Omega e^{i\delta t}\rho_{ge}) \tag{2.32}$$

$$\frac{d\rho_{ge}}{dt} = -\left(\frac{\Gamma}{2} + i\Delta\right)\rho_{ge} + \frac{i}{2}\Omega^* e^{-i\delta t}(\rho_{ee} - \rho_{gg}) \tag{2.33}$$

$$\frac{d\rho_{eg}}{dt} = -\left(\frac{\Gamma}{2} - i\Delta\right)\rho_{eg} - \frac{i}{2}\Omega e^{i\delta t}(\rho_{ee} - \rho_{gg}) \tag{2.34}$$

The OBE can be solved. For steady states $\frac{d\rho}{dt} = 0$ taking $\rho_{gg} + \rho_{ee} = 1$ and that $\rho_{eg} = \rho^*_{ge}$. The steady-state population of the excited state ρ_{ee} and the coupling term ρ_{eg}

$$\rho_{ee} = \frac{\Omega^2}{4\Delta\omega^2 + 2\Omega^2 + \Gamma^2} = \frac{1}{2}\frac{s_0}{1 + s_0 + 4\frac{\Delta\omega^2}{\Gamma^2}} \tag{2.35}$$

$$\rho_{eg} = \frac{i\Omega}{2(\Gamma/2 - i\Delta\omega)(1 + s)} \tag{2.36}$$

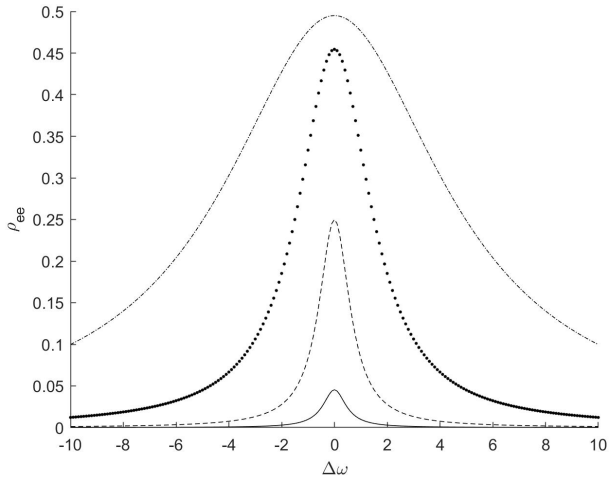

Figure 2.5: Population of the excited state ρ_{ee} as a function of detuning $\Delta\omega$. The different traces indicate different values of the saturation parameter s_0. $s_0 = 100$ indicated by dot dashed line, $s_0 = 10$ indicated by dotted line, $s_0 = 1$ indicated by dashed line, $s_0 = 0.1$ indicated by solid line.

Where

$$s = \frac{\Omega^2}{2\Delta\omega^2 + \frac{1}{2}\Gamma^2} \tag{2.37}$$

s is called the saturation parameter. The on resonance characteristics are also useful to define starting with the saturation parameter s_0

$$s_0 = 2\frac{\Omega^2}{\Gamma^2} = \frac{I}{I_{sat}} \tag{2.38}$$

Where the on resonance saturation intensity is

$$I_{sat} = \frac{\hbar\Gamma\omega_{eg}^3}{12\pi c^2} \qquad\qquad I = \frac{\epsilon_0 E_0^2}{2} \tag{2.39}$$

The excited state population can be seen in figure 2.5 against the detuning with different values of s_0 the shape of which is Lorentzian. Increasing the power the maximum state achieved is saturated at $\rho_{ee_{max}} = 0.5$ where $s \gg 1$. At high saturation parameters the Lorentzian broadens this is called power broadening and can be expressed as an increase in the natural linewidth by

$$\Gamma_{broad} = \Gamma\sqrt{1 + s_0} \tag{2.40}$$

Now the different channels for which the atom can interact with the field and decay have been described, the force and the momentum must be considered.

2.2.3 Radiation pressure and the dipole force

So far the 2 level atoms interaction with an electronic field has been described by its electronic state evolution, the force and momentum transferred haven't been considered. To do this the momentum operator $\hat{p}$ is introduced. Using Ehrenfest theorem [45] the force can be shown to be

$$\boldsymbol{F} = \frac{d\langle\hat{p}\rangle}{dt} = \frac{i}{\hbar}\langle[\hat{H},\hat{p}]\rangle + \left\langle\frac{\partial\hat{p}}{\partial t}\right\rangle \tag{2.41}$$

Ehrenfest's theorem bridges the quantum mechanical analogue of the classical expression stating that the field is the negative gradient of the potential. Using the previous equation. The rate of change of the momentum operator is considered to be time independent $\left\langle\frac{\partial\hat{p}}{\partial t}\right\rangle = 0$ simplifying the expression. The commutation between the system Hamiltonian and the momentum operator is given by $[\hat{H},\hat{p}] = i\hbar\frac{\partial\hat{H}}{\partial x}$. The force can be simplified to

$$F_x = -\left\langle\frac{\partial\hat{H}}{\partial x}\right\rangle \tag{2.42}$$

Considering the force just from the field interaction of the main Hamiltonian $\hat{H} \to \hat{H}_{field}$ using equation 2.16 and making the electric field 2.18 the force along x can be written as

$$F_x = -\frac{\mu_{ge}}{2}\left(\frac{\partial E_0}{\partial x}(\rho_{ge}+\rho_{eg}) + E_0 ki(\rho_{ge}-\rho_{eg})\right) \tag{2.43}$$

This has been arranged in a way highlighting the force consists of both a real and imaginary component. If we now use the steady state solution for ρ_{eg} found in equation 2.36 and the saturation parameter the force can be expressed in its final form

$$F_x = \frac{s_0\mu_{ge}/\Omega_0}{1+s_0+4\frac{\Delta\omega^2}{\Gamma^2}}\left(-\Delta\omega\frac{\partial E_0}{\partial x} + \frac{\Gamma}{2}E_0 k\right) \tag{2.44}$$

The force consists of 2 distinct parts. The first part is proportional to the gradient of the electric field and the fields detuning (field dependent). The second term is proportional to the spontaneous emission rate Γ (atom dependent). It is worth exploring each part in detail starting with the first term.

The dipole force

The first term due to being proportional to its detuning implies that when the field is on resonant $\Delta\omega = 0$ this force goes to 0. When the field is off resonant a force is felt that pushes the atom towards the fields maximum intensity. This is called the dipole force and has the form

$$F_{dipole} = -\frac{\hbar\Delta\omega}{\Omega_0}\left(\frac{s_0}{1+s_0+4\frac{\Delta\omega^2}{\Gamma^2}}\right)\frac{\partial\Omega_0}{\partial x} \tag{2.45}$$

Another interesting case is when the the interacting field is heavily detuned $\Delta\omega \gg \Gamma$ this simplifies the dipole force to

$$F_{dipole} = -\nabla\left(\frac{\hbar\Omega^2}{4\Delta\omega}\right) \tag{2.46}$$

Where $\frac{\hbar\Omega^2}{4\Delta\omega}$ is the magnitude of the AC stark shift. This is a shift of the coupled transitions energy levels due to off resonant coupling. The spatial gradient of the AC stark shift is equal to that of the dipole force. A more useful notation conveys the dipole force with respect to intensity

$$F_{dipole} = -\frac{\mu_{ge}^2 \nabla I}{\hbar c \epsilon_0 \Delta\omega} \tag{2.47}$$

$$I = \frac{1}{2} c \epsilon_0 E_0^2 \tag{2.48}$$

$$\tag{2.49}$$

The AC stark shift plays a roll in clock operation systematic shifts.

Radiation pressure

The second term in the atom light force equation is proportional to the decay rate of the coupled transitions.

$$F_{rp} = \frac{1}{2}\left(\frac{s_0}{1 + s_0 + 4\frac{\Delta\omega^2}{\Gamma}^2}\right)\frac{\mu_{ge}\Gamma E_0 k}{\Omega_0} \tag{2.50}$$

This can be simplified noticing that the steady state solution to the excited state shown in equation 2.35 and can be introduced making the equation

$$F_{rp} = \rho_{ee}\Gamma\hbar k \tag{2.51}$$

This simple equation brings out some interesting points. The force is due to the absorption of the photons momentum $p_{photon} = \hbar k$ as this becomes maximised when the population is in the excited state $\rho_{ee} = 1$. The force saturates to an upper limit dictated by the decay rate of the chosen state. This means there is a force in imparted by the field in the direction of the field, this force is called radiation pressure.

Radiation pressure can be understood by considering a blow by blow account of what is happening. An atom in the ground state absorbs a photon of momentum $p_{photon} = \hbar k$. The atom receives a momentum kick and the electron is prompted into its excited state. From this position the atom can evolve in two ways. Another incoming photon can stimulate the emission leading to a net zero force as the recoil is in the opposite direction as the absorbed kick. Or it can spontaneously emit. As previously stated spontaneous emission emits in a random direction meaning over a large enough repetition rate the net force is

zero, but the initial recoil remains meaning there is a force due to the absorbed photon. Radiation pressure is the exploited effect that underpins Doppler laser cooling.

2.2.4 Doppler cooling

Laser cooling or Doppler cooling is a technique used to cool an atomic or ionic sample to sub mili Kelvin temperatures. It uses a laser or lasers, detuned from atomic resonance by which it exploits the Doppler effect in drawing the frequency along the atoms motional component, bringing the field back into resonance, exploiting spontaneous emissions random emission direction and the resulting imbalance in momentum to reduce the a ions motion. The technique of Doppler cooling a trapped ion can be considered to be the same as a free atom, as long as the trap drive frequency is much smaller than that of the decay rate of the transition meaning the ion.

Previously the fields interaction with a stationary atom and the resulting internal dynamics and reactive forces have been shown. However, for Doppler cooling the atom is not in a stationary state. When the atom has a component of motion in the same direction as the interacting field, the atom observes a shift in the fields frequency due to the Doppler effect. In the atoms frame of reference $\Delta\omega \rightarrow \Delta\omega + \delta$ where $\delta = \nu_k k$. δ is the induced Doppler shift. ν_k is the velocity of the atom in the direction of the field. The radiation pressure can be rewritten as

$$F_{rp} = \frac{1}{2}\left(\frac{s_0}{1 + s_0 + 4\frac{(\Delta\omega+\nu_k k)^2}{\Gamma}^2}\right)\frac{\mu_{ge}\Gamma E_0 k}{\Omega_0} \tag{2.52}$$

The force can be Taylor expanded about $\nu_k = 0$ to separate the unshifted force from the Doppler component. The first two terms of the expansion are

$$F_{rp} \approx F_0 + F_{Doppler} \tag{2.53}$$

Where by F_0 is equal to that of the radiation pressure represented in equation 2.50. The second term in the expansion representing the Doppler force and is commonly expressed as a coefficient β multiplied by the atoms velocity

$$F_{Doppler} = \beta\nu_k \tag{2.54}$$

$$\beta = -\frac{4\hbar k^2 \Delta\omega\nu_k}{\Gamma}\left(\frac{s_0}{1 + s_0 + 4\frac{\Delta\omega^2}{\Gamma}^2}\right)^2 \tag{2.55}$$

The key point being that this force acts against that of the atoms motion when the detuning is negative $\Delta\omega < 0$ (red-detuned) or with it when its positive $\Delta\omega > 0$ (blue-detuned). Meaning this force can be used to both increase the atoms motion when blue-detuning heating the atom or reduce its motion by red-detuning cooling the atom. β

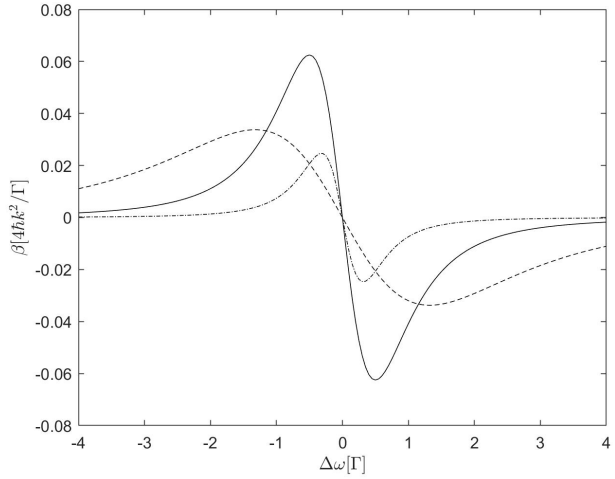

Figure 2.6: The graph shows the magnitude of the Doppler cooling coefficient β against the interacting fields detuning $\Delta\omega$. Different saturation parameters are shown: $-$ line $s_0 = 0.2$, solid line $s_0 = 2$, $--$ line $s_0 = 20$.

can be maximised with respect to $\Delta\omega$ by setting the detuning to half the width of the transition $\Delta\omega = \Gamma/2$. The saturation parameter can also be maximised setting $s_0 = 2$. This maximised force is shown in figure 2.6. The graph shape shows the heating and cooling abilities which can be exploited by selectively detuning the interacting field.

Focusing on the ability to cool $\Delta\omega < 0$. The damping force can reduce the kinetic energy of the atom at the rate

$$\dot{E}_{cooling} = \nu_k F_{doppler} = -\beta\nu_k^2 \tag{2.56}$$

But there is a underlying heating rate. The recoil from spontaneous emission averaged over time goes to zero, but each emission viewed as individual event does have a net momentum. The atom's momentum does a random walk about zero, this gives rise to a heating effect defined by the spontaneous emission rate of the atom. This heating rate can be characterised by considering the kinetic energy from the recoil and is of the form

$$\dot{E}_{heating} = \frac{(\hbar k)^2 \Gamma \rho_{ee}}{m} \tag{2.57}$$

Where m is the mass of the atom. The detuning is set to maximise the cooling force $\Delta\omega = -\Gamma/2$. By balancing the rate of cooling and the heating in a state of equilibrium and taking $m\nu_k^2/2 = k_B T/2$. The Doppler cooling limit can be extracted to be

$$T_{limit} = \frac{\hbar\Gamma}{2k_B} \tag{2.58}$$

The Doppler cooling limit using the cooling transition of $^{40}Ca^{+}$ is 0.5 mK.

Laser cooling a free atom would require the use of three pairs of counter propagating beams, each pair allowing slowing along that axis regardless of atoms trajectory with each pair coupled to a principle axis. For an Ion trap this can be reduced due to the trap acting to oppose the ions motion. Laser cooling of trapped Ions can be achieved with just one beam that has a component in each principle axis. The trap setup in this thesis uses 2 due to geometric considerations this is discussed further in Chapter 4.

2.3 The $^{40}Ca^{+}$ ion

Calcium ion has an alkali like electronic structure similar to that of potassium. The electronic structure means only one electron is outside the closed shell making it a Hydrogen-like atom. The lowest lying electronic states are shown **??** with all relevant transitions and decay channels indicated. Laser cooling (discussed in 2.2.4) can be efficiently achieved using either the $4^2S_{1/2} - 4^2P_{1/2}$ or the $4^2S_{1/2} - 4^2P_{3/2}$[1] both paths require repump beams due to their decay channels being significant but using the lower $4^2P_{1/2}$ state requires one less beam allowing for simpler operation. This is used in this system. The $4^2S_{1/2}$ – $3^2D_{5/2}$ transition is dipole forbidden and is used as the reference transition due to its narrow linewidth. Due to the closed lambda system created by ($4^2S_{1/2}$, $4^2P_{1/2}$, $3^2D_{3/2}$) this gives a simple method for state detection and laser cooling. For the rest of this text its common usage to refer to $4^2S_{1/2}$ – $4^2P_{1/2}$ as the cooling transition $3^2D_{3/2}$ – $4^2P_{1/2}$ as the repumper transition, $4^2S_{1/2}$ – $3^2D_{5/2}$ as the clock transition and the $3^2D_{5/2}$ – $4^2S_{3/2}$ as the quench transition.

A key benefit for using ionic calcium is the wavelengths required to perform laser cooling, state preparation and read out are all addressable with commercially available diode laser technologies.

2.3.1 Systematic shifts

A single trapped ions behaves as an extremely well understood physical system, but the environment that it is surrounded by tends to not be harder to predict. With optical clocks achieving such high fractional stability small environmental effects can have a large interaction with the ion shifting the clock transition. These shifts are predominately

[1] The $4^2S_{1/2}$ – $3^2D_{5/2}$ can also be used to Doppler cool the ion but it is more difficult to implement due to its narrow linewidth

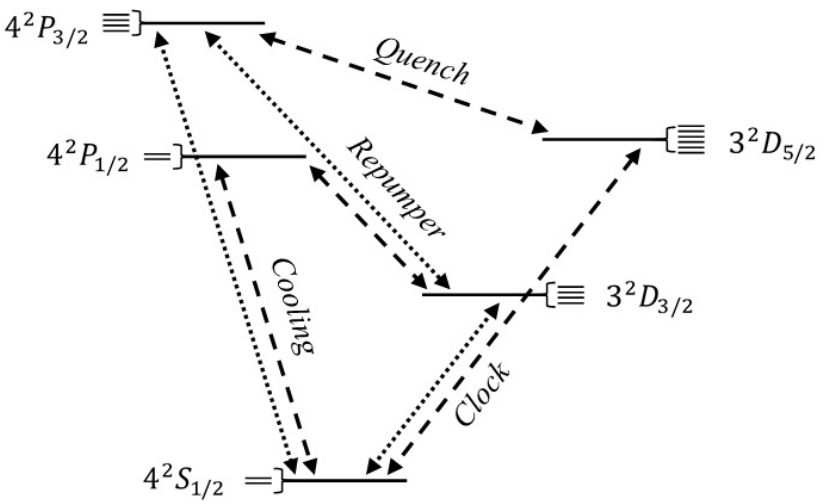

Transitions name	Coupled levels	Wavelength (air) [nm]	Decay rate $/2\pi$ [Mhz]
Cooling	$S_{1/2} \rightarrow P_{1/2}$	396.847	20.67
Repumper	$D_{3/2} \rightarrow P_{1/2}$	866.214	1.69
Clock	$S_{1/2} \rightarrow D_{5/2}$	729.147	$15.23 \cdot 10^{-8}$
Quench	$D_{5/2} \rightarrow P_{3/2}$	854.209	1.58
-	$S_{1/2} \rightarrow P_{3/2}$	393.366	21.51
-	$D_{3/2} \rightarrow P_{3/2}$	849.802	0.18
-	$S_{1/2} \rightarrow D_{3/2}$	732.289	$14.74 \cdot 10^{-8}$

Figure 2.7: The lowest lying energy levels of $^{40}Ca^{+}$ ion. In the figure dashed lines indicate transitions that are used in this experiment the dotted ones for reference. Wavelengths and decay rates are shown.

Zeeman shifts, the electric quadrupole shift, second-order Doppler shifts and Stark shifts. The cause and mitigation techniques are highlighted below.

Zeeman shifts

Uncompensated magnetic fields couple to the magnetic moment of the ion resulting in a shift in the clock transition. The first order Zeeman shift can be compensated by inducing a bias magnetic field and sequentially sampling two of the components which are symmetric about the unshifted line center[54]. The second order Zeeman shift although much smaller than the first order can be significant depending on the accuracy of the clock. A three Gauss magnetic field corresponds to an ≈10 MHz first order Zeeman shift, and a 1.3 Hz second order Zeeman shift[55]. When designing a trap magnetic shielding reducing the influence of external fields and compensation coils to introduce a bias magnetic field for Zeeman compensation are required. The stability of these coils around a few hundred micro Gauss is enough[55].

Electronic quadrupole shift

Electric field gradients, due to stray patch potentials and uncompensated micromotion, couple to the electric quadrupole moments of the ion shifting the clock transition. The quadrupole moment for $^{40}Ca^{+}$ is $1.83(1)ea^2$, this corresponds to a shift sensitivity of 2.975(2) Hz mm^2V^{-1}[56]. To compensate for this an measurements of several Zeeman levels can be taken and each averaged[57]. Patch potentials most commonly form during ion loading. As neutral atoms are ionised in the trap environment to form the wanted ion, the stripped electrons and untapped ions can be deposited onto ungrounded or dialectic surfaces in the trap environment. This results in unwanted build up of stay electric fields. To reduce build up of these patch potentials, careful planning of the trap environment is needed and the ability to load using low flux atomic beams with higher ionisation beam powers can be used.

Second-order Doppler shifts

Uncompensated ion motion due to the thermal motion and micro-motion causes a second order Doppler shift. The second-order Doppler shift ($\Delta\nu_{2nd}$) can be written as[58].

$$\frac{\Delta\nu_{2nd}}{\nu} = -\frac{3k_BT}{2mc^2} \tag{2.59}$$

Where ν is the transition frequency. Taking the temperature as that of the Doppler cooling limit as seen in equation 2.58, it can be seen that with $^{40}Ca^{+}$ a second-order Doppler shift

of $-1.9 \cdot 10^{-18}$ can be calculated. This could be further reduces using a method that cools past the Doppler limit such as resolved side-band cooling[59].

Mirco-motional second-order Doppler shift is heavily coupled to the quality of the micro-motion compensation. There are two commonly practised methods for gauging the shift depending on the which is bigger, the trap drive frequency (Ω) or the linewidth of the transition (Γ)[58].

For $\Omega \gg \Gamma$ this allows a comparison of the scatter rate generated when the laser is tuned to resonance ($\omega_{laser} - \omega_{ion} \approx 0$) R_0 compared with tuned to the first side band ($\omega_{laser} - \omega_{ion} = \pm\Omega$).

$$\frac{\Delta\nu_{2nd}}{\nu} \approx -\left(\frac{\Omega}{ckcos(\theta)}\right)^2 \frac{R_1}{R_0} \tag{2.60}$$

Where $kcos(\theta)$ is the angle between the laser propagation axis and the micromotion axis. This is typically used when using the clock laser to measure the shift.

For $\Omega \ll \Gamma$ this uses the cross correlation technique. This monitors the scatter rate from the cooling transition and correlates the modulation due to the first order Doppler shift.

$$\frac{\Delta\nu_{2nd}}{\nu} \approx \frac{1}{4}\left(\frac{\Gamma}{ckcos(\theta)}\frac{\Delta R_d}{R_{max}}\right)^2 \tag{2.61}$$

Where ΔR_d is the scatter rate correlated to the trap drive frequency and R_{max} is the scatter rate when the laser is tuned to resonance. This allows the use of other transitions to gauge the shift.

It can be seen, if not compensated properly the second-order Doppler shift can be a significant.

Stark shifts

Electric field couplings to the ion can occur through several channels, all of which result in a Stark shift of the clock transition. Micromotion and thermal ion motion can induce a Stark shift. As well as the surround environments black body radiation shifts the clock transition. The lasers used to probe the clock transition, laser cool the ion and used for state readout, all can induce an AC Stark shift. These all interact with varying degrees and can be suppressed or compensated if certain actions are taken.

The micro-motion induced Stark shift can be calculated as with second-order Doppler shift based on which is larger the trap drive frequency or the linewidth of the transition. Taking $\Omega \gg \Gamma$ the motional induced stark shift can be written as[58]

$$\Delta\nu_s \approx 2\sigma_s\left(\frac{m\Omega}{Qk \cdot cos(\theta)}\right)^2 \frac{R_1}{R_0} \tag{2.62}$$

Where σ_s is the Stark shift coefficient of the transition. In the case when $\Omega \ll \Gamma$ The Stark shift becomes.

$$\Delta\nu_s \approx \sigma_s \frac{1}{2} \left(\frac{m\Gamma\Omega}{Qk \cdot cos(\theta)} \frac{\Delta R_d}{R_{max}} \right)^2 \tag{2.63}$$

Where Q is the charge of the ion. This trap induced stark shift can be suppressed by driving the trap at a frequency where by the RF-induced stark shift and the second-order Doppler shift cancel each other out[60]. For this reason our trap will be driven at 24.7MHz.

The trap environment emits a Planck blackbody radiation spectrum on the ion inducing a Stark shift. To understand the effect the thermal profile of the surrounding structure of the ion must be understood. The trap electrodes due to their design can become very hot when driven and these also tend to be the surfaces closest to the ion. A combination of rf theoretical modelling and real world temperature measurements with in vacuum sensors are required to predict this shift. The black body radiation shift accounts for most uncertainty budgets of trapped ion clocks[60] due to its hard to measure nature, but with proper modelling and some measurement $^{40}Ca^{+}$ at ≈300K can be reduced to a few parts in 10^{18}[61]. For this reason our system will contain in vacuum temperature sensors, allowing an accurate model of the thermal profile of the ion to be calculated.

Laser interaction with the electric dipole moment of the ion can induce an AC Stark shift. This occurs primarily with off-resonant transitions coupling to the probing laser field. Due to this, the intensity of the field is the main contributor. This means with better stability in the clock laser, the needed power to drive the clock transition reduces and thus the AC stark shift also reduces. This is also true not just for the clock laser but also for the other laser needed for cooling and state detection. The best way to mitigate these shifts is to turn off the lasers when the probe laser is cycling. However real world shutters have a finite extinction ratio. For practical laser intensities used in $^{40}Ca^{+}$ ion trapping experiments an extinction of 70 dB caused AC stark shifts below mHz for each laser[60].

Chapter 3

Laser design and assembly

This chapter discusses the fiber integrated laser system's design and characterisation. It is broken down in to three sections: The first section gives an overview of the current laboratory laser system and its limitations, how fiber optics can be used to reduced size weight and power (SWaP), and what specifications are required for a $^{40}Ca^{+}$ reference laser system. The second section describes the design, gives details on each of the laser system components, the chosen technologies used and the layout of each laser. The third section is on the assembly and characterisation of the laser system, giving details on how each laser was assembled and characterised, as well as the long-term stability of the system. The laser system in this thesis does not include the clock laser. The clock laser diode selection is only referenced in the design section as to indicate the direction that is ongoing.

3.1 Overview

The laser system is used to manipulate, control and exploit the trapped ion's desirable characteristics. The laser system is required to be.

1. Frequency tuneable, allowing to easily adjust the desired wavelengths when needed.
2. Lasers maintain stability over long periods of time (months).
3. Controllable, allowing each laser to be pulsed on and off.

Also required are optical power and polarisation control for efficient coupling of each desired transition.

Laboratory based laser systems achieve this by having several subsystems coupled to each laser. These subsystems modify the laser beams properties to the desired specification. A series of mirrors and beam splitters allow the laser beams path to be redirected and steered to the desired subsystem. Free space beam propagation allows high adaptability.

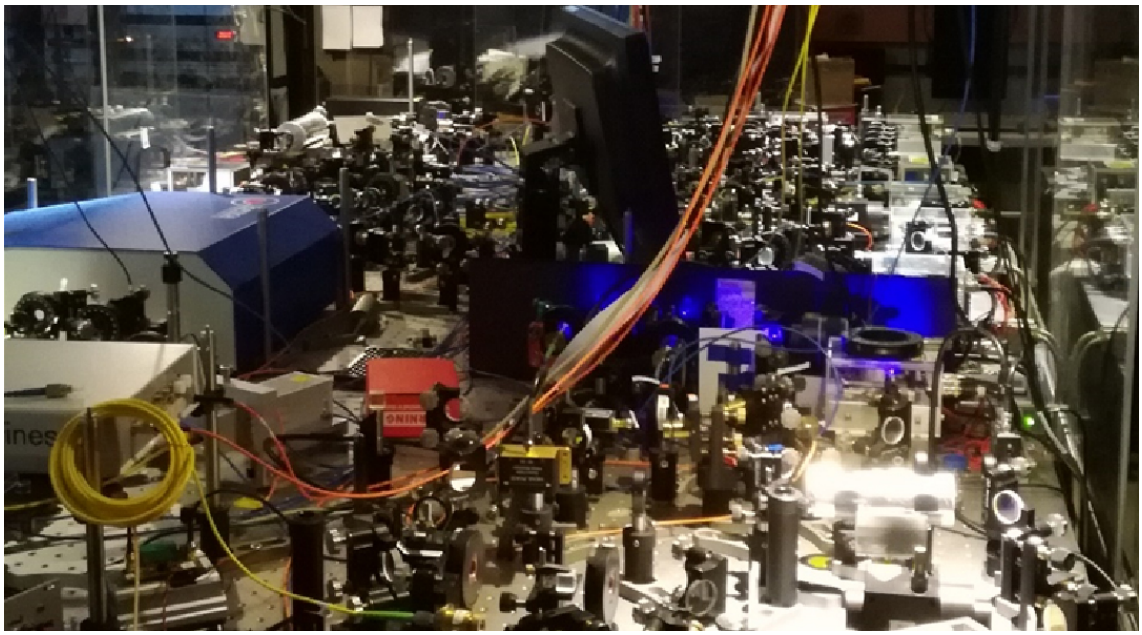

Figure 3.1: The ITCM free space laser bench used to drive two experiments covering a full 1.5 m x 3.0 m optical breadboard.

Therefore, components can be put in, taken out and upgraded with just the use of a few mounts and clamps. An example of how this is achieved is based on ITCM's laboratory based $^{40}Ca^{+}$ laser system (see figure 3.1). This laser system is made up of: An optical table (1.5 m x 3.0 m) supported by four active vibration isolation supports, these reduces path length differences and the long-term misalignment caused by vibrations. The entire laser system is mounted on this table.$^{40}Ca^{+}$'s transitions are all addressable using diode lasers. In the laboratory these are commonly extended cavity diode lasers (ECDL) based on a variety of configurations, these benefit from wide tunable wavelength ranges ($\approx$ 40 nm), whilst still being very short-term stable ($\approx$ 1 MHz) and have adequate powers ($\approx$ 50 mW). Optical isolators decouple the laser from any back reflections caused at the optics interfaces, which would destabilise the lasers. Optical mirrors, polarisation beam cubes and wave plate retarders are used to steer the lasers beams, allowing adjustment of powers and polarisations to each coupled system. Acousto-optical modulators act as fast shutters and allow for fine tuning of the beam frequency. Mechanical shutters are used for further isolation of the beams when needed. A calibrated wavemeter is used as a reference system to steer all the lasers to specific frequencies. For the highest stability needed for the clock laser, a high precision optical cavity acts as a short-term stabilisation system reducing the reference lasers linewidth down to (<Hz). On top of this, electronic control for each system is required. The combination of all these components makes common laboratory

based laser systems large (>1000 l), heavy (>1000 kg), high power (>1000 W) and high maintenance.

Commercial systems are on the market in 19" full rack configuration. They are smaller than laboratory based laser systems ($> 100l$), but still based on small optical breadboards utilising free space beams coupled to free space subsystems, making them susceptible to vibrations and are not maintenance free.

The key technology to make the laser system portable and maintenance free are integrated fiber optics. Coupling each system using single mode (SM) polarisation maintaining (PM) fibers reduces vibration sensitivity, as well as maintaining polarisation stability across the propagation distance. Designs can make efficient use of the available space and therefore reduce in size significantly. All the required components of a standard laser system are available as fiber integrated versions. These components tend to have smaller form factors due to their fiber integration, this tends towards low power control systems that are used to drive each component. Fiber integration is the key technology bringing down the size, weight and power (SWaP) of the laser system.

Laser wavelength [nm]	**Optical power [μW]**	**Stability [MHz]**	**Additional considerations**
397	< 20	< 1	fast tunability, multiple beams, gated
866	< 500	< 10	high extinction ratio, gated
729	$< 10,000$	$< 10^{-6}$	fast tunability, gated
854	< 500	< 10	high extinction ratio, gated
423	< 100	< 20	switched
< 389	< 500	NA	switched

Table 3.1: The required optical parameters needed to by each laser to photo-ionise, Doppler cool and perform the clock operations on $^{40}Ca^{+}$. Additional considerations are highlighted. The 866 and 854 lasers induce a AC stark shift in the clock transition and must be gated using a high extinction ration shutter. The 397, 866, 729, 854 require gating to allow for controlled pulses to be used to perform certain manipulations on the ion. The 397 and 729 require fast tunability of frequency to allow for frequency steering. The lasers at 423 and <389 require switched operation this is distinguished between gated as these lasers switched timings is uncritical.

The laser system requirements for $^{40}Ca^{+}$ are highlighted in table 3.1. The order in which the lasers are needed are photo-ionisation, cooling, clock state probing, state detection and quenching. These processes require lasers to address specific transitions within the ion.

3.2 Design

Each laser in this system needs to be optimised for five characteristics:

1. Form size
2. Optical output power
3. Tuneable range (Mode hop free)
4. Spectral linewidth
5. Robustness

An advantage of $^{40}Ca^{+}$ is that all the required frequencies are addressable with diode lasers. Diode lasers benefit from low SWaP with a range of configurations. These allow for GHz mode-hop free tuneable ranges, narrow linewidths < 100 kHz and high optical powers > 100 mW.

The diode lasers chosen are based on three different configurations: A distributed Bragg reflector laser made by Photodigm, which is housed inside their Mercury package. A monolithic micro ECDL by Sacher Lasertechnik, which is referred to as the Micron laser, and a direct diode laser by Nichia. The use of different lasers and manufacturers allowed testing of which behaved best in a portable system.

Laser diodes are directly available at the needed UV wavelengths but are not as DBR or integrated ECDL lasers. The available laser diodes suffered from short mode hope free tuning ranges and reduced stability. Because of that, the UV transitions 397 nm and 423 nm are accessed using frequency doubling of 794 nm and 845 nm diodes. The 375 nm laser is a non critical laser, this is because the frequency used is above the ionisation threshold and just requires the output power to exceed $100\mu W$ for efficient ionisation. Therefore a simple laser diode by Nichia was chosen. All the lasers and specifications used are shown in table 3.2.

Configuration	**Wavelength [nm]**	**Max optical power [mW]**	**Stability [MHz@1ms]**	**Part No.**
Mercury	795	> 160	< 10	PH795DBR080TS
Micron	866	> 120	< 0.1	S1-0866-100 BFY
Micron	729	> 30	< 0.1	S1-0729-100 BFY
Mercury	854	> 100	< 10	PH852DBR040TS
Micron	845	> 120	< 0.1	S1-0845-100 BFY
Diode	375	30	$--$	NDU4116

Table 3.2: Each lasers specification, indicating the chosen technologies key optical properties. The use of different technologies is to test which performs best in a portable system outside of their characterised environment (vibration isolated optical benches).

3.2.1 Lasers modules

The laser cannot be pigtailed directly due to back reflections destabilising the laser. This makes using a free space optical isolation the only option, after which the beam must be launched into a fiber. This bounds the laser design.

The laser diode package, the electrical D-sub, the optical isolator and a six axis fibre coupler make up the laser (see figure 3.2) for all lasers but the 375 nm which is housed in a commercially available housing (see figure 3.3.

Both laser diodes have different package formats. For ease of fabrication each laser was made to fit the same profile. For the Mercury lasers a conversion block was machined out of brass in order to accommodate the mercury package into the same mount as the Micron laser.

The lasers are mounted on an aluminium frame. The aluminium frame allows for good thermal conduction distributing each lasers generated heat. The frame gives a rigid platform to maintain optical coupling, as well as being light weight, it is also designed to keep the beam path central to the both the optical isolator and the fiber coupler.

Each laser's electrical connections are converted to a D-sub 9 pin variant DE-9. This allows for robust and easy connection between the control board. The laser control electronics are discussed in section 3.2.3.

The optical isolators are free space to block back reflections at the fiber interface. The isolators used (Thorlabs, IO-3D-850-VLP for 845, 854, 866 nm and IO-3D-780-VLP for 795 nm) are mounted just after the diodes and are fixed using compression clamp built

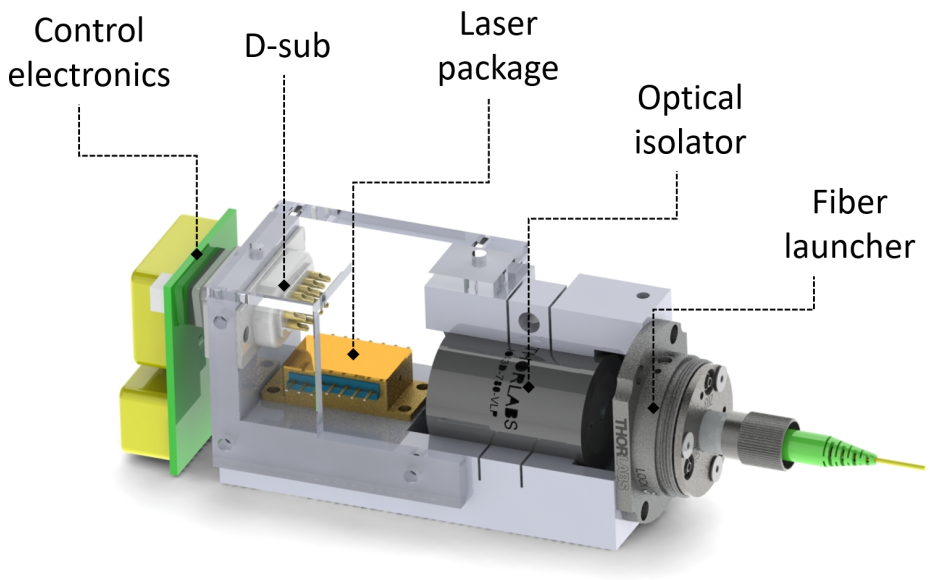

Figure 3.2: This image shows a cut out of the laser module design used for the 866 nm, 854 nm, 845 nm and 794 nm laser packages. The total package dimensions with control board attached are 120 x 36 x 43 mm. Original design created by Professor Keller.

into the frame.

The fiber couplers (Thorlabs, PAF2-5) consist of a small collimation lens and six axis control (x,y,z,tilt,tip and roll) with all, except roll, having fine adjustment. This can be secured using a locking grub screw to maintain alignment. The launchers are mounted at the end of the frame.

Finally, perspex shields are placed around the diode housing, sealing off the assembly. This is to reduce any air currents interfering in the free space environment and to protect from any dust that might settle on the optics.

The 375 nm diode is mounted in a collimation tube (Thorlabs, LTN330-A) which is converted to a 1 inch form factor (Thorlabs, AD11F) connected to a lens tube (Thorlabs, SM1L05) and adapted (THORLABS, CP08FP/M) to a six axis fibre coupler (ThorLabs, PAF2-5A) mounted at the front. The electronic control board is connected via a standard four pin laser diode connector. The different design is due to the laser not requiring temperature stabilisation or frequency tuning.

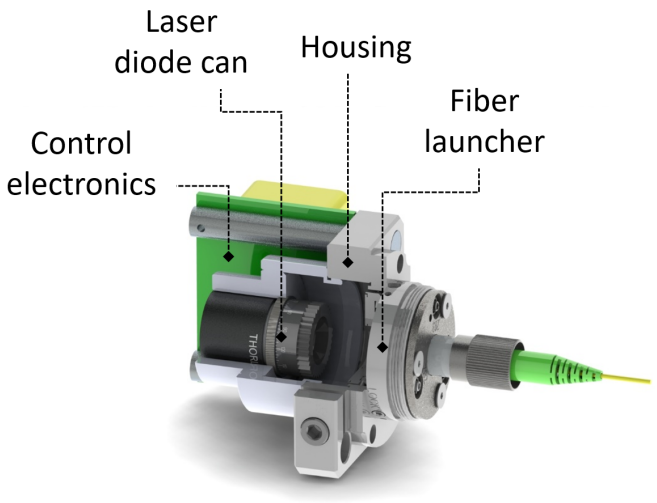

Figure 3.3: This figure shows a cut out of the laser module design used for the 375 nm laser package. The total package dimensions with control board attached are 60 x 41 x 51 mm. Original design created by Dr Gonzalvo.

3.2.2 The laser system

The laser system produces seven outputs, three of them being delivered to the trap and four to a reference wavemeter. There are two independent subsystems (see figure 3.4), the UV lasers consisting of the cooling laser and the photo-ionisation lasers, and the IR lasers made up of the re-pump laser and quench laser. Each fiber integrated component in each assembly is spliced to the next one, creating a continuous fiber network. A description of the splicing method can be found in the section 3.3.4.

3.2.2.1 UV Lasers

Cooling laser [794 nm/397 nm]

The cooling branch starts with the 794 nm laser module. This module is coupled to the connectorised input of the 99/1 fiber beam splitter [Laser components, CP-PS-P-1X2-794-1/99-900-5-1-FA-3X54] utilising PM780-HP fiber throughout. This beam splitter is used to sample off 1% of the lasers power for wavemeter referencing. The 99% output arm is spliced to the input of the fiber coupled acousto-optical modulator (AOM). The AOM [Gooch and Housego, SFO4533-T-M150-0.5C2W-3-F2P-01] allows the frequency of the laser to be finely tuned and rapidly switched. This is controlled by a SMA input requiring a 1 W source at 20 MHz. The output of the AOM is spliced to the frequency doubling

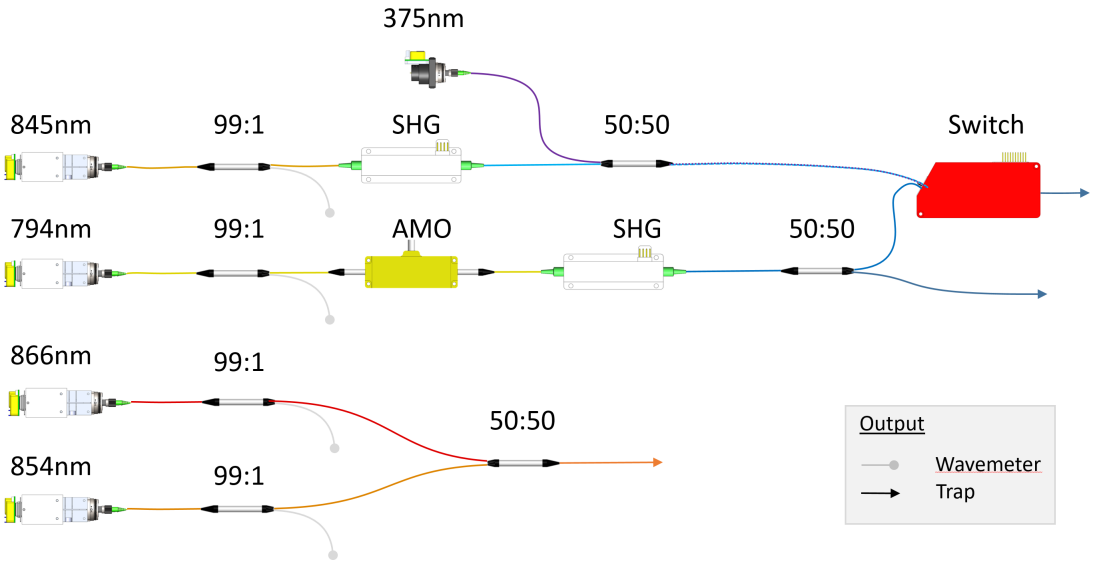

Figure 3.4: Schematic figure of the fiber component layout. SHG stands for Second Harmonic Generation and AOM for Acousto-Optical Modulator.

component. The frequency doubler [HCP Photonics Corp, 1WM079400H111010CP002] is based on second harmonic generation (SHG) using a wave guided Periodically Poled Lithium Niobate crystal (PPLN). The PPLN crystal is mounted on a thermoelectric cooler (TEC) which is controlled by four pin connector allowing the temperature to be tuned for optimum SHG. The input fiber is a PM780-HP with the output fiber a PM-S405-XP. The output of the frequency doubler is spliced to a 50/50 UV fiber beam splitter[1][GOULD Fiber Optics, 52-36740-50-11202] which utilises PM-S405-XP fiber. The 50/50 acts to split the power between the two intended cooling arms of the trap, with one of the arms going directly to the trap and the other continuing to an optical switcher. The switcher (Laser Components, optical switch 1x2) acts to swap between photoionisation and cooling beams. The output of the switcher goes directly to the trap.

Photoionisation lasers [845 nm/423 nm] + [375 nm]

The photoionisation lasers are made up of a laser module at 845 nm and the 375 nm module. The 845 nm laser module is coupled to the connectorised input of the 99/1 fiber beam splitter [Laser components, CP-PS-P-1x2-850-1/99-900-5-1-FA-3X54]. The fiber used in this component is PM780-HP. The 1% branching arm is outputted to a wavemeter, while the 99% arm is spliced to the input of the frequency doubling component. The frequency doubler [HCP Photonics Corp, 1WM084700H111010CP002] works the same as

[1]The high extinction shutters under development will be spliced after the SHG

the other SHG used in the cooling laser. The input fiber of the SHG uses PM780-HP and its output fiber PM-S405-XP. The output of the frequency doubler is spliced to a UV fiber combiner [GOULD Fiber Optics, 52-36740-50-11202], which utilises the PM-S405-XP fiber. The combiner brings the 423 nm and 375 nm lasers into one output. The output of the combiner is spliced to the input of the switcher denoted in the cooling laser.

3.2.2.2 IR Lasers

Re-pump laser [866 nm]

The 866 nm module is coupled to the connectorised input of the 99/1 fiber beam splitter [Laser components, CP-PS-P-1X2-866-1/99-900-5-1-FA-3X54]. This beam splitter uses PM780-HP fiber. The 1% branching arm is outputted to a wavemeter, while the 99% arm is spliced to one of the two inputs of a fiber combiner [Laser components, PBS-1X2-P-866-900-1-1-FA]. This is used to combine both, the quench laser and the re-pump laser. The combiner uses PM780-HP fiber.

Quenching laser [854 nm]

The quench laser starts with the 854 nm laser module. This module is coupled to the connectorised input of the 99/1 fiber beam splitter [Laser components, CP-PS-P-1X2-850-1/99-900-5-1-FA-3X54]. The one % branching arm outputs to the wavemeter. The 99% output is spliced to the other input arm of the switcher denoted in the re-pump laser.

3.2.3 Control electronics

Each one of the lasers as well as the two SHGs require highly stable control electronics. Each laser requires a stable current supply to drive the laser, and both the lasers and the SHGs require temperature stabilisation. Noise on these systems will lead to frequency and power instability.

Commercially available control systems tend to be to bulky and consume high power. These control systems often have additional features that are not needed for a portable system. The priorities of a small, high efficiency and low noise controller, that can be externally managed, was realised by a set of analogue control chips made by Analogue Technologies.

Analogue Technologies inc specialise in controllers that are internally referenced and have inbuilt high bandwidth feedback loops mounted inside a small multi-pin package. Each of these chips are controlled by an external input voltage, which sets the output

point. The internal feedback loop then maintains the output allowing for tuning (Hz) and stable control.

The TEC drivers have stabilities of 0.004°C and the current drivers 100 ppm $°C$. The TEC control circuit is based on their recommended design with selective values for the feedback resistors and capacitors based on the laser packages thermal capabilities. These values have to be configured to ensure the feedback loop behaves optimally. The values are covered in the assembly section 3.3.

The electronic control board (see figure 3.5) outputs to the laser via a D-sub DE-09 male, allowing for a robust connection between the laser and the control board. The board is powered on a separate connector to isolate any cross talk.

The laser control boards for the 794 nm, 866 nm, 854 nm and the 845 nm lasers all share the same design. The 375 nm laser and the two SHGs share similar architecture to the laser control board but require only one of the modules (SHGs require only TEC control and the 375 nm laser only current control). For this reason the designs are shown but not described (see figure 3.5). Each laser requires different set temperatures and lasing currents the used controllers reflected this (see table 3.2.3). The performance of the chips differ, but all except the 375 nm controllers share the same pin configuration and form factor. The 375 nm, due to its larger current drive, requires a larger board.

Wavelength [nm]	**Configuration**	**Current Controller**	**TEC controler**
794[397]	Mercury	ATLS200MA103	TEC5V3V-DAH -5/15/5/10K
866	Mercury	ATLS200MA103	TEC5V5V-D
845[423]	Micron	ATLS200MA103	TEC5V5V-D
854	Micron	ATLS200MA103	TEC5V5V-D
729	Micron	ATLS200MA103	TEC5V5V-D
375	Diode	ATLS500MA212D	–
794[397]	SHG	–	TEC5V6A-D
845[423]	SHG	–	TEC5V6A-D

Table 3.3: This table shows each laser's control electronics part numbers. All components are made by Analogue Technologies

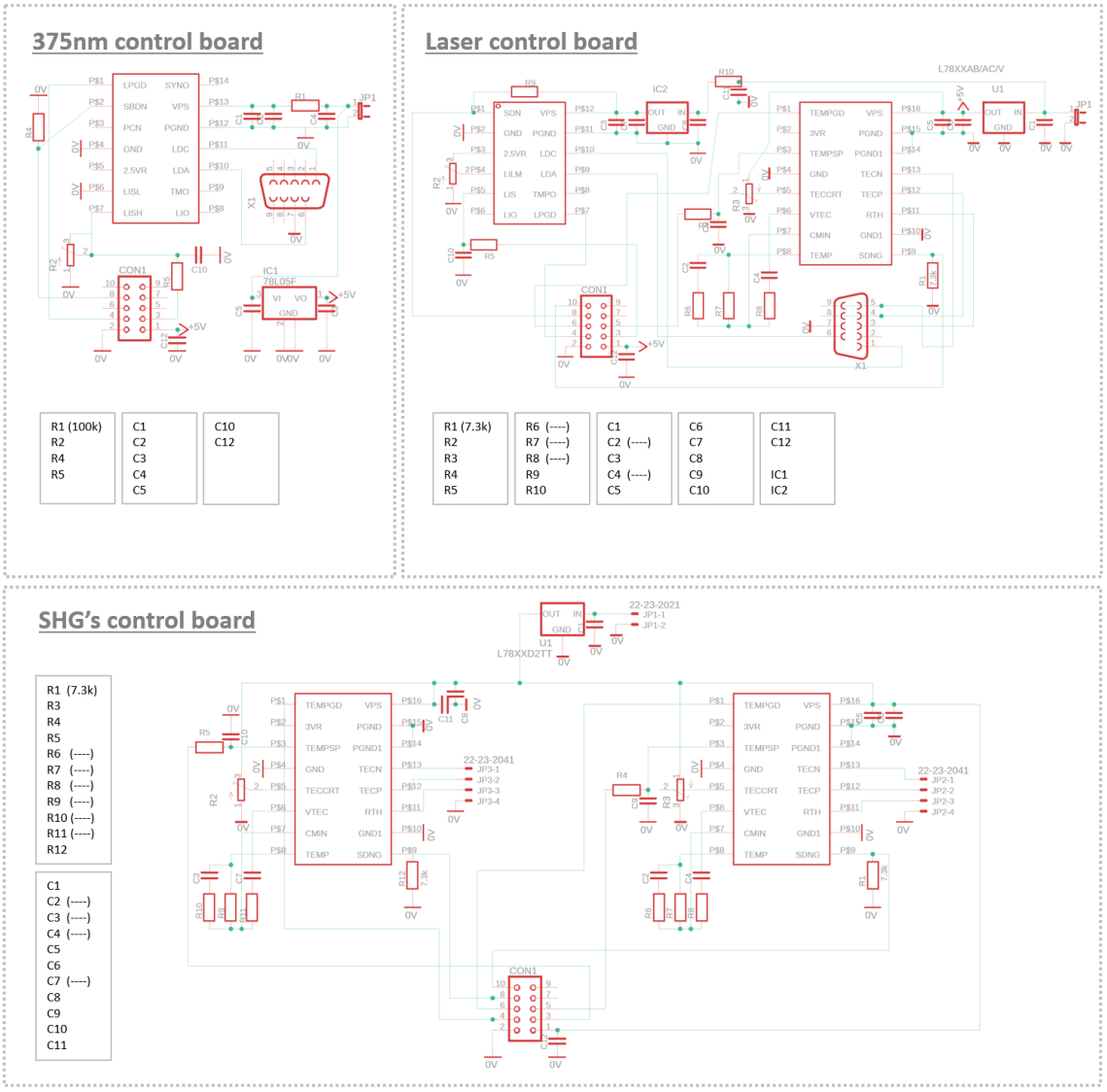

Figure 3.5: The schematics for the control boards for the laser modules, the 375 nm variant and the board driving the two SHGs. Each board is powered by a two pin jumper input labelled JP. The control input is labelled CON1. For both the Laser control board and the 375 nm control board the pin configuration is the same, with a few pins being redundant on the 375 nm control board. The output for the two laser boards is indicated by a D-sub connection, for the SHGs they output via two separate four pin jumper outputs. The blanked-out values are described in the assembly section. All designs were created by Professor Keller.

3.2.4 Laser system housing

The laser system is housed inside an aluminium housing with fiber management. The aluminium frame acts to distribute the heat of each laser module, the AOM and the two SHGs, while also maintaining a rigid support for all components. An additional heat sink is clamped onto the outside of the housing where the AOM is mounted for additional heat dissipation. The fiber outputs and the electrical inputs are formed on a single removable panel, allowing for ease of cable management during assembly. The fiber management is designed to never exceed the minimum bend radius (13 mm) of the used single mode polarisation maintaining fibers it secures. It has channels with varying positions and directions intended to allow multiple fibers with varying lengths to be housed securely with minimal slack. Each beam splitter tube is mounted on the fiber management tray and clamped in place. The tray is made from a 3D printed plastic allowing a light weight and rigid construction. The complete laser system design can be seen in figure 3.6.

3.3 Assembly

In this section the fabrication of the laser system and the characterisation is presented. This starts with the construction of the two types of laser modules and their characteristics. This is followed by the splicing of each of the components and their operation. Then the laser systems housing and fiber management and the completed system is shown.

3.3.1 Mercury laser

3.3.1.1 Control board setup

The Mercury package starts by mounting the diode into the conversion block with a small application of thermal compound on each contact face. The use of thermal compound ensured efficient transfer of the thermal power from the TEC to the mounting block. The laser package was mounted to the frame with another bridge of thermal compound and fixed to the frame via four screws.

The electrical connection for the Mercury package is via their TOSA flex cable, which is converted to a D-sub via an in-house fabricated PCB (see figure 3.8 d).

The laser is tested using the TEC controller evaluation board (Analogue technologies, TECEV104). The feedback loop for the TEC drivers is configured to minimize the response time of the thermal control loop and the dynamic temperature tracking errors, while keeping the control loop stable. This is done by tuning the resistors [R6, R7, R8] and

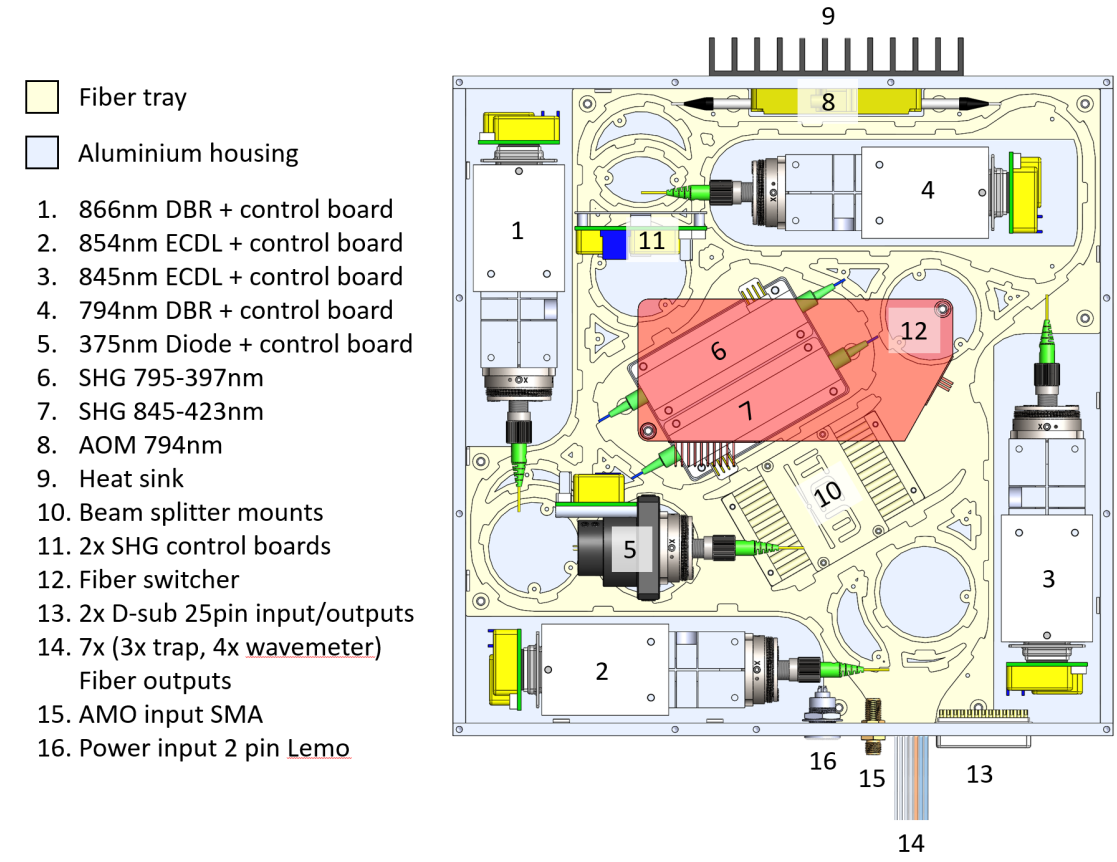

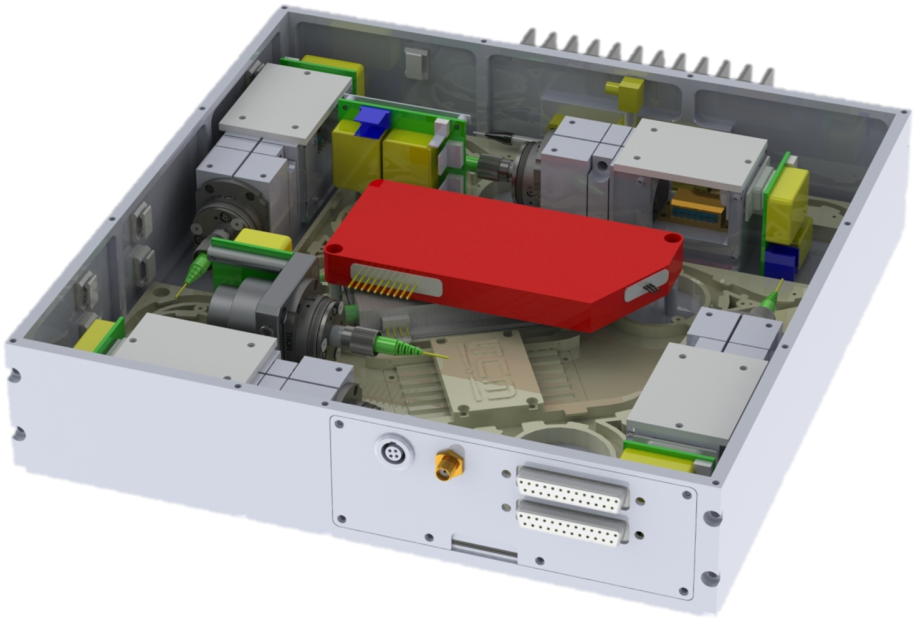

Figure 3.6: TOP: Overhead schematic view of the laser system. BOTTOM: 3D render of the laser design total dimensions of 275 x 260 x 56 mm. Original drawings made by Dr Gonzalvo.

capacitors [C2, C4] around the feedback loop. The best response was viewed using an oscilloscope and adjusting the set point. The optimised values were found to be: R6: 2 MΩ, R7: 1 MΩ, R8: 200 kΩ, C2: 200 nF and C4: 2.2 μF.

The maximum current the TEC can be supplied by the controller is set. This set point (Voltage) is indicated in the specification sheet. For the Mercury package a threshold of 3.0 V cosponsoring to 1.1 A maximum drive current is set. This was set using the R3 variable resistor and the voltage was measured on the TECCRT pin. The thermoelectric coolers are the same for both the 794 nm and the 854 nm lasers, therefore the same values were used in both control boards.

Using the low noise laser driver evaluation board (Analogue Technologies, ATLS1A103DEV1.0) the maximum current limit was set. The evaluation board allows a simulated laser diode to be run with the controller to ensure that the setup does not harm your intended laser package. This was set by adjusting the R2 variable resistor to 200 mA (2.27 V) for the 794 nm and 180 mA (2.05 V) for the 854 nm laser.

The completed laser control board was connected to the lasers D-sub. The control board was driven using a manually adjustable in-house fabricated laser test board (see figure 3.7). The driver board connected to the laser controllers via an eight pin input/output connector and a two pin power connector powering the board. Each laser was turned on and checked for lasing threshold.

3.3.1.2 Laser module assembly

The optical isolator was placed inside the frame and rotated to maximise output power as verified with an optical power meter.

Each fiber launcher was pre-collimated. This was done by coupling laser light of the desired frequency into a fiber and plugging the fiber into the coupler. The launcher was then collimated by observing the free space propagation over a distance of several meters and adjusting the z position of the collimation lens until the beam was collimated. The coupler was then mounted to the laser frame. A multi-mode (MM) with a 50 μm core was plugged into the launcher and coupled to a power meter. The x and y positions of the fiber launcher were power optimised followed by the z position which was incrementally adjusted to maximise the coupled power, before the tilt was maximised. Once the MM fiber was optimally coupled it was replaced with the 99/1 fiber beam splitter input arm. The pre-coupling of the MM fiber makes swapping to the SM fiber easier. Once a few μW of power was coupled the 99% output arm was connected to a polarimeter (Thorlabs,

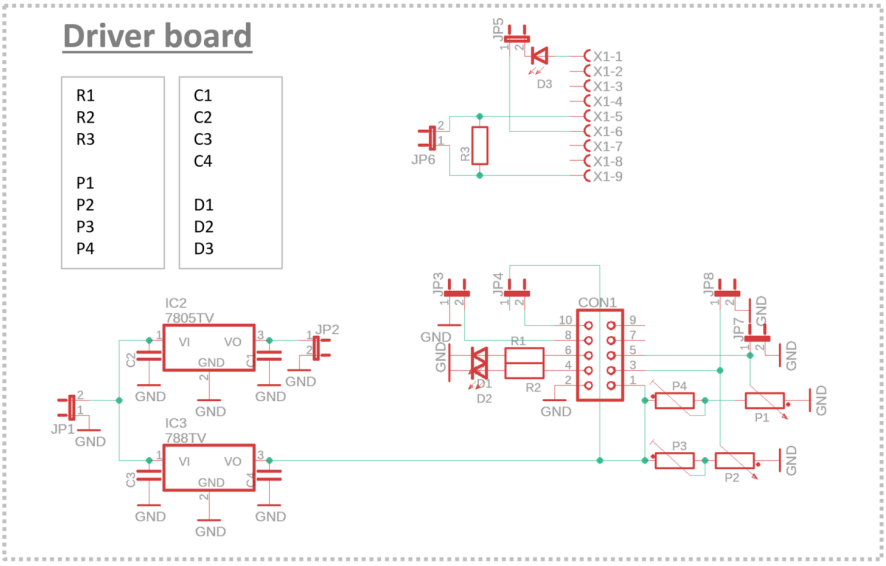

Figure 3.7: Schematic overview of the driver board used to drive the lasers during fabrication. JP2 was used to power the boards. JP7 and JP8 were used to read off the voltage across the potentiometers, giving an indication of the set point. D1 and D2 were LEDs indicating where the feedback on the Analogue Technologies chips were feeding back correctly. The top independent circuit was used as a basic test board to mimic resistive load and drive a LED. JP6 was used to measure the voltage across the TEC and JP5 was used to measure the drawn current to the LED. Designed by Professor Keller.

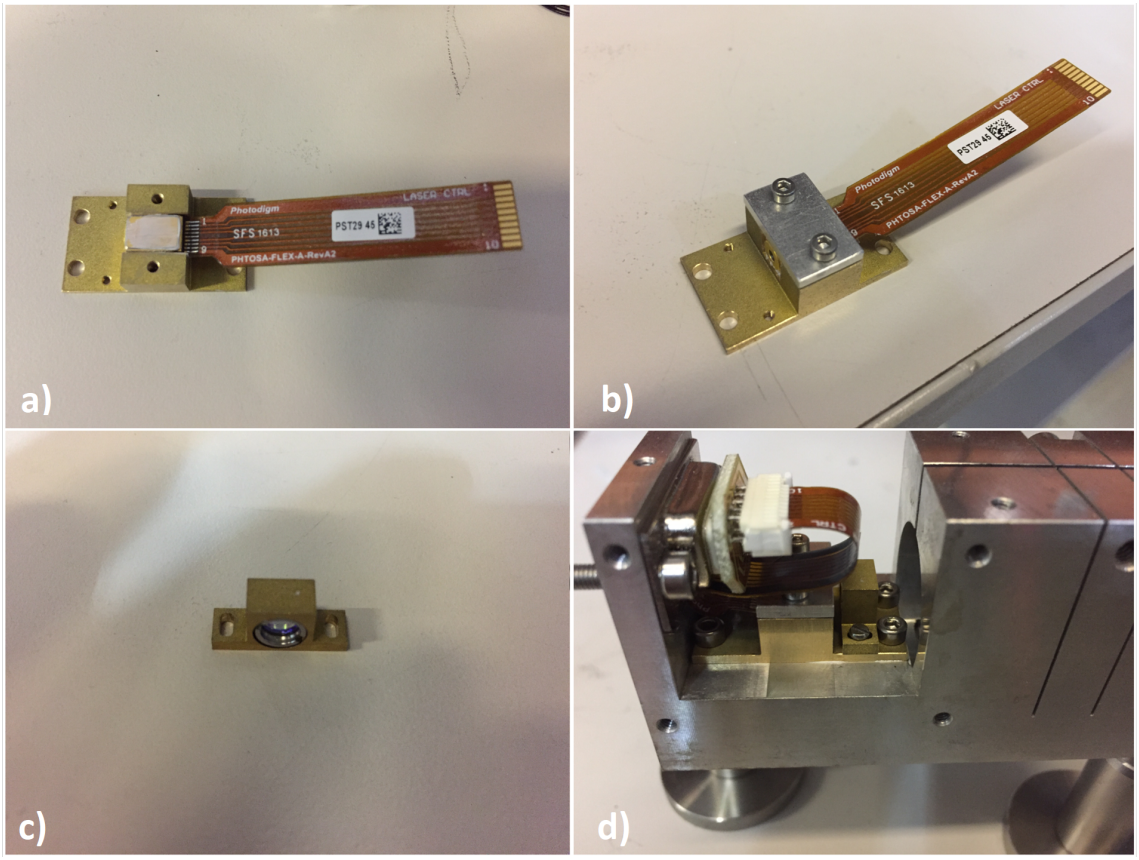

Figure 3.8: a) Shows the mounting of the mercury laser into its conversion block with thermal paste being pre-applied. b)This shows the top clamp that is fixing the laser into the block. c) The corrective lens used to increase coupling for the mercury package. d) Shows the frame with the mercury package and corrective lens mounted and the electrical connections converted to the D-Sub.

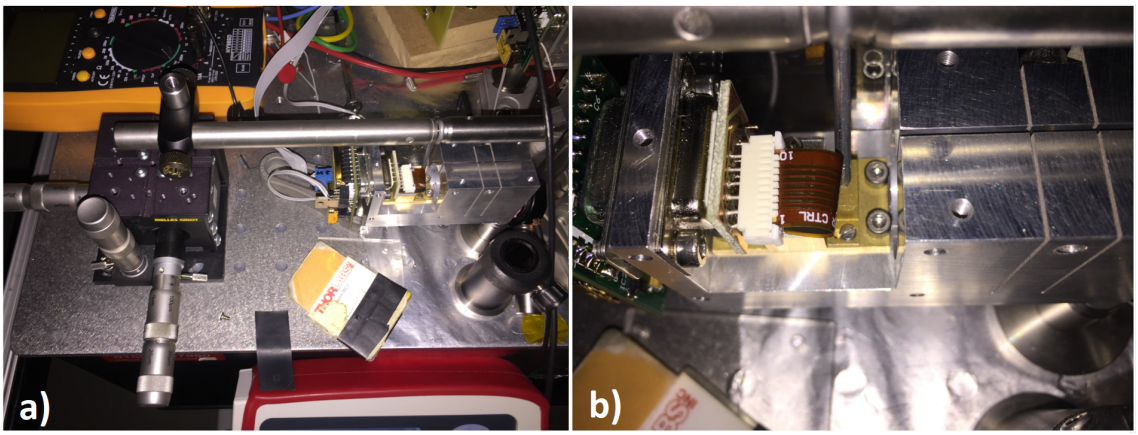

Figure 3.9: a) Three axis alignment stage and the arm that was attached to the corrective lens. b) Close up image of the arm that attached the corrective lens.

PAN5710IR1). The optimisation of the polarisation extinction ratio (PER) was done by loosening the front three clamping screws to allow the fiber port coupler to be rotated. This was done incrementally by hand whilst re-optimising the power to ensure enough light was coupled for the polarimeter to read. This process was done with each laser. Once the PER was maximised the coupling was more thoroughly optimised. Both Mercury lasers suffered from an astigmatism in their emission profiles, which made the coupling efficiency $< 5\%$. This had to be corrected, due to the power critical nature of the laser (794 nm) with multiple high loss systems being fed (AOM, SHG, 50/50). To correct the astigmatism a aspheric lens was used (Thorlabs, N414TM-B). The positioning of the lens required precise alignment to maximise coupling into the fiber.

The lens alignment was done using a craned arm attached to a three axis translation stage. The lens was attached to the crane arm via a small application of super glue. The lens was adjusted on the translation stage the coupler adjusted to maximise the coupling (see figure 3.9). This method worked well and increased the coupling to 30.4% for the 794 nm laser with a polarisation extinction ratio (PER)of $29.57dB$. Once the lens was aligned it was secured using two clamping screws and the mounting arm was detached.

With the laser functioning and coupled to the 99/1 splitter the lasers were tested. The lasers at fixed currents (1 V on current set pin) had there TEC set points scanned in both directions to measure there mode structure. Along with this their currents were scanned with a fixed TEC again to measure the mode structure. These measurements would give an indication as to the types of laser control would be needed to program for each laser. Figure 3.10 shows both, the 794 nm and the 854 nm scans. Each laser has a very broad mode hop free operational area, with the 794 nm laser with a fixed current showing no

mode hop across the full scanned range of the TEC. There can be seen hysteresis on the 854 nm scan and only around the mode hop, if this is avoided then automation of these lasers can be simplified. The currents were also scanned with fixed temperature set more mode hops can be seen across this span indicating that a combination of slow feedback to the TEC and fast to the current would likely give the best long-term stability.

3.3.2 Micron laser

3.3.2.1 Control board setup

The Micron laser package is directly mounted to the frame and thermal paste is added to ensure good thermal transfer. This is designed, so that the lasers beam axis is centred to the other components.

The electrical connections are bridged using push pin connectors and wired up to the D-sub mounted to the frame. This reduces the dangers of direct soldering to the laser package.

Using the TEC controller evaluation board [Analogue Technologies, TECEV104] the laser is powered on. The feedback loop for the TEC drivers is configured to minimize the response time of the thermal control loop and the dynamic temperature tracking errors, while keeping the control loop stable. This is done by tuning the resistors [R6, R7, R8] and capacitors [C2, C4] around the feedback loop. The best response was viewed using an oscilloscope and adjusting the set point. The optimised values were found to be: R6 (1 MΩ), R7 (1 MΩ), R8 (100 kΩ), C2 (1 μF) and C4 (1 μF).

The maximum voltage limit, the TEC can be supplied by the controller, is set. For the Micron laser a threshold of 2.18 V equalling 2.0 A maximum drive current is set. This was set using the R3 variable resistor and the voltage was measured on the TECCRT pin.

Using the low noise laser driver evaluation board (Analogue technologies, ATLS1A103DEV1.0) the maximum current limit was set. The evaluation board allows a simulated laser diode to be ran with the controller to ensure that the setup does not harm your intended laser package. This was set by adjusting the R2 variable resistor to 100 mA (1.13 V) for the 866 nm and 150 mA (1.70 V) for the 845 nm laser.

The completed laser control board was connected to the D-sub. The control board was driven using a manually adjustable in-house fabricated laser test board. This is shown in figure 3.7. The driver board connected to the laser controllers via the eight pin input/output connector and a two pin power connector powering the board. Each laser was turned on and checked for lasing threshold.

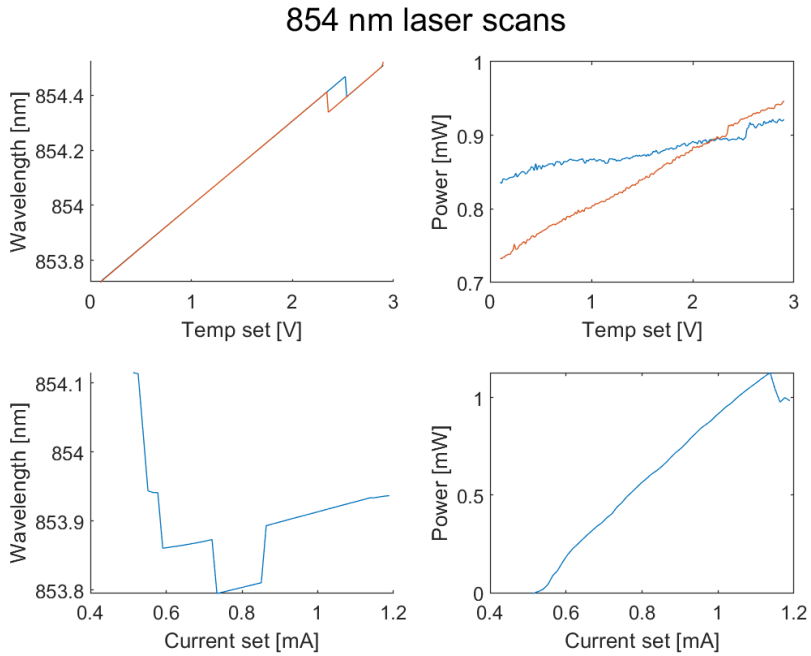

(a)

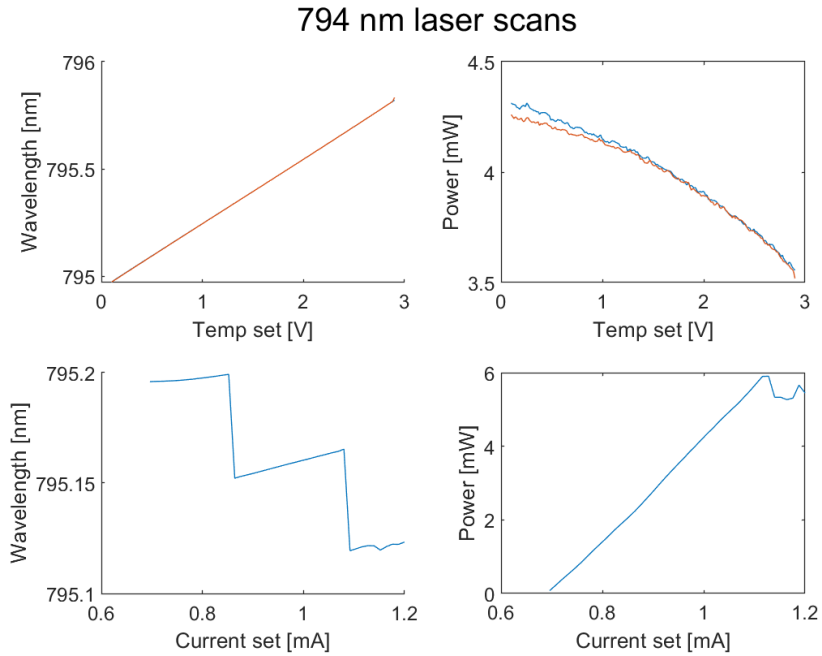

(b)

Figure 3.10: Characteristics of the 854 nm and 794 nm lasers. Each temperature scan was taken both, increasing (blue) and decreasing (orange) at a fixed set current of 88.6 mA. Each current scan was taken as a fixed set temperature voltage of 0.72 V. The data indicated that there is hysteresis in the lasers. Original data taken by Dr Gonzalvo.

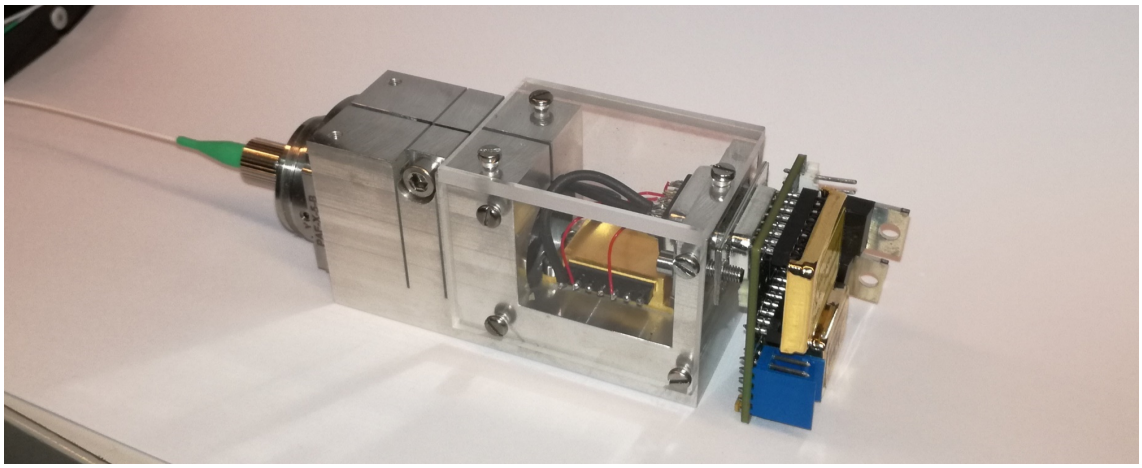

Figure 3.11: The complete Micron laser module.

3.3.2.2 Module Assembly

The optical isolator was placed inside the frame and rotated to maximise output power as verified with an optical power meter.

Each fiber launcher was pre-collimated using the same method described in the Mercury package assembly. The complete module can be seen in figure 3.11.

The lasers mode hop free range was measured in both directions to gauge if there was any hysteresis. The current was fixed and the temperature set point was scanned from minimum to maximum and vice versa. This would indicate the mode hop free range of the laser and if there was any and hysteresis. Figure 3.12 shows, both the 866 nm and the 845 nm laser scans. Each laser has a short mode hop free range scanning the temperature, with only a small amount of hysteresis. The current scans have less of an impact in triggering mode hops, therefore the Micron laser benefits favors feedback on the current. Intelligent programming will have to be employed to ensure mode hops are dealt with correctly.

3.3.3 Laser stability characterisation

The Micron and Mercury lasers stability was checked over different time ranges, indicating how they would perform as a black box once in operation.

A beat note measurement measures the effective linewidth. Each of the laser modules was overlapped with one of the tabletop lasers of the same frequency available in the laboratory. For the Micron laser the 866 nm was used and for the Mercury the 854 nm. The tabletop lasers were referenced to a caesium cell via a scanning cavity lock[62]. From previous measurements of the scanning cavity lock each of the tabletop lasers attached had a linewidth of ≈60 kHz at 1 ms. This low linewidth means, that when performing a

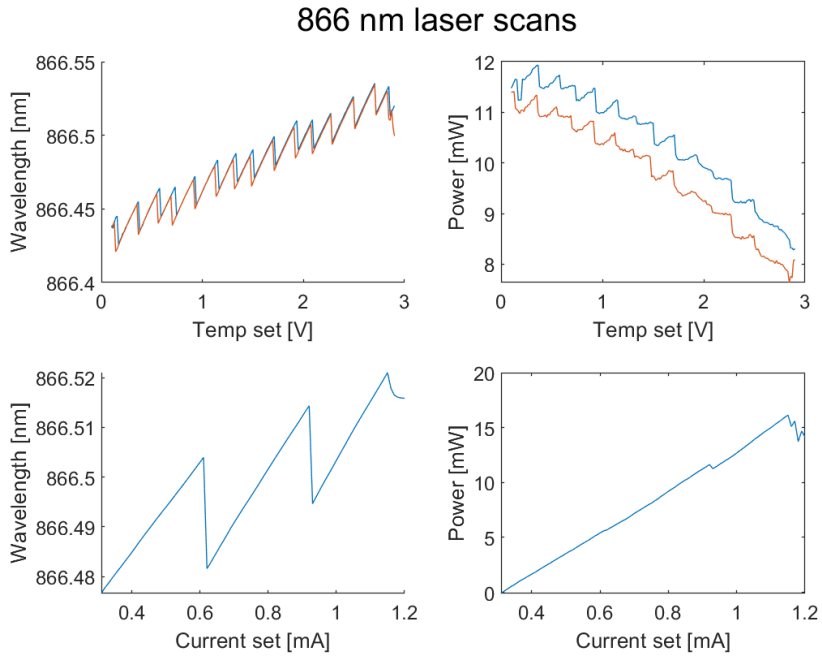

(a)

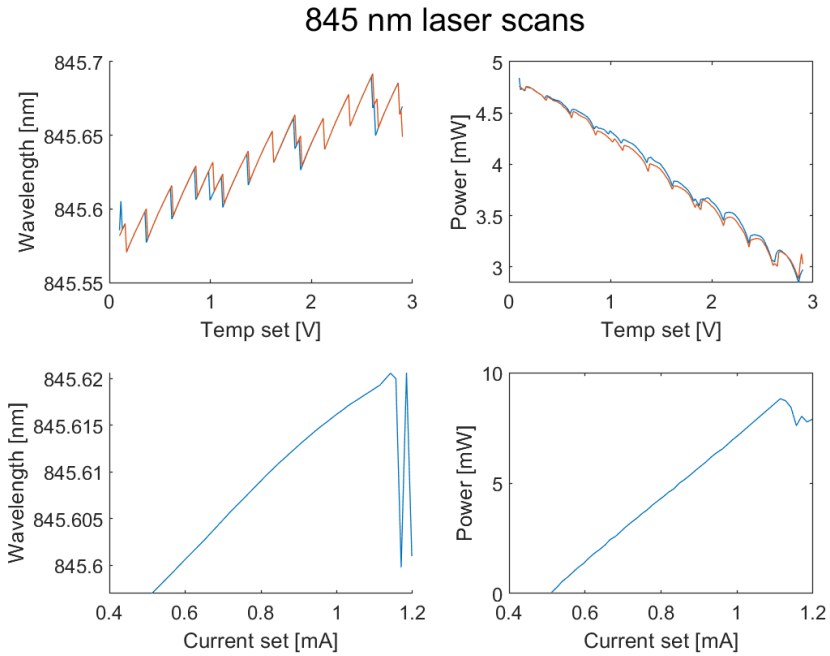

(b)

Figure 3.12: Characteristics of the 866 nm and 845 nm lasers. Each temperature scan was taken both, increasing (blue) and decreasing (orange) at a fixed set current of 71 mA. Each current scan was taken as a fixed set temperature voltage of 0.72 V. This indicated that there is hysteresis in the lasers. Original data taken by Dr Gonzalvo.

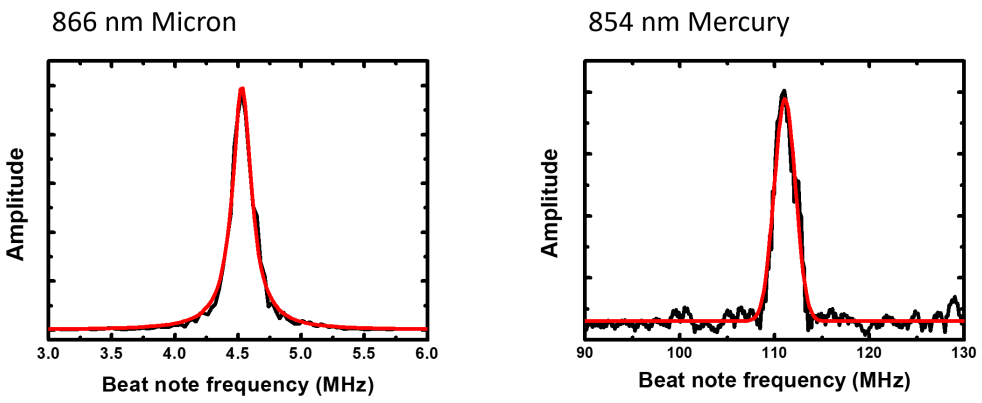

Figure 3.13: Beat note measurement for the Micron and Mercury lasers. The 854 nm (Mercury) had a Gaussian fit with an R^2 value of >0.95. The 866 nm (Micron) had a Lorentzian fit with an R^2 value of 0.99. The Mercury 854 nm full width at half maximum is 2.41 MHz at 1 ms and the Micron 866 nm laser full width at half maximum of 180 kHz at 1 ms.

beat note, the portable lasers should dominate the beat width. The Mercury 854 nm laser was found to have a full width at half maximum of 2.41 MHz at 1 ms (see figure 3.13), with the quoted linewidth between 1-10 MHz. For the Micron 866 nm laser a linewidth of 180 kHz at 1 ms was measured, the quoted linewidth of the laser was typical 100 kHz at 1 ms. This indicates that both laser control boards do not broaden the natural linewidth of each laser. The lasers stability and their free running drift was measured. This was done by turning the laser on and measuring their wavelengths and powers over ten hours whilst free running. The results for the 794, 845, 854 and 866 lasers are shown in table 3.3.3. A figure of each lasers characteristics is shown in 3.14.

Frequency [nm]	**Laser**	**Total drift [GHz]**	**Stable drift [MHz]**
866	Micron	3.96	1.025
845	Micron	1.13	1.483
854	Mercury	1.77	2.081
794	Mercury	2.43	2.765

Table 3.4: This lists the measured uncompensated drift of the lasers. The stable drift was taken as the standard deviation of all measured values, taken after the lasers were running for two hours. The total run time of each laser was in excess of 8 hours. The total drift was taken as the maximum minus the minimum recorded wavelengths.

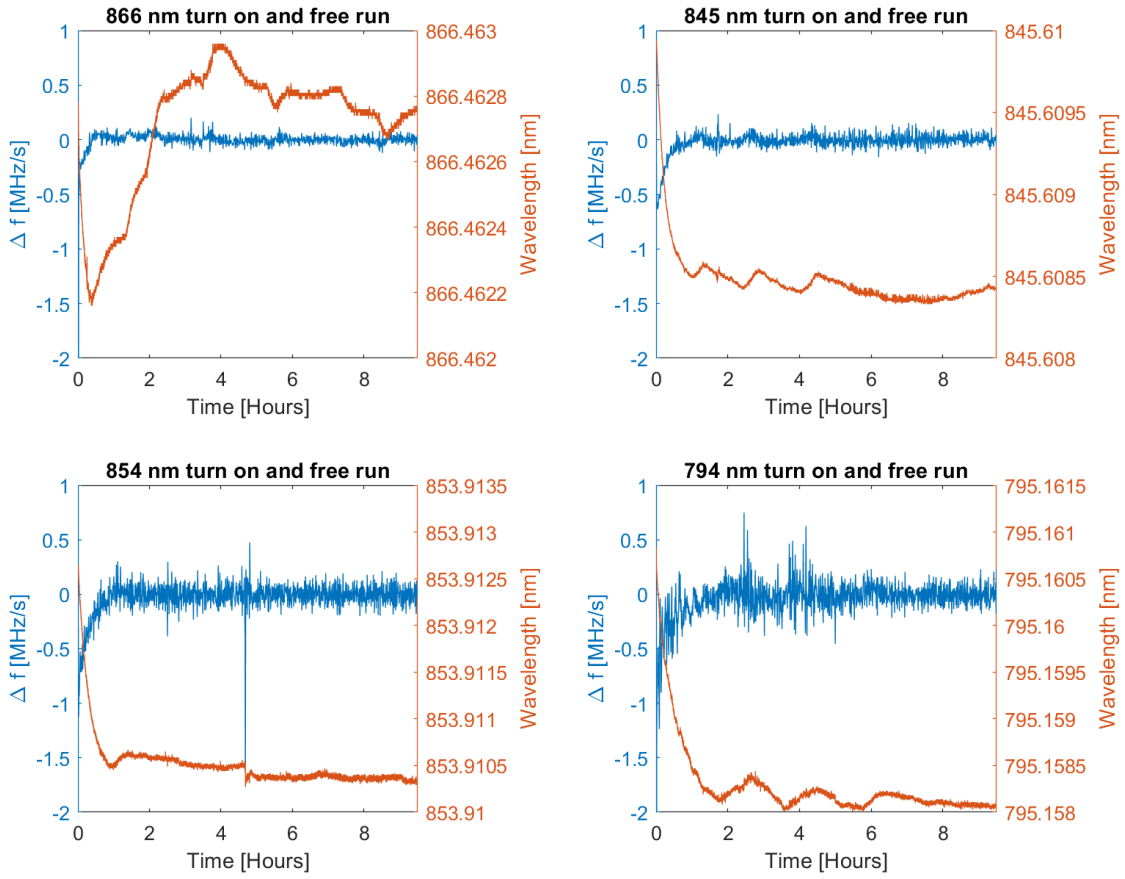

Figure 3.14: The plots show the laser drift and stabilisation time. This data for visualisation was cropped taking out the first 30 seconds and the Δf scale is fixed. This was done to highlight any underlying features of the drift and highlight the stability differences in the types of laser. Original data was taken by Dr Gonzalvo.

A long-term frequency stability test was setup to check if the lasers remained stable and mode hop free over an effective operational period (a month). To do this the laser was driven by a constant TEC set point and the current was locked using a computer and an in development laser driver board based on a 12 bit PIC micro-controller. The driver acts as a digital to analogue converter (DAC) and interfaces with the computer running a feedback loop. The lasers power and wavelength were measured. The 1% arm of the 99/1 fiber splitter was connected to a wavemeter and the 99% arm to a calibrated photo diode to give an indication of power drift. The laser system was mounted on a optical table

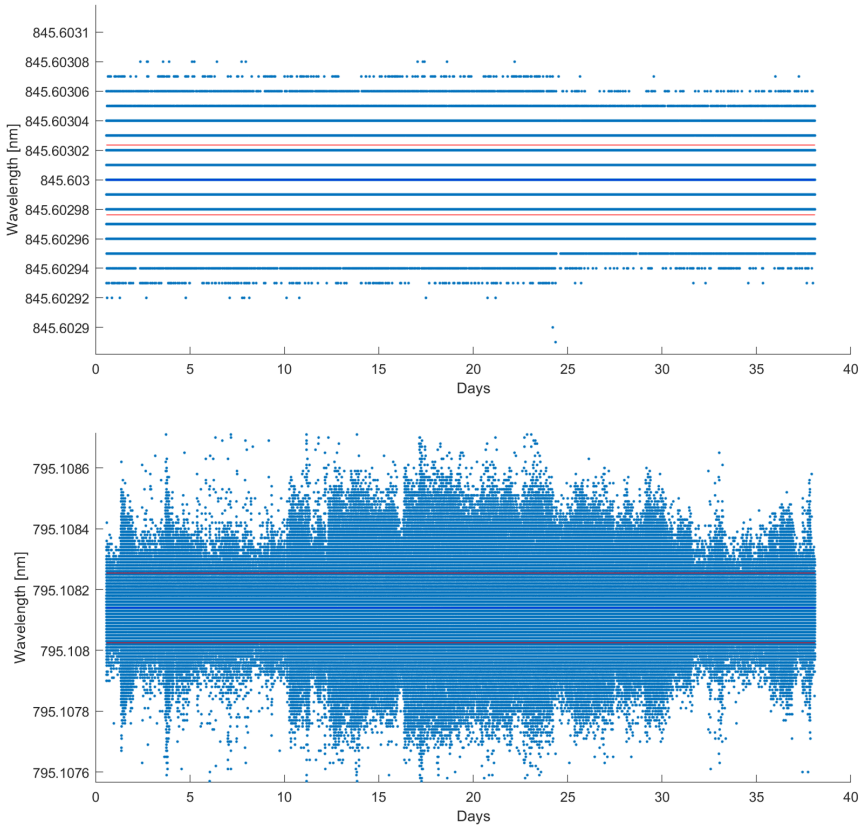

Figure 3.15: The graph shows the laser stability over a month. The red bars indicate the standard deviation of the mean. The results highlight the bit rate limitations of this 12 bit PIC controller. Original data taken by Dr Gonzalvo.

used for the laboratories laser system. The portable lasers were left locked over a month. The laboratory is a controlled environment, but the laser table was actively used over the course of this month with the laboratory also suffering from temperature fluctuations of around 5°C due to the air-conditioning system. The microcontroller architecture limited the lock on this measurement due to its 12 bit resolution causing large steps to occur in the feedback. A trace of the lasers wavelengths locked by the microcontroller over this month can be seen in figure 3.15, the digital steps due to the controllers lack of resolution are notably visible. The lasers did not mode hop or drop out of the lock over the tested period. The standard deviation of the lasers over the course of the lock was 54.43 MHz for the 794 nm Mercury laser and 9.914 MHz for the 845 nm Micron laser. This would be expected to be much lower with a greater than 12 bit controller.

3.3.4 System components

All other optical components in each branch are spliced together sequentially. Each component was purchased connectorised, this meant that each component could be tested prior to splicing to ensure the splice did not degrade the performance. When ready to splice each component had their connectors removed and the protected sleeve and coating stripped back. Then the fiber was washed, before it was cleaved using a fiber cleaver (Fujikura, CT-101) at a tension of 180 gF. The splicer (Fujikura, ARCMaster R FSM-100P+ Fusion Splicer) can splice polarisation maintaining (PM) fiber using the end view method. This method aligns the stress rods for extremely high PER reduction due to splice misalignment. A default end view PM splice mode was modified to each fiber used specification. After each use the splicer gave calibrated read outs of the quality of the splice and the PER expected. If the measured PER was below 30 dB the process was repeated. This ensured the splice never limited the PER of the laser.

Each laser branch was mounted onto the bottom plate after the fiber management tray was fixed. The beam splitters were mounted to the tray and the fiber was rooted. The SHGs were mounted to an aluminium pedestal with a small application of thermal compound and four screws each. The aluminium block was directly mounted to the bottom plate allowing good thermal distribution of the SHGs heat. The AOM was also mounted using thermal compound to the side plate. The portable laser system can be seen in figure 3.16.

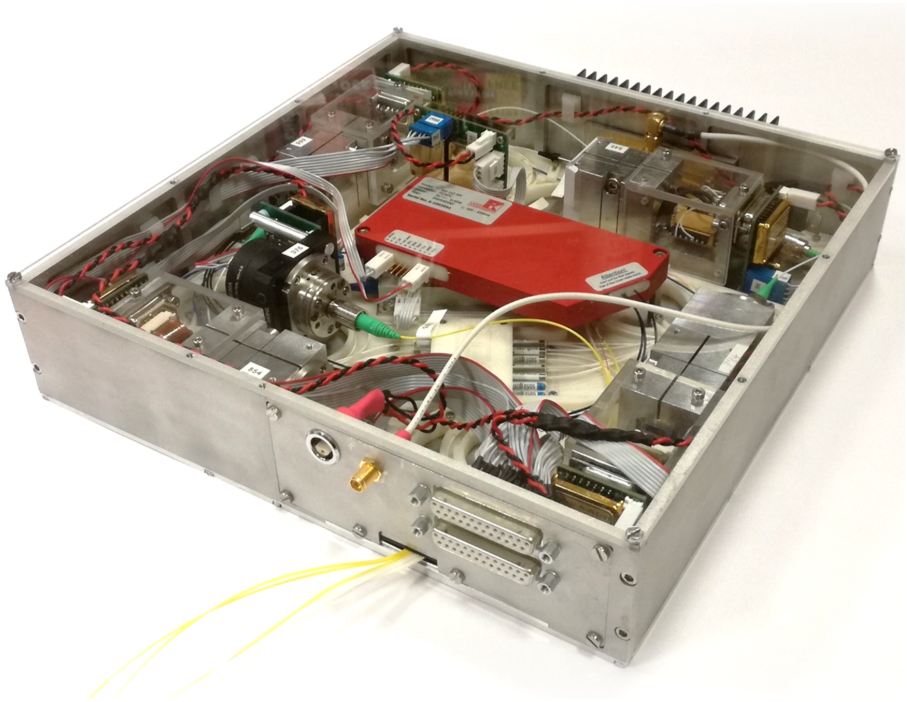

Figure 3.16: The fully fabricated laser system is shown.

3.4 Ion trapping

The fabricated laser system required testing to ensure the lasers behaved as expected interacting with an ion. Therefore, the portable laser system was connected to an existing blade trap that has been extensively used for the past ten years. This trap acted as a good way of testing the stability of the lasers and the functionality in its packaged format.

3.4.1 Experimental setup

The lasers that controlled the blade trap were situated on a different optical table as the trap. This meant fibers were already in place and aligned to the trap for each needed beam. This made coupling the portable system to the trap easy, as the fibers from the laboratory based laser system could be disconnected and coupled directly to the portable system (see figure 3.18). The portable system was mounted onto the vibration isolated table that houses our laboratory based laser system used to drive the trap. The three trap output fibers of the laser system were fiber mated to the input of the trap. The four outputs to the wavemeter were connected to a fiber coupled switcher used by the wave meter [HighFinesse, W7].

The laser system was controlled by a driver board (in development) based on a PIC microcontroller. This acted to control the portable laser system, but with BNC connectors for the outputs. This driver was connected via mini USB to a computer and controlled

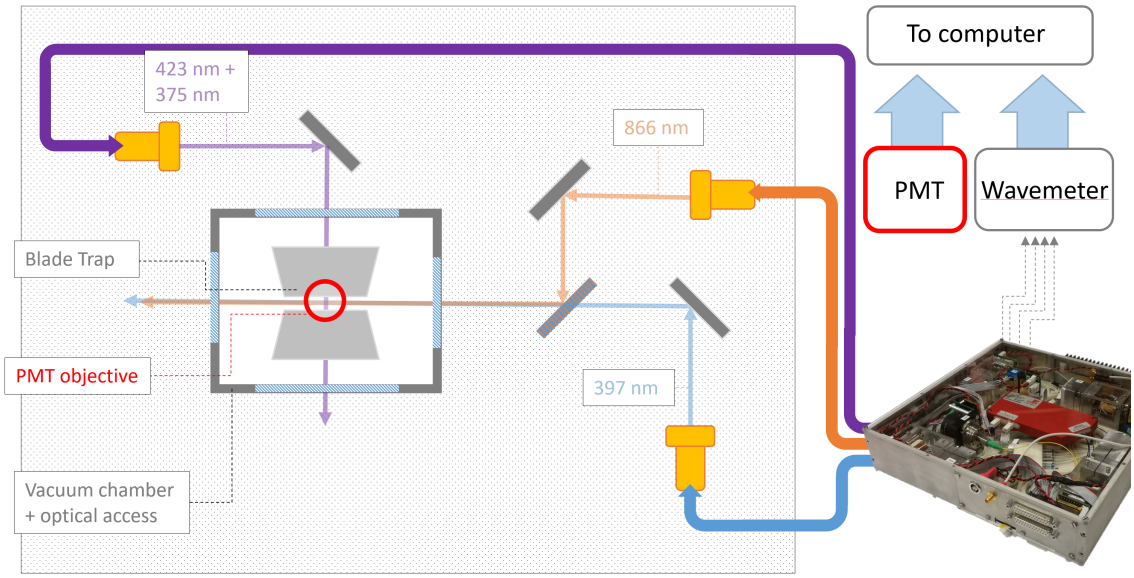

Figure 3.17: This figure shows the used layout of the lasers and trap, when coupling the portable laser system to the "blade" trap.

via a LabView interface. The LabView interface allowed adjustment of the set point for each of the lasers and SHGs controllers manually. Although each lasers wavelength was visible on-screen, active locking was not setup at this point. A layout of the control loop can be seen in figure 3.18.

3.4.2 Trapping

In order to trap and cool an ion, the cooling (397 nm), re-pumping (866 nm) and photo-ionisation (423 nm, 375 nm) lasers are required. For this test the quench laser (854 nm) was not used. The optical switcher used for choosing between the second cooling laser or photo-ionisation lasers was set to the photo-ionisation lasers. The fiber AOM was driven using an external function generator and amplifier.

Each lasers frequency was steered to the known frequencies verified by another active trap. Using the wavemeter values as a target, each laser was tuned manually via the LabView interface varying the set point voltages of each laser TEC and current controller. Once every laser was steered to the correct wavelength the oven on the trap was run and the photo-ionisation shutters were opened.

An Ion was trapped and cooled with manual steering of the cooling frequency. Once loaded the oven was turned off and the photo-ionisation shutters were engaged. Using just the cooling beam and the re-pump laser, manual steering of the cooling beam was able to keep the ion trapped and fluorescing over tens of minutes. A picture of the trapped ion

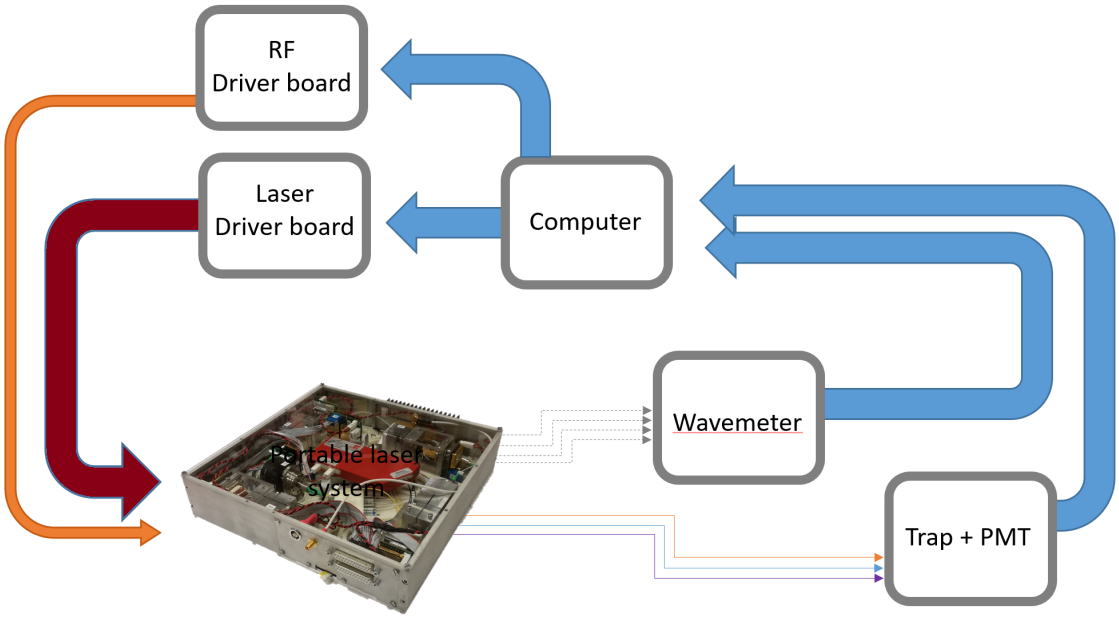

Figure 3.18: Schematic overview of the feedback loop of the laser system in this test. The blue lines indicate digital signalling, the orange analogue RF and the purple analogue DC.

can be seen in figure 3.19.

This test showed the lasers system behaved beyond expectations with regards to its overall stability. No active wavemeter lock was used, just manual steering. The laser system managed to achieve photo-ionisation and stable cooling of a single trapped ion with the entire system smaller than 0.4 liters in volume.

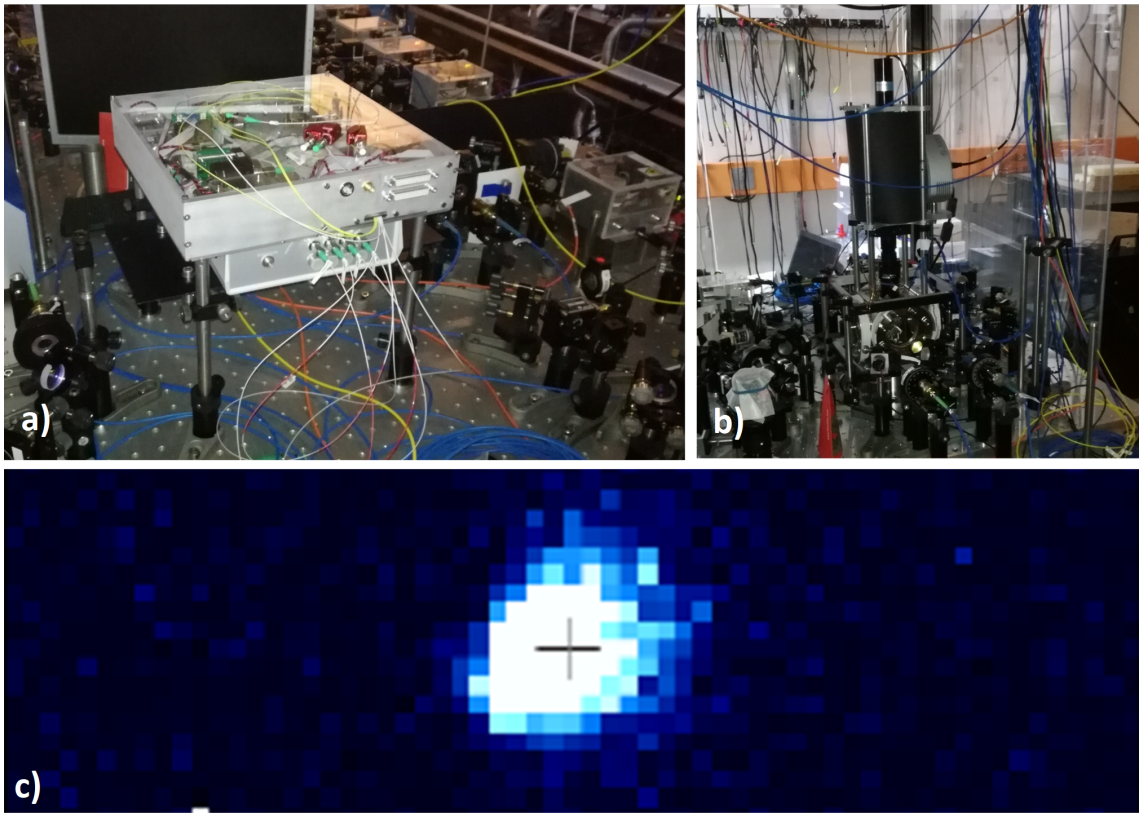

Figure 3.19: a) Shows the portable laser system. Below the laser system the fiber switch can be seen with the four outputs plugged into it, which are fed to the wavemeter. b) Shows a working blade trap with the portable laser system integrated into it. c) Shows the trapped ion florescence being driven by the portable laser system.

Chapter 4

Trap design and assembly

This chapter discusses the fiber integrated ion trap. It begins by giving an overview of what an ion trap consists of in a laboratory environment, its constraints and how integrating fibres allows a portable system to be realised.

The next section explores the reasoning behind the trap design. This gives a detailed breakdown of the integrated fiber solutions used for beam delivery and fluorescence collection, how the trap design allows for these to be integrated and mounted monolithically, followed by the novel solutions for fiber optic feedthroughs in a highly compact vacuum system.

The last section focuses on how the system is put together with detailed explanations of fabrication methods and techniques, highlighting the problems faced and the solutions provided.

4.1 Overview

An ion trap is designed to confine an ion in a highly isolated environment. It consists of the needed electrodes configured in the geometry desired along with the support structure. On top of this it needs to facilitate a loading area where by an atomic beam can be used to seed for ionisation and ion loading. Furthermore optical access is needed to allow for the necessary lasers to photo-ionise, cool and manipulate the ions state.

Lab based ion traps tend to occupy $>$ 100 l in volume, weighing in excess of 100 kg and require large electrical power consumption. The ion traps themselves tend to be relatively small compared with the surrounding structure occupying 10 cm^3, what makes them so spatially demanding is optical access. Laboratory based systems use free space laser delivery and fluorescence detection. These require a fixed frame around the trap

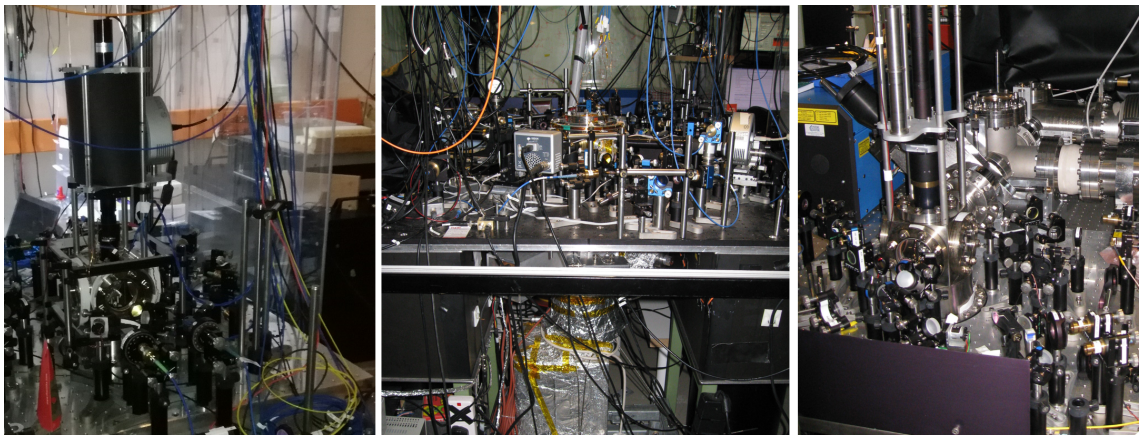

Figure 4.1: Three examples of Ion traps and the surround infrastructure

to ensure the optics needed remain coupled to the ion. To access the ion large ultra high vacuum (UHV) windows are needed in the vacuum chamber to ensure the lasers and fluorescence detection systems can be couple to the ion in a variety of angles. These large windows make the vacuum structure much larger than the trap and in turn require larger pumps to maintain the UHV required. Furthermore, these systems require maintenance due to their large footprint and adjustable alignment. Free space optical access makes ion traps complex, large, and they require input for constant use. Examples of ion traps and their surrounding infrastructure can be seen in figure 4.1. All of these issues can be addressed by using optical fibers.

The trap for this project needs to achieve these criteria:

1. Predictably trap a single ion
2. Maximise signal to noise
3. Maintenance free operation
4. Low SWaP [$<$ 1 l (Volume), $<$ 10 Kg (Weight), $<$ 100 W (Electrical Power)]

One important tool to reach the criteria are fiber optics. Fibers offer a highly compact, flexible, directional light guiding system. Single mode fibers can deliver a single transverse light mode with little to no attenuation or dispersion that maintains its polarisation regardless of the fibers routing over one kilometre[63]. Multi-mode fibers are capable of carrying a wide bandwidth of frequencies in the same fiber with core size close to the fiber width and a large numerical aperture allowing for wide acceptance angles of light to be coupled and guided. Integrating fibers for fluorescence collection and beam delivery into the inherently compact radio frequency (rf) trapping structure eliminates the need for UHV windows and optomechanical supports outside the vacuum system. This heavily reduces the needed SWaP The system also becomes maintenance free by fixing the fibers

to the trap, making the entire structure monolithic.

4.2 Trap Design

4.2.1 Fiber integration

For an atomic clock the stability is underpinned by the signal to noise ratio (SNR). The higher the signal is, the faster the state can be measured, the faster the laser can be steered to maintain resonance, the more stable is the clock. The signal is based on the efficiency of the detector γ_{eff} multiplied by the amount of detectable events I_{flux}. The noise is the contribution of false triggers (dark counts) of the detection device plus the detection of unwanted scattered light. The efficiency of the detector and the dark counts are a property of the detector itself and can be optimally chosen. The scatter collected is a property of the optical purity of the delivery beam and its interaction with the surrounding trap structure resulting in unwanted signals. The amount of collected detectable events is underpinned by the ions emission rate and the way the fluorescence is collected. These considerations frame the trap design but more so the beam delivery and fluorescence collection design.

4.2.1.1 Florescence collection

The standard method of fluorescence collection incorporates high numerical aperture (NA) lenses along with free space propagation, tight apertures to isolate the area of collection, and a Photo Multiplier Tube (PMT) to count the emitted photons. To maximise the signal collected, a higher numerical aperture (NA) lens allows for higher collection of the ions fluorescence, but at the cost of needing to place the lens closer to the ion or make the lens much bigger. This makes practical inclusion of high NA lens close to the ion technically challenging as these lenses tend to be a few 10's mm in diameter and thickness approximately half of the diameter. Lab based systems capture one too two percent of the ions fluorescence and can occupy volumes of $> 10cm^3$. The additional need to use windows in the vacuum system makes the vacuum package larger and more complex. Overall for a portable system using free space collection is too large and comes with a lot of technical compromises. The solution is the usage of integrated fiber optics.

Integrated large core step index multi-mode (MM) fibers, integrated into tubular end-cap electrodes have been shown to collect upwards of six percent[64]. This massive increase is due to the fiber sitting much closer than standard lenses could. The fiber being housed inside the trap electrodes allows for shielding the dielectric fiber from destabilising the

trapping field. It should be noted that it does have an adverse effect on the trap depth[65] but as it the dielectric is tightly integrated into the electrode it remains stable[64].

The used MM fiber (Thorlabs, FG200UEA) was chosen due to its large NA of 0.22 and a large core size of $200\mu m$ for a silica clad fiber. Silica cladding is crucial for the fiber feedthrough as it allows for a low diffusion vacuum seal (more of this is discussed in section 4.3.1.2). Due to the fibers core size and NA, the florescence collection will be maximised when the fiber to ion separation is $< 443\mu m$. With a fiber in each endcap electrode the total collection of the ions fluorescence is 2.45%. This collection will allow for fluorescence collection comparable to that of a lab based system, but with a vastly reduced footprint. It will also allow to maintain a vacuum not limited by windows and have a reduced vibration sensitivity.

The collection fiber sits within the trap electrodes (see part 4.2.2.1) and delivers into vacuum via an integrated fiber feedthrough (see 4.3.1.2). The fluoresence is detected using a compact PMT ([Older version of the new H12386-110]). This boasts a high sensitivity in the UV range.

4.2.1.2 Beam delivery

Ion trapping experiments require lasers to control and manipulate the internal electronic states. The way the laser light is coupled to the ion is commonly via a combination of free space optical mirrors, lenses, and waveplates fixed around the vacuum chamber. Same as with the laser systems, these are mounted on a vibration isolation table. The table reduces the interaction with external vibrations but these systems are not maintenance free and can require re-optimisation every few weeks. This is primarily down to the long path lengths that are still required due to large easily adjustable optics ($>$ 10 cm's) and optical access constraints. The bulk of the system is in the delivery optics around the trap.

The beam delivery for our system needs to address these key criteria:

1. Maintenance free
2. Low volume (to keep with the small form factor of the trap)
3. Minimal free space (vibration insensitive)
4. Optical beam quality (low background scatter)
5. Focal length >5 mm

To achieve this the free space path length needs minimising and the bulky optics need to be compressed. The use of optical fibers delivered into the vacuum chamber via com-

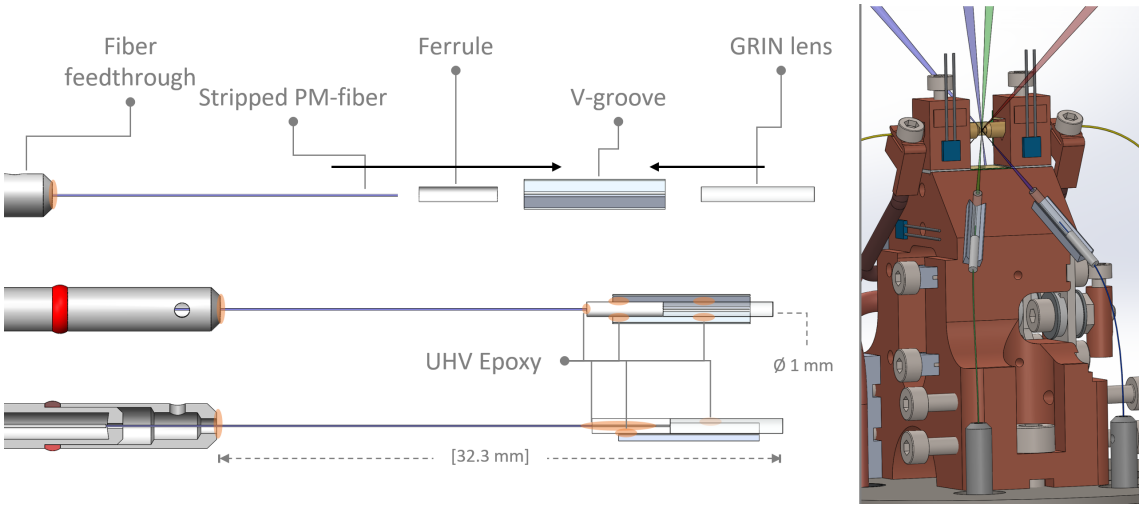

Figure 4.2: This shows a schematic breakdown of the GRIN lens assembly. Original SolidWorks drawing created by Dr Gonzalvo.

pact fiber feed-throughs eliminate the need for UHV windows. Single mode polarisation maintaining fiber further reduces the need for bulky waveplates. Mounting the fibers to the monolithic trap structure will reduce the needed free space between the end of the lens and the ion and couple the two systems together, making it more vibration insensitive.

A single mode fiber has a divergent output which would illuminate the trap structure and cause large background scatter. To address this a lens can be used to focus the beam so that it does not interfere with the trap structure. Having a focused beam requires less power to perform the needed excitations in the ion. A disadvantage of this lensed approach is that alignment becomes critical and must be considered carefully.

The focusing method used is based on Graded-Index (GRIN) lens. These are compact cylindrical lenses that are capable of producing a near diffraction limited spot size with usable focal lengths (>10 mm). GRIN lenses have been used in medical imaging for years, where compact form factors and optical purity is a priority[66, 67, 68].

The assembly (see figure 4.2) is comprised of a single mode fiber centred inside a cylindrical ceramic ferule acting to align the fiber to the same height as the center of the GRIN lens. The GRIN lens and ferrule are secured using a UVH epoxy to a machined aluminium V-groove. This allows for the fiber and GRIN lens to be self aligned based on the tolerance of the ferrule (concentricity $\pm$ 1 μm) and the surface of the V-groove. The GRIN lenses have a focal length of 9 mm.

The assemblies are designed to be aligned to the trap center and secured to the trap structure via UHV epoxy. Once aligned this ensures no misalignment can occur from moving parts. The beams are aligned so that the spot size at the trap center is 20 um,

this is done by setting the focus before the trap center. This is done to ensure the beam will couple to the ion with an acceptable margin of error for the misalignment in the predicted trap center.

The beam delivery fiber is delivered into vacuum via an integrated fiber feedthrough (see 4.3.1.2). The input of these fibers will be spliced to the portable laser system.

4.2.2 Trap design

4.2.2.1 Ion trap geometry

The trap geometry requires these key criteria:

1. Integrate collection fibres
2. Predictable potential
3. Low SWaP

It also requires high secular frequency, deep trap depth and good optical access.

The ion trap design is based on a modified end-cap geometry. This trap geometry has been shown to support fiber integration into the electrodes[64]. The trap generates a three dimensional parabolic trapping potential, making it ideal for trapping single ions. The field is symmetric about the electrodes making the trap position predictable. The geometry has a simple low volume design, allowing it to be driven without the need for high powered amplifiers. This type of trap can be run with the RF signal connected to the inner electrode and the outer electrode connected to ground or vice versa.

The trap depth and secular frequency are a product of the trap geometry. Both of these parameters need to be maximised. The trap depth is a measure of the energy needed by the ion to escape the trap. This can be estimated using the trap pseudopotential. The pseudopotential is modelled using a finite element modelling program using an electrostatic analysis [1] (see figure 4.3). The trap is driven at a frequency of $24.6MHz$.

The electrode structure used in this design is shown 4.4. The trap consists of a pair of electrode assemblies facing each other. Each trap electrode is made from two concentric gold coated copper tubes separated by an alumina spacer.

Copper was chosen for its high conductivity and ease of machining. But when it is exposed to atmosphere it produces a thin oxide layer. Copper oxide is an electrical insulator which poses an issue with the accumulation of patch potentials on the trap electrode surface. For this reason gold is electroplated to the electrodes. Alumina was used due to high electrical insulation and ease of machining with a low dielectric heating

[1] COMSOL Multiphysics

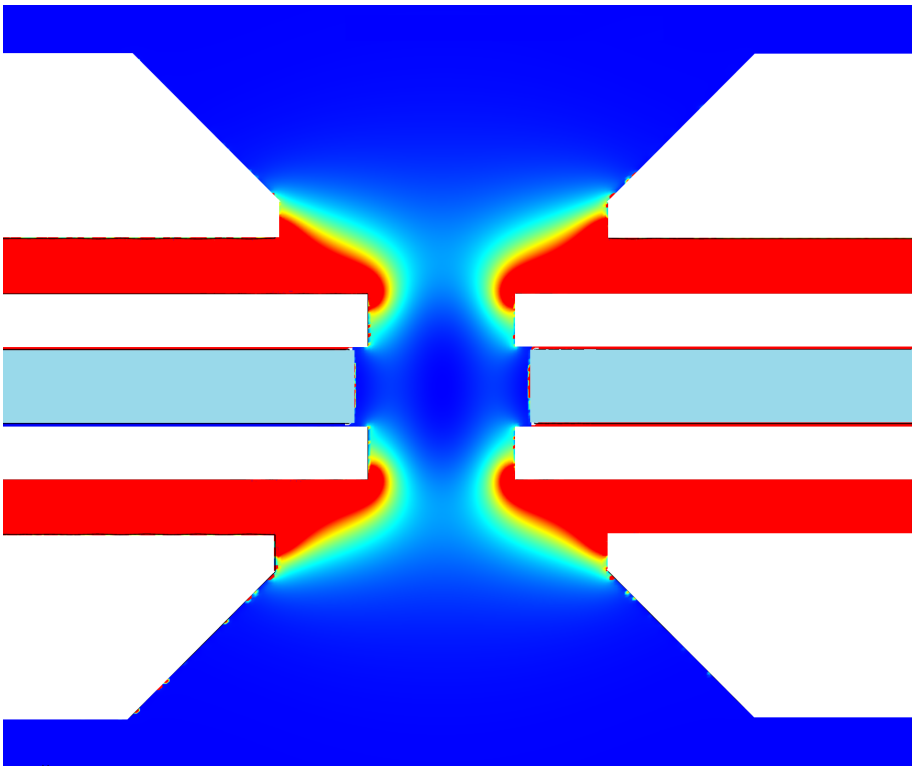

Figure 4.3: The pseudo potential of the simulated trap electrodes. The trap electrodes are indicated in white and the fiber in light blue.

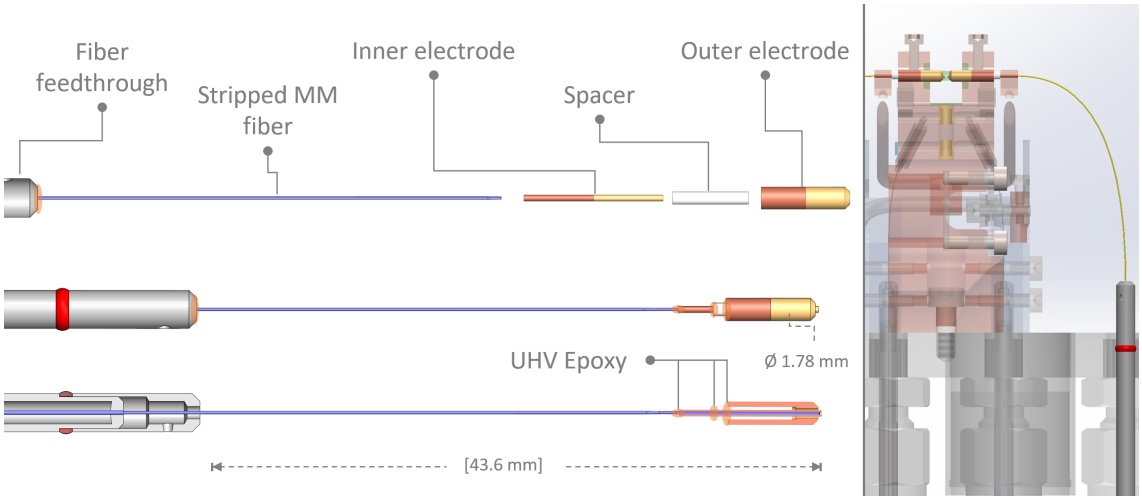

Figure 4.4: This shows a schematic breakdown of the electrode assembly. Original SolidWorks drawing created by Dr Gonzalvo.

rate.

To optimise the balance between fluorescence collection and optical access, the outer electrodes were tapered to 45° and the inner electrodes protrude to intersect the tapered plane of the ground electrodes. The collection fiber fits tightly into the inner electrode and is reassessed by 50 μm. This is done to shield the dielectric surface from the trapping field as well as stray charge deposition.

The inner electrode is made from 99.99% pure drawn copper tube (Goodfellow, CU007100) with a 1 μm gold coating. This copper tube has an outer diameter of 500 μm and an inner diameter of 220 μm. The outer electrode is made from 99.95% oxygen-free high thermal conductivity (OFHC) Copper (Goodfellow, CV007180) tube with a 1 μm gold coating. This copper tube has an outer diameter 1780μm inner diameter 800μm.

The mounting and alignment of the electrodes is critical, as any misalignment will introduce unwanted asymmetries in the trapping field. For this reason each electrode is aligned independently and secured to the main body via UHV epoxy. This is done by aligning two columns. These columns double as the trap electrodes support structure as well as an electrical connection for RF ground. The inner electrodes electrical connection is connected using a compression clamp that is precisely aligned to the back of the inner electrode. The mounting structure of the trap electrodes can be seen in figure 4.7.

Temperature of ions' surroundings plays a key role in understanding the black body radiation shift. The ion's biggest surfaces that it is exposed to are from the trap electrodes. For this reason two thermistors are placed on the support columns and one on the body to gauge the temperature of the electrodes and system in real time.

For operation the trap is designed to use the inner electrode as the RF drive electrode with the outer electrode as RF ground.

4.2.2.2 Micromotion compensation electrodes

Micromotion is a driven motion due to the oscillating trap field. Intrinsic micro motion is a fundamental property of an rf trap but excess micromotion is caused by unwanted fields pushing the ion out of the trap center. Stray charges can get deposited during ion loading causing excess micro motion. Excess micromotion can be seen as a broadening of the ions spectrum along the intersection axis of the stray charge. Fields can be used to compensate these stray charges and eliminate the access micromotion caused.

In this trap design two axis of the micromotion compensation electrodes is done by using two PCB based electrodes the other axis uses the outer electrode of the trap electrodes

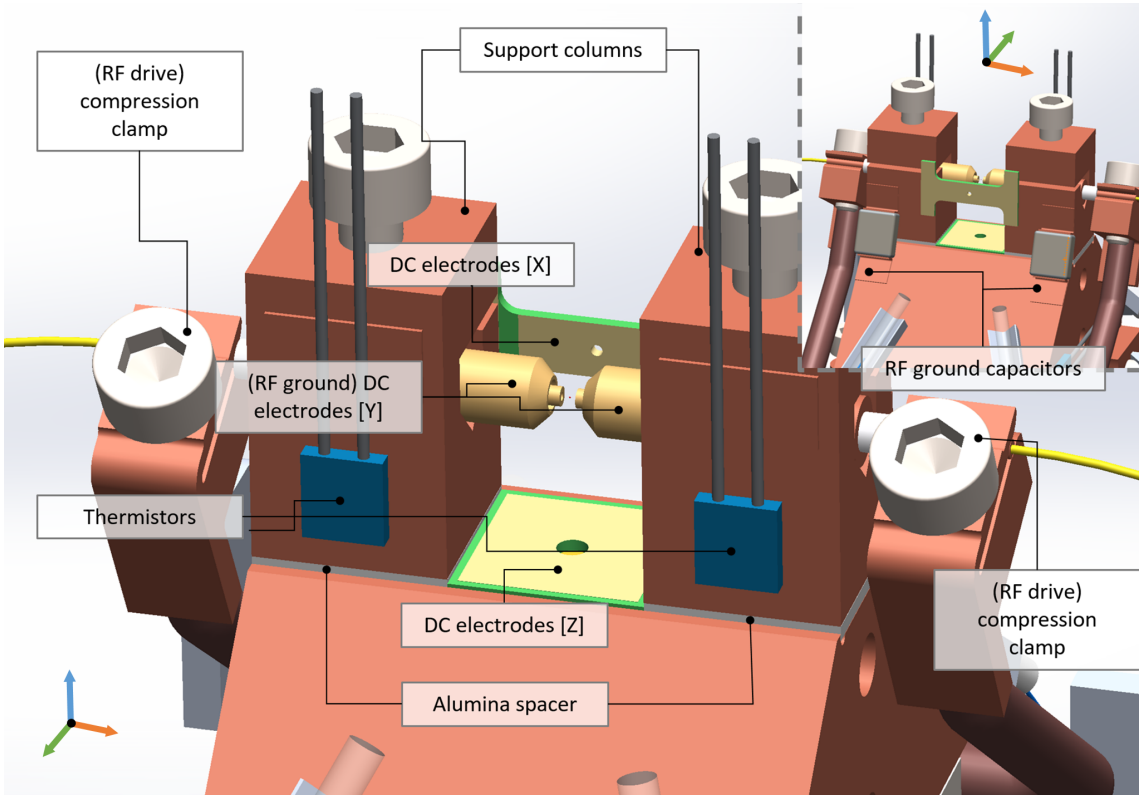

Figure 4.5: This shows the trap electrode structure and the micromotion compensation electrodes. Original SolidWorks drawing created by Dr Gonzalvo.

(see figure 4.7). This is done by having a connection attached directly to the mounting columns. The support columns are insulated at the base by an alumina spacer and connected to the rf grounded body by two capacitors. This allows the columns to be driven as well as rf ground.

4.2.2.3 Atomic oven

The atomic oven acts as the source of the atoms that go on to be ionised and then trapped. This is done using a resistive heater and sublimating calcium into a cloud which is collimated into an atomic beam that intersects the trap center. The restive heater is made up of a tantalum tube which contains calcium, wrapped in a tantalum wire. The wire is electrically connected to a high current source. Tantalum was chosen due its high resistance and high melting point.

The oven needs supporting as its alignment is critical. The oven is part of an assembly (see figure 4.6) that when inserted into the body self-aligns the exit of the oven with the collimators. The assembly consists of two notched alumina spacers epoxied into a titanium frame. The alumina spacers where chosen to thermally and electrically insulate the oven

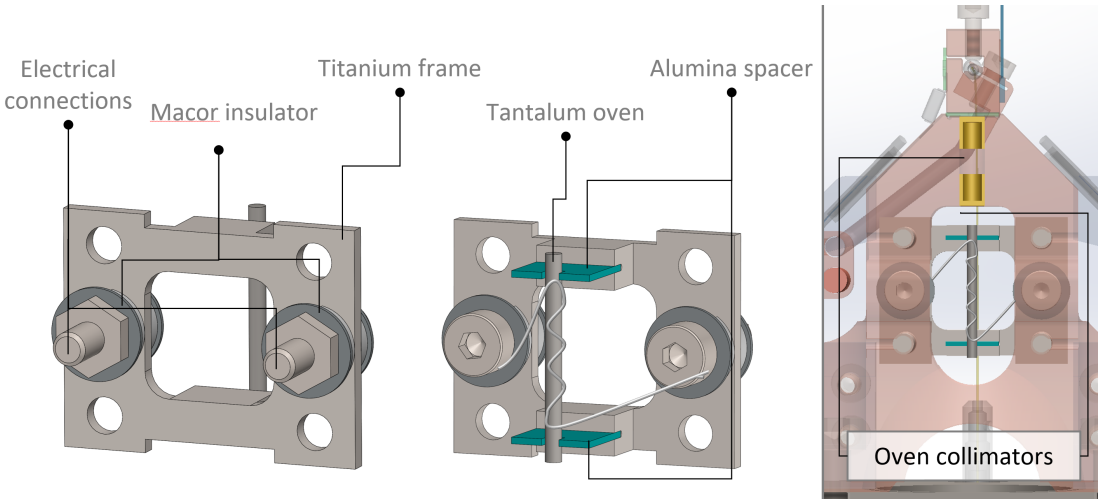

Figure 4.6: This shows the oven assembly and the way it is mounted into the trap. Original SolidWorks drawing created by Dr Gonzalvo.

from the trap. The oven rests on the two notches in the spacers and is held in place via tension of the tantalum wire.

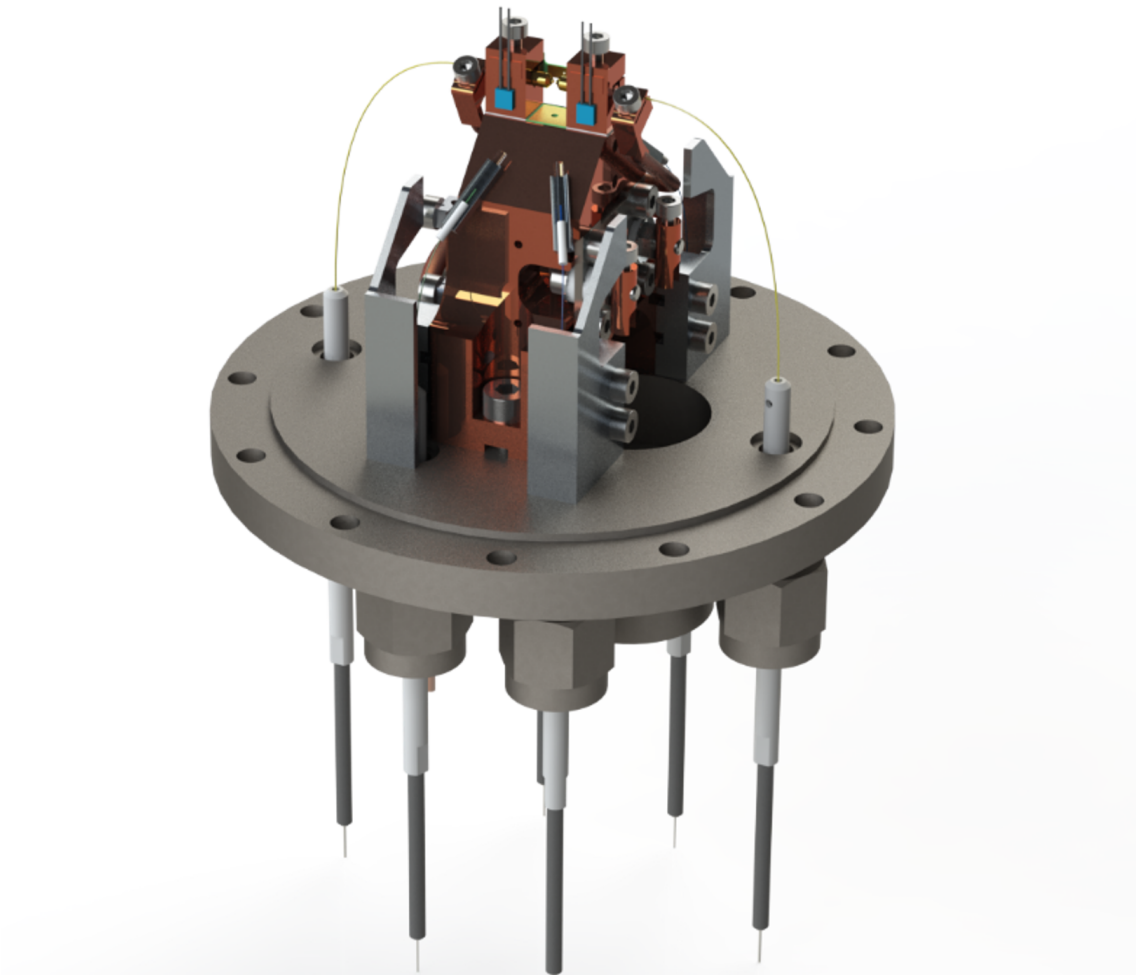

Figure 4.7: This shows the trap design. Original SolidWorks drawing created by Dr Gonzalvo.

4.2.3 Vacuum system

The trap must be in ultra high vacuum to reduce collisional interaction and maintain a highly isolated environment for the ion. This is done by encasing the trap structure in a sealed chamber that is pumped down to $< 10^{-10}$ mBar. The vacuum system must allow for all of the electrical connections and all needed fibers to pass between atmosphere and vacuum.

The trap is mounted on top of a custom flange. On this flange all of the traps connections are feed-through to atmosphere.

4.2.3.1 Fiber feedthroughs

Commercially available fiber feedthroughs rely commonly on two techniques. Epoxy potting and brazed metal sealing. Both of these methods do not fill the requirements needed for our feedthroughs. Brazed metal sealing requires metal coated fibers. These are not available for all the necessary fibers needed for this project or require post processing of fibers incurring additional complications. Epoxy potting, although is readily available and uncomplicated, suffers from out-gassing and poor diffusion rates making them unreliable seals. This lack of commercial availability for what is required by this system led to this in-house development.

The key design goals for this where:

1. Total leak rate $< 10^{-11}$ mbar l s^{-1}
2. Compact form factor
3. Adjustable fiber position
4. Vibration insensitive/ robust
5. Does not change fiber properties

The feedthrough we developed allows for a low diffusion seal in a small form factor with an adjustable positioning. It is based on two well known vacuum sealing techniques used in electrical and liquid/gas feedthroughs. Metal-metal compression seals are proven UHV sealing technique with a wide range of designs. Swagelok fittings compress 2 metal ferrules, which thread over a metal input tube/rod between a nut and the tapered swagelock body. When the nut is tightened it creates a metal-metal seal between the tube the ferrule and the body of the swagelock fitting. The seal between the fiber and the swagelok fitting uses a glass sealing process used in some experimental fixed fiber feedthroughs and electrical multipin feedthroughs. Glass sealing is accomplished by using low melting point solder glass preform to bond between surfaces. These benefit from low diffusion rates and high operational temperatures, but do suffer from some level of fragility.

Our design combines the solder glass bonding an arbitrary fiber to a stainless steel metal tube which is inserted into a swagelok fitting and sealed via the standard swagelok sealing method. The combination of these two techniques allows for an adjustable low diffusion rate vacuum seal, capable of delivering any needed fiber into the vacuum chamber at a small volume. A detailed schematic of the design can be seen in figure 4.8.

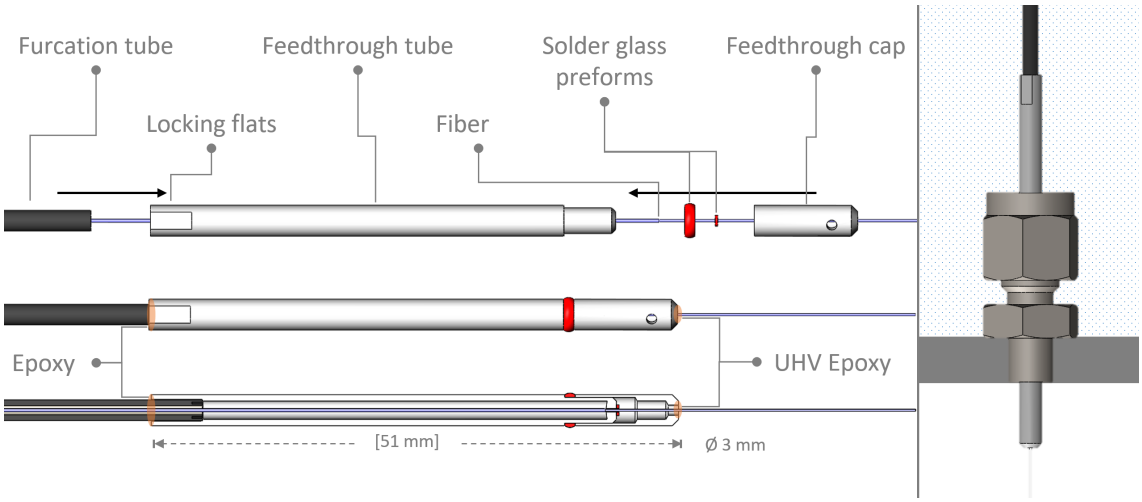

Figure 4.8: This shows a breakdown of the fiber feedthrough structure: an expanded view, the completed assembly, and a cut through once assembled. On the right is shown a completed feed through fastened into a swagelok fitting.

4.2.3.2 Electrical feedthroughs

The electrical feedthroughs requirements are commercially available. The trap requires dc and rf electrical connections to be fed into the trap. This is done using a high density multipin electrical feedthrough for the dc and a high voltage feedthrough for the rf. Both of these are electron beam welded into the flange.

4.2.3.3 The chamber and pumping system

The trap flange is sealed to the vacuum can using a gold wire seal on which the pumping system is situated. The pumping system, due to the required volume of the trap being so compact, can be achieved with low pump rate pumps. These pumps befit from requiring less power and are more compact. The pumping system (see figure 4.9) is connected using standard DN16CF flanges. It consists of an ion pump, a non evaporative getter (NEG), and a copper pinch-off tube. This system requires an initial pump down using a standard pumping system (turbo pumping backed by a roughing pump). Once pumped down, the copper tube is pinched and the two pumps will act to maintain the UHV required by the system.

The DN16CF flanges all use copper gaskets. The seal between the vacuum Can and the trap assembly flange is done using a gold wire seal.

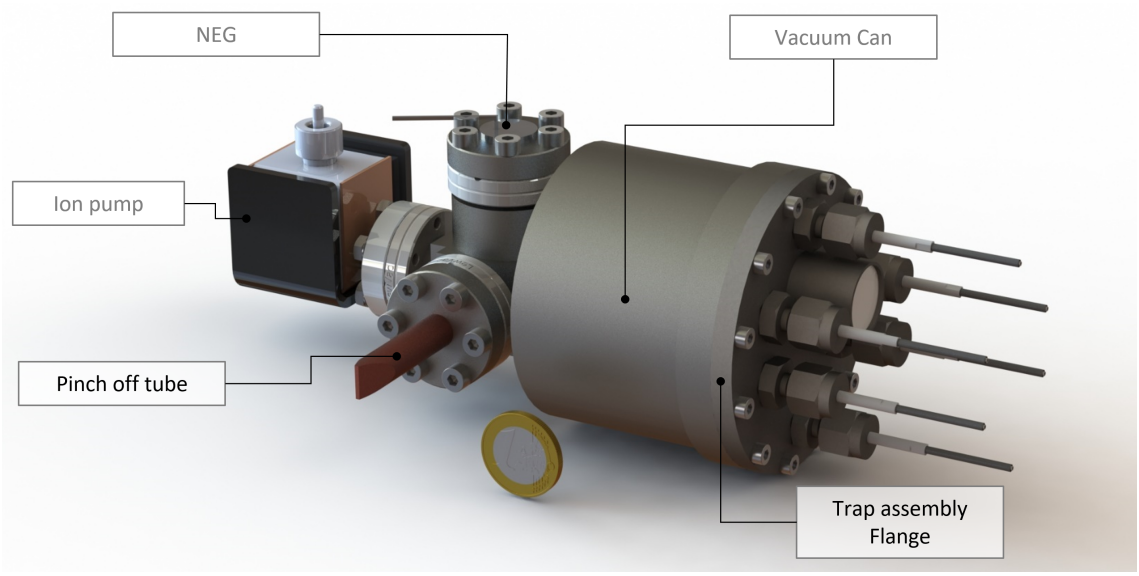

Figure 4.9: Portable trap design incorporating fiber optics for beam delivery and flores-cence collection. Original SolidWorks drawing created by Dr Gonzalvo.

4.3 Assembly

In this section the assembly of the trap is discussed. This is broken down into three sections. The beam delivery assembly, discussing how each of the beam delivery fibers was prepared, how the feedthrough was assembled and how the beam was characterised. The electrode assemblies, starting with the collection fiber tapering, followed by the feed-through assembly and then finishes with how the electrodes were prepared and assembled on the end of the fiber. The final section goes through the trap assembly, this highlighting the critical alignment steps and goes through in detail the methods used to assemble and characterise the trap.

During assembly there are cleaning steps. UHV washing and baking is referenced throughout this section. In the following the terms are described:

UVH wash: Using an ultrasonic bath the object is washed in each solution for nine minutes and then transferred to the next. The order in which each solution is used is as follows: Soap and deionised water, deionised water, deionised water, iso-propanol. After the wash the object is dried using dry nitrogen. This acts to wash off any oils and grease on the object and makes it ready for UHV.

Baking: The UHV cleaned object is placed into the baking chamber. This consists of a roughing pump backing, a turbo pump, that pumps down a large chamber to $10^{-6} - 10^{-7}$ mbar. The chamber is wrapped in two heat belts. The temperature is controlled by a variac and two temperature sensors placed along the chamber to measure the temperature.

Unless stated otherwise the bake is set to 250°C over two days. This acts to boil off any oils still remaining on the system after cleaning. This is useful to do in our system as the low baking point caused by the combination of GRIN lenses and epoxies means a thorough pre-bake is necessary for a timely bake when assembled.

Another process used throughout when dealing with epoxies is degassing:

Degassing: Our lab built degassing chamber backed by a roughing pump is used. The epoxy is placed in an open boat into the vacuum chamber and sealed. This is pumped down, and over a period of five to ten minutes is shocked back to atmospheric pressure and re pumped down several times. This encourages any trapped gas during mixing of the epoxy out. This is a necessary step as any gas trapped in epoxy when cured can create local pockets of high pressure leading to virtual leaks.

4.3.1 Beam delivery assemblies

The beam delivery assemblies are built from the delivery fiber up. All four of the delivery fibers are built using the same method. The difference is in the used fibers and lenses based on the frequency's required. The beam delivery assemblies start with preparing the fiber by securing the ferrule and polishing, next the feedthrough is built around the fiber, then the lens assembled, and finished by charactering the beam profile. These steps are discussed in detail below highlighting the procedures used.

4.3.1.1 Beam delivery fibers

The beam delivery fibers are mounted into ceramic ferrules used to align the beam to the center access of the GRIN lens. The fibers require epoxying in place within the ferrule and then polishing to ensure a clean optical emission. All of these components are mounted inside the UHV environment and therefore have to be UHV cleaned and baked before construction.

The epoxy used to secure the fibers in the ferrules was EPO-TEK® 353ND. It can be cured at 150°C in one minute. This epoxy is low viscosity, UHV compatible, and polishable using standard fiber polishing techniques. Once the epoxy is mixed it must be degassing.

There are three types of polarisation maintaining single mode optical fiber used [2x PM-S405-XP, PM630-HP, PM780-HP].

The fibers are first stripped of their coating ≈ 10 cm and wiped down with an optics tissue and iso-propanol. A custom heating block (UHV cleaned) clamps 8 ferrules in a

stainless steel disk. The fibers are inserted with a small amount of degassed EPO-TEK® 353ND into the clamped ferrules, a further small application of the epoxy at the end of the ferrule is achieved with a cleaned fiber. The fibers are secured at fixed distance of 35 mm to their coating shoulder. The stainless steel block fits inside a small induction heater coil[2] and acts as a heating element used to cure the epoxy. The system is pre-calibrated with a temperature probe coupled to the heating block at 150°C. Induction heating allows a controlled heating profile that is repeatable.

The excess fiber protruding out of the ferrules was cut using a diamond scribe. Polishing the fibers was done using a SpecPro™ Connector Polisher by KrellTech. This polisher allowed the ferrules to be clamped and polished using a series of finner lapping papers and pressure to ensure a clear ferrule surface. The polish is characterised by imaging the surface of the ferrule using a fiber inspection microscope rigged on a 3D micro stage. Once the polish quality was verified, the fiber was stored in a sealed container ready for feedthrough assembly.

4.3.1.2 Fiber feedthrough assembly

The feedthrough assembly is broken down into three steps: solder glass sealing, fiber support, furcation tube sealing. The solder glass sealing utilises preforms from OZ optics [GSP-C-381-1054-254] which melt at 400 degrees. An induction heater is used to achieve this[3].

Eight fiber feedthroughs are constructed on the mounting 'skewer'. The skewer consists of three individual clamps clamping the feedthrough tube, fiber, and protective furcation tube. These clamps are mounted on a rod and spaced to aid assembly. The clamp for the feedthrough tube also doubles as a heat source for melting the solder glass preforms and curing the EPO-TEK® 301-2.

The feedthrough tube and the feedthrough cap are UHV washed and baked. The needed fibers are wiped down using iso-porpanol and optics tissues. The solder glass preforms are UHV washed. The EPO-TEK® 301-2 is degassed before application. All tools used were UHV washed.

The assemblies start with each feedthrough tube being mounted to the skewer. The fibers are inserted back to front. This means that all the parts in between the fiber and the feedthrough tube are inserted onto the fiber, before the fiber is inserted into the feedthrough tube. Once assembled, the skewer is rotated so that the vacuum end

[2] 1000W 20a ZVS Low Voltage Induction Heating Board with copper induction coil

[3] 1800w 40a ZVS Induction Heating Board with copper induction coil

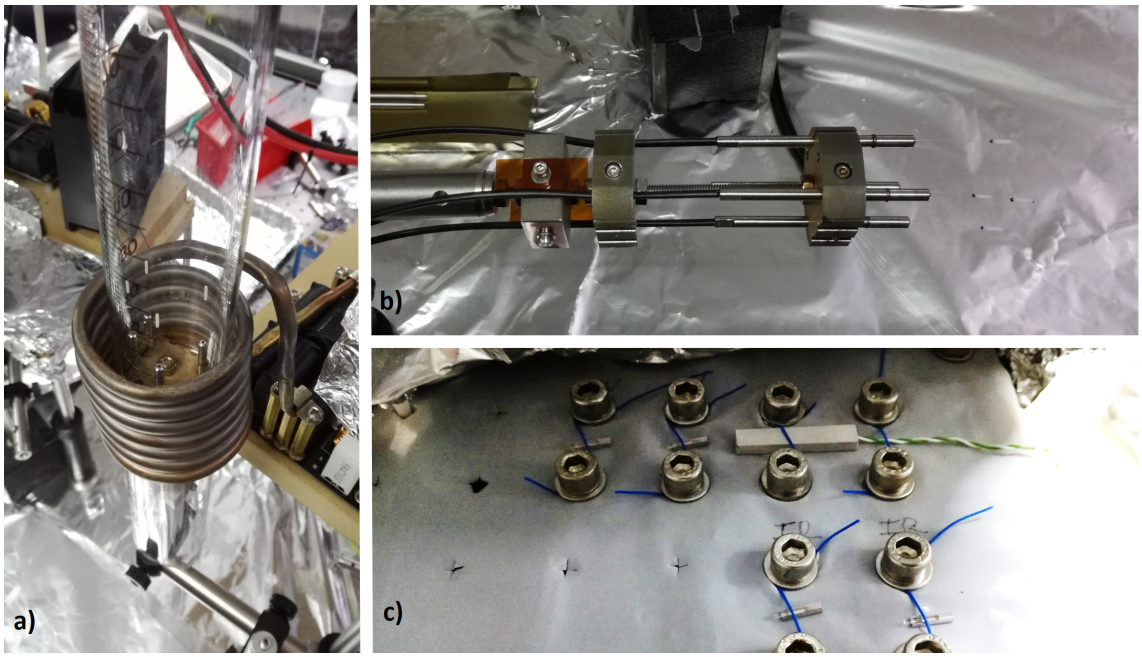

Figure 4.10: a) The feedthrough assembly inserted into the induction heater protected by the measuring cylinder. b) The "Skewer" with four complete beam delivery assemblies. c) Epoxying the GRIN-lenses into the V-grooves mounted to the heat plate.

of the feedthrough tubes are pointing down. This aids the solder glass preforms to melt flush to the feedthrough tube surface. An inspection is made to ensure the solder glass preforms are resting on top of the feedthrough tube front face and that the feedthrough caps preforms and caps are resting correctly. The skewer is mounted inside the induction heater with the coil around the feedthrough clamp. An upside down measuring cylinder is placed between the induction coil and the skewer. This acts to shield the feedthroughs during cooling down from much colder air currents in the laboratory which makes the fiber seals brittle. The induction heater uses a pre-calibrated heating profile to melt the solder glass preforms and reduce thermal shock. The measuring cylinder is removed after melting of the preforms. A small application of degassed EPO-TEK® 301-2 is applied to the feedthrough cap head. This beads between the fiber and the cap supporting the fiber. EPO-TEK® 301-2 is a low viscosity, UHV compatible epoxy cured at 80°C for three hours. A curing profile is used with the induction heater. The furcation tube is slid over coated fiber. Before inserting into the feedthrough tube a small application of general purpose epoxy [G14250 by ThorLabs] secures the furcation tube in place. Once fabricated each feedthrough assembly was stored in a cleaned sealed container.

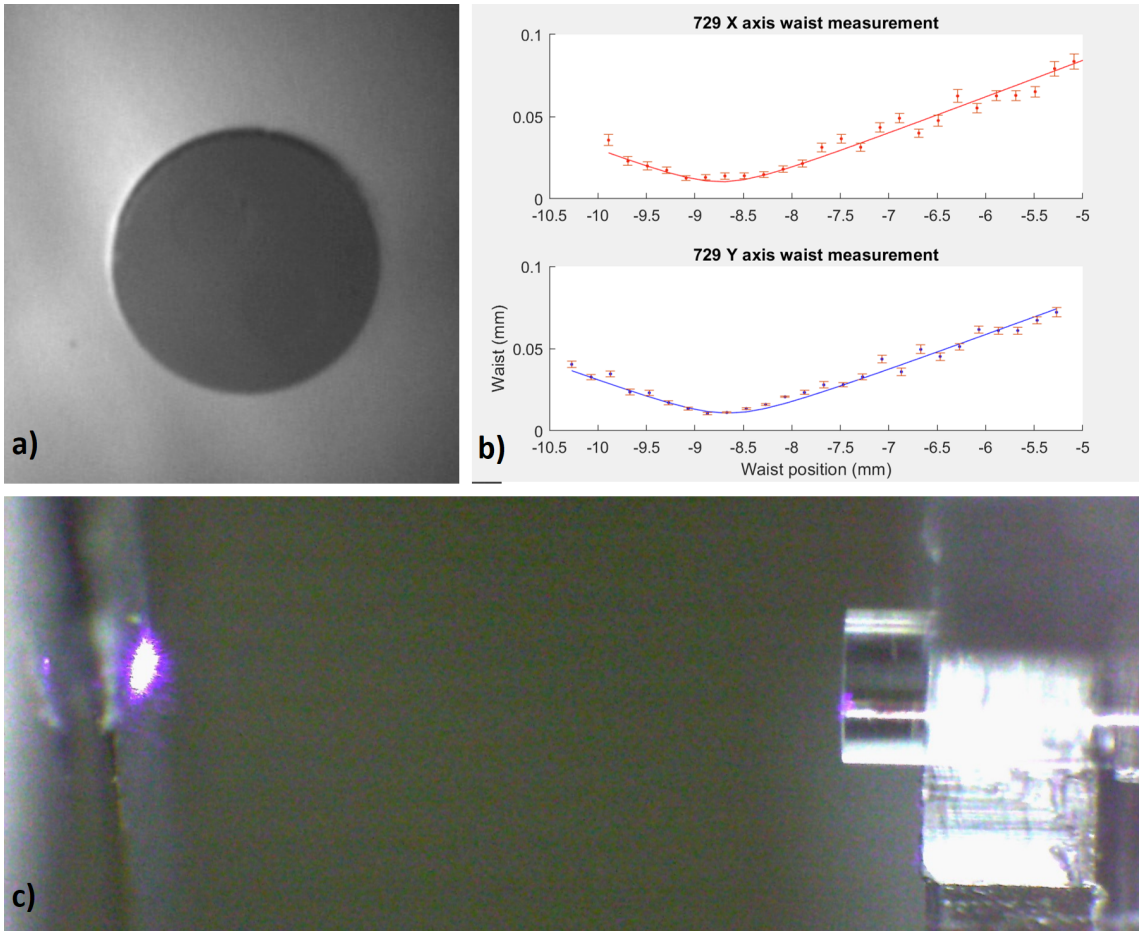

Figure 4.11: a) Polished ferrule surface. b) Example knife edge measurement of both axis of a 729 beam profile. c) Beam scattering of the knife blade used for calibrating.

4.3.1.3 Lensing and beam characterisation

Each of the beam delivery feedthroughs are tested prior to GRIN lens assembly. The input side of each beam delivery feedthrough is cleaved using Fujiura CT-101 at a tension of 180 gF (gram force) and mounted inside a thorlabs bare optic terminator[BFT1 + B30125D1]. Light of the intended wavelength is fiber-fiber coupled to the feedthrough. The free space propagation is visually inspected, using a beam detector card[4] over a length of a 10 cm. Any observed defects in the Gaussian profile would result in the feedthrough being dismissed.

The V-grooves are UHV washed and baked. The lenses are considered vacuum ready due to the fabrication and storage. The EPO-TEK® 301-2 is degassed before application. The mounting plate was wiped down with acetone and optical wipes. The tools used were UHV washed.

The GRIN lens and the V groove are assembled before the ferrules are introduced. This reduces complexity in clamping the three pieces. Each lens is placed on the V-groove and judged by eye to have an overhang of ≈ 1.5 mm. The position of the lens is uncritical with respect to the V-groove ± 0.5 mm. A small application of EPO-TEK® 301-2 is placed on the center boundaries of lens and V-groove. The use of EPO-TEK® 301-2 offers a low viscosity UHV compatible epoxy with a low curing temperature ($80°C$ for three hours) and $> 80°$ C glass transmission temperature. This means no unexpected misalignment should occur during the multiple curing runs at $80°$ C due to the glass transition. A mounting plate secures 16 lens assemblies ready to be cured. A hot plate, referenced to a temperature sensor and clamped to the assembly block, is used to cure the epoxy.

The GRIN lens assembly is mounted in a fixed clamp. This clamp is resistively heated using a calibrated high power resistor. A further feature of the clamp allows the securing of the beam delivery fiber ferrule once aligned. The fiber feedthrough is clamped using a V-groove mounted to a single axis linear translation stage[5]. This allows fine adjustment of ferrules position in the GRIN lens assembly V-groove to achieve the wanted nine mm focal length. To characterise the focal length a knife edge measurement is used. Two blades, mounted perpendicular to each other, are mounted to a three axis stepper motor controlled linear translation stage [MAX381/M ThorLabs]. The blades are positioned just after the lens. Light of the used frequency of each assembly is coupled to the input side of the feedthrough. A power meter [PM100D with S120C by ThorLabs] is used to

[4]For the visible beams a piece of white card was used for the inferred beams a thorlabs VRC5 card was used

[5]MT1/M by ThorLabs

measure the transmission power of the lensed setup. The blade position is calibrated to the front surface of the GRIN lens referenced to the width of the lens. Both axes are measured against the transition axis. This allows a further check to see if there is any stigmatism in the lens. Once the ferrule is set to the right position to produce the nine millimetres focal length, it is clamped and a small application of degassed EPO-TEK® H21D is applied to the back of the assembly. This epoxy is used due to its high viscosity and UHV compatibility it can be cured at $80°C$ for 90 minuets. Previous assemblies used EPO-TEK® 301-2 but had issues with epoxy running between the lens and causing washed out emission profiles. The resistive heater cures the epoxy. A further run of the knife edge measurement is done to check the profile to ensure nothing has moved in curing. This is repeated for each beam delivery assembly.

4.3.2 Electrode assemblies

The electrode assemblies are built similar to the beam delivery assemblies, from the fiber upwards. The assemblies start with the preparation of the collection fiber, followed by the assembly of the feedthrough and finishing with the electrode assembly on the input of the collection fiber. These steps and the fabrication methods are discussed in detail in this section.

4.3.2.1 Collection fibers

The collection fibers have an outer cladding diameter of 220 μm. Due to the inner electrode's inner diameter which is also 220 μm and having a tolerance of five percent, the fiber was too big to be cleanly inserted into the electrode. No commercially available fibers were found to fit the needed specification. The solution was to reduce the outer diameter of the fiber by 20 μm via tapering.

Fiber tapering was achieved using the ARCMaster® FSM-100P+ by Fujikura and the control software supplied (FPS[6]). This allowed for the diameter and length of the tapper to be defined. The tapper length was set to one millimetre with a linear tapper profile and a 15 mm constant draw followed by a symmetric re-tapper. 15 mm gave enough tolerance so that after the cleave and the 11 mm insertion length into the electrode, the fiber would be able to protrude out of the electrode. This would allow for surface quality checks before being retracted into the electrode for final positioning. Before tapering, the splicers motors were alignment calibrated and the arc power was calibrated and linked

[6]Fiber Processing Software version 1.7

to the tapper profile. This ensured a repeatable tapper every time. After each tapper, a tapper profile was recorded using the FPS software to ensure the profile matched that of the expected.

The FG200UEA fiber from thorlabs had its coating stripped to a length of $\approx$ 10 cm and was then wiped down with an optics tissue and propanol. Using the FH-100-250-EV clamps, a reference marker was used to ensure the fiber was placed with the coating shoulder (inface between coating and stripped section) in the same position in the clamp every time. This allowed for ease of cleaving. Once the tapper was performed and characterised, the fiber was removed from the ARCMaster® within the reference clamp. The cleaver used was the CT-101 by Fujikura, this benefited from using the same mounting method used in the ARCMaster® using the FH-100-250-EV clamps. This allowed the cleavers cleave distance to be fixed and then each fiber could be cleaved at the same point referenced to the clamp. This made processing the 17 fibers repeatable and more time effective. The cleave tension used to achieve a clean cleave was found to be 500 gF.

The final test was to check the cleave quality. This was done using a microscope setup, consisting of a 10x Nikon objective, a Moticam 5 camera by Motic. Once cleaved, the quality was verified and the fiber was stored ready for feed-through assembly.

4.3.2.2 Fiber feedthrough assembly

The fiber feedthrough assembly was done in the same way as the beam delivery fibers. For details please see 4.3.1.2.

4.3.2.3 Electrode assembly

The electrodes are machined in house to the dimensions given in the design. Both the inner and outer electrodes require polishing and gold coating from their machined state. The front surface of the electrodes are critical, as these are the surfaces the ion is exposed to. Any surface roughness causes imperfections in the trapping profile. The electrodes are handled in transfer or mounting at the back to avoid damaging the critical surface.

To polish the electrodes, each electrode is spun on a watch makers lathe and polished, using three stages of polish paper [5 μm, 3 μm, 0.3 μm]. The surface is visually inspected and recorded with a high magnification USB camera looking for a mirror finish. Once polished the inner electrodes are cleared out using a piece of stripped 200 μm fiber inserted back to front. This ensures that they are clear of any obstructions without posing risk to

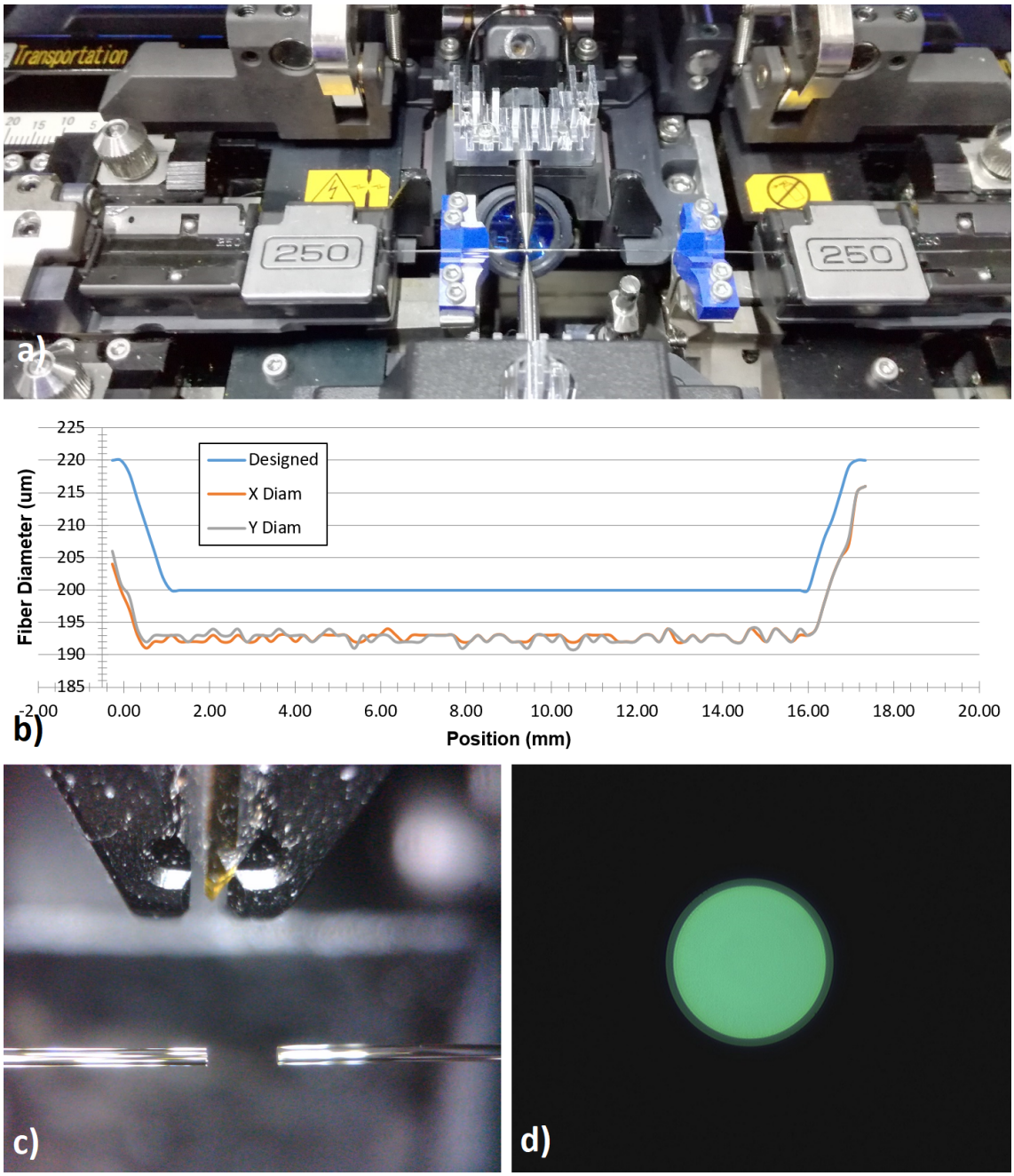

Figure 4.12: a) The image shows the ARCMaster® FSM-100P+ by Fujikura after tapering. b) The measurement of the tapper profile. The actual deviates from the intended, but this seems to be an error in the read, as the program suggested the diameter of the fiber was 205 μm which it was not. The offset would imply the tapper achieved tapper width of 207 μm. c) This image shows the cleave position of the used fiber on the left and the retapper can be seen on the right. d) The cleaved surface of tapered fiber

the polished surface. Next, the electrodes undergo a UHV cleaning process and are baked.

Gold coating and electrode assembly is done back to back in order to reduce any chance of contamination occurring. Any contamination in the electrode assembly, resulting in localised outgassing, has a high risk of flowing along the electrode axis. This would result in a high collisional rate at the trap center resulting in an unstable trap environment. This would be very hard to detect, as a small leak would result in only a very small rise in background pressure, but locally for the ion the pressure could be high.

For gold electroplating, the copper electrode surface must be free of any oxide layer. To do this, each electrode is ultrasonic washed in HCL (3.5% concentration) < 30 s. The inner electrode is pipe cleaned whilst submerged using a stripper 200 μm fiber. This is followed by a wash in deionised water for two minutes in the ultrasonic bath. During washing the electrode is pipe cleaned to ensure cleaned throughout. This is followed by a two minute wash in iso-propanol and dried with dry nitrogen. The gold plating method we used was based on tank plating setup by SPA plating. This consisted of a gold coating solution [HS Code: 3824 99 70] in a 250 ml beaker and a platinum anode with the intended coating electrode connected as the cathode. The circuit was completed with a mA adjustable power supply. The current and time of deposition was calculated using SPA plating deposition calculator for a one micrometer gold layer: inner electrode [3 mA, 2.3 V, 8 min 41 s], outer electrode [11 mA, 2.8 V, 8 min 41 s]. When coating, it was found that putting the solution in the ultrasonic bath gave the best surface quality results, as it dislodged any bubbles formed on the electrode. After coating, using the same clamp used for coating, the electrodes were washed in deionised water, followed by a wash in iso-propanol and dried using dry nitrogen.

The electrode assemblies were built onto the collection fibers. A combination of clamps, translation stages, cameras and an electrical heat gun were used in this assembly. Each clamp in direct contact with the electrodes or vacuum intended component was UVH washed. The alumina spacers were UVH washed and baked.

The inner electrode is carefully reverse inserted into a V-groove mount with a cleaned piece of viton rubber acting as a soft clamp. This mount is on a three axis linear translation stage. The collection fiber feedthrough is mounted via another V-groove on a seperate three axis linear translation stage. On this stage two USB high magnification cameras [Zhangwei-10765-ZZWBOX] are mounted perpendicular to each other. These are aligned in a way that their viewing axis is perpendicular to the fiber axis. These cameras can be translated along the fiber axis using another translation stage. This free movement

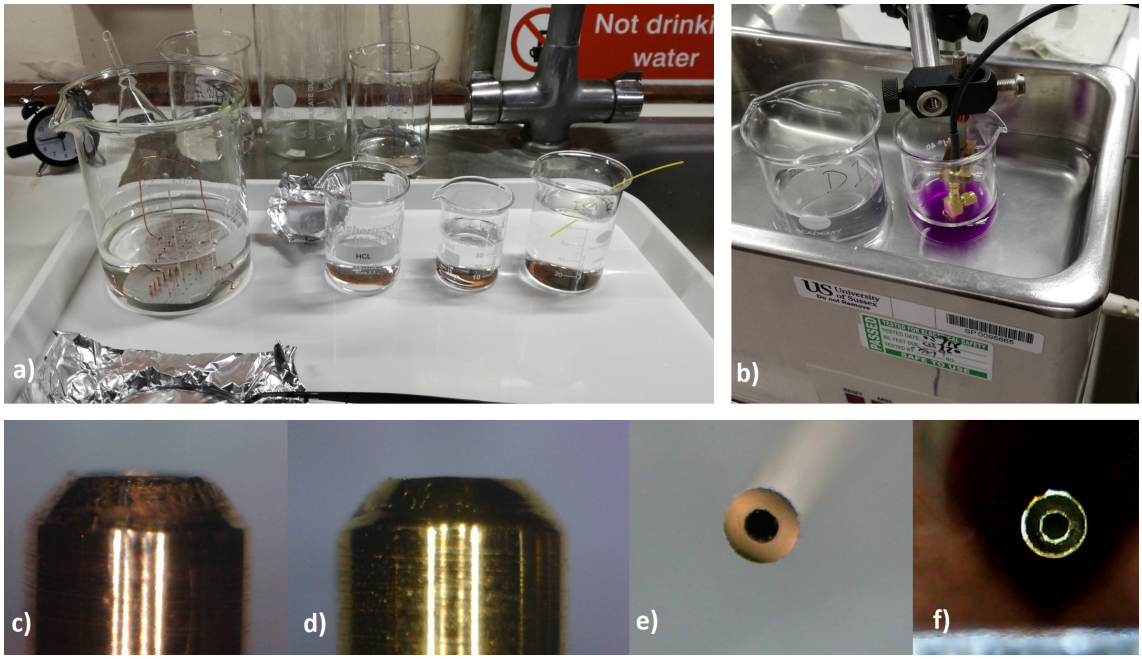

Figure 4.13: a)This photo shows the chemical setup, in the largest beaker the polished electrodes can be seen. b) Here the gold coating setup is shown. The purple liquid is the gold coating solution. The electrode is mounted on a modified SMC T-piece. c) This is the state after polishing the outer electrode. d) The outer electrode after gold coating is shown. e) This is the polished surface of the inner electrode and in f) after gold coating.

of the cameras along the fiber axis allows the front of the fiber to be viewed and easily translated to the rear tapper shoulder of the fiber when epoxying, without disturbing any of the setup. The collection fiber front face is aligned to the center of the electrode allowing a clean insertion. The fiber is translated to protrude out of the electrode. The fiber and the electrode face are inspected using a third USB high magnification camera mounted down the axis of the fiber. This is to ensure the fiber surface is clean and the electrode surface has not been caught during insertion[7]. The fiber is then aligned to the front surface of the electrode using the two side facing cameras. The fiber is recessed 50 μm inside the electrode using the scale on the translation stage. The two side facing cameras are translated to the back of the electrode, where a small application of degassed EPO-TEK® 301-2 is applied. To cure the epoxy an electric heat gun is used. A further K-type thermo-coupler was mounted to the side of the clamp, housing the electrode. The thermo-coupler protruded below the electrode in the line of sight of the heater. This gave a more accurate temperature measurement of the heat gun. The temperature on the heater was set to the lowest setting (100° C). At the separation distance, the thermo-coupler read measured $\approx 90°$ C. The cameras were retracted and the epoxy was cured over three hours. Once cured, the joint was reinspected using the two side facing cameras and the front face of the electrode was checked to ensure the epoxy hadn't ran over the front face of the collection fiber. The electrode was realised and the fiber feedthrough was retracted, removing the inner electrode from the clamp.

The same V-groove clamp used to house the inner electrode, had the viton rubber soft clamp removed and the gold coated ground electrode is now mounted rear end first. The alumina spacer is carefully inserted into the rear end of the ground electrode. This is a tight fit and does not require any clamping once inserted. Using the two side face cameras aligned to the inner electrode end, the inner electrode is aligned to the center of the alumina spacer. The front facing camera is focused on the front surface of the inner electrode to aid insertion through the alumina spacer. This is done slowly and correctively to ensure the inner electrode does not come in contact with the side of the spacer. The electrode is set to protrude 250 μm. This is judged by referencing the outer diameter of the electrode at 500 μm and using the pixel spacing to reference the protrusion. The three cameras and the three axis translation stage are used to concentrically align the front face of the inner electrode to that of the outer. The two side cameras are now retracted to the base of the alumina spacer. A small application of degassed EPO-TEK® 301-2 is applied to the seam

[7]In some insertions the fiber caught the edge of the electrode and pulled off a flake of the gold coating, due to higher deposition of gold on the edge of the electrode.

between the alumina and the inner electrode and the seam between the alumina and the outer electrode. The electric heat gun is used to cure the epoxy over three and half hours, during which the two side cameras are removed, but the end face camera remains. The electrode alignment is monitored intermittently over the cure duration, looking for any deviation due to asymmetric cure, which was corrected immediately if observed. Once the electrodes are cured the clamp is realised and the complete electrode structure is translated out of the V-groove holding the outer electrode. This is then stored in a cleaned purpose build container ready for use in the trap fabrication.

4.3.3 Trap assembly

Previous trap assemblies highlighted the importance for fully clamped translatable alignment of both the beam delivery and the electrodes. The assembly of small optics on a small frame with several mounting and curing procedures made it a complex assembly. For this reason, the trap assembly was modelled in solid works first. The assembly is made out of a combination of custom mounts and clamps, linear translation stages and a selection of high magnification cameras aligned in specific orientations. In this section a detailed break down of how the system is assembled and characterised is presented.

The trap assembly is built on a cleaned optical breadboard with a protective perspex cage surrounding it. Each face of the perspex cage can be removed when access is needed. The cage prevents contamination during dead periods in assembly and protects the system when working around the trap. The breadboard has an access hole under the position the trap is built, to allow for fibers and the electrical connections to be accessed without contaminating the chamber.

All the mounts, used that did not have direct contact with anything in UHV, were wiped down using iso-propanol. All mounts, that had direct contact with any intended UHV component, were UVH washed and baked. All tools were UHV washed and stored. When assembling the trap, a mask and gloves were worn throughout the assembly. All of these precautions and pre-cleaning were taken to ensure the system, even if being baked at a low temperature $< 80^{\circ}$ C, achieved the desired pressure.

The assembly requires several heating periods for curing epoxies on the trap. This requires the system to be heated to a well controlled temperature to ensure no damage is caused by overheating key components like the GRIN lenses. A resistive heater is mounted in place of the oven. The mount consists of a high current resistor, mounted to a copper block. This is used in parallel with mounted thermistors, initially on the trap, and later

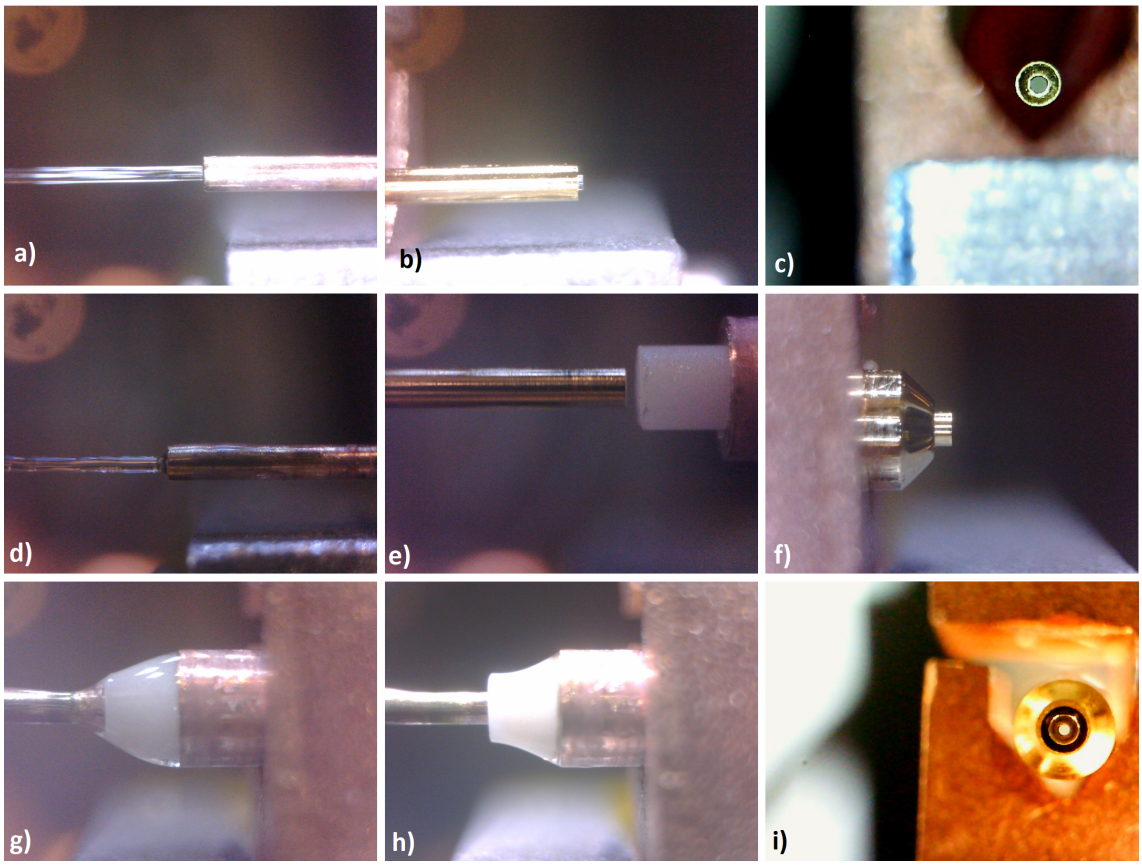

Figure 4.14: a)Shows the alignment of the collection fiber into the inner electrode. b) and c) show the protrusion and surface check of the collection fiber after insertion. In d) the cured EPO-TEK® 301-2, securing the fiber into the electrode is pictured. e) The alignment of the inner electrode to the center of the alumina spacer inserted into the outer electrode. f) Inner electrode protrusion distance set. g) and h) show the state before and after curing the EPO-TEK® 301-2, securing the inner electrode to the space and outer electrode. The epoxy can be seen to have run into the assembly. i) Here is pictured the finished end surface check of the electrode, ensuring no epoxy overrun.

in the build on the electrodes, to finely control the temperature.

4.3.3.1 Flange and trap base

The electrical multipin connector had each pin UHV soldered to a kapton coated wire. This wire was used for all the electrical connections, except the oven, which uses two wires per connection and a thicker gauge kapton coated wire. The oven wire was soldered to two pins per connection, to ensure the feedthrough pins current was not exceeded. The three PT100 thermistors and the four dc electrodes were UHV soldered to the wires. Each PT100 is configured in a four wire connection to ensure the highest accuracy measurable. Soldering each component to the electrical feedthrough was found to be a much easier and safer solution, than electrically connecting once attached to the trap.

The trap is built on top of the feedthrough flange. Access is needed underneath the flange, therefore it is raised on a pedestal. The electrical multipin connector needs to be inserted first as the base sits on top of it. It is secured using a locking screw. The trap base is mounted and the electrical connections are cable managed to the base. Then the two oven collimators are inserted and clamped.

The top camera [Zhangwei-10765-ZZWBOX] is critical to the alignment of the electrodes. The electrodes need to be referenced to the oven axis. To establish this axis, the camera is aligned by translating the focal plain between the top oven collimation hole and the bottom one. Any angular mismatch between the camera axis and the collimation axis can be seen as a difference in position of the collimation hole. Once corrected the camera is fixed.

The top camera is needed for the alignment of the central DC compensation electrode, to ensure its hole clears the collimation holes. The two alumina insulation pads, a PT100 thermistor mounted to the base, and the aligned DC compensation electrode are epoxied to the base. Degassed EPO-TEK® 301-2 is used and all components are held in place using spring loaded pressure clamps.

4.3.3.2 Electrode alignment

The electrodes are mounted at 90° to the fiber feedthroughs. Due to the risk of fiber breakage the 90° angle was established before the fiber feedthroughs where inserted. To do this each electrode was delicately mounted into a 90° clamp. This consisted of four clamps and a support wire. This mount allowed for protected insertion of the electrode assembly with easy attachment to the three axis translation stage. This mount can be

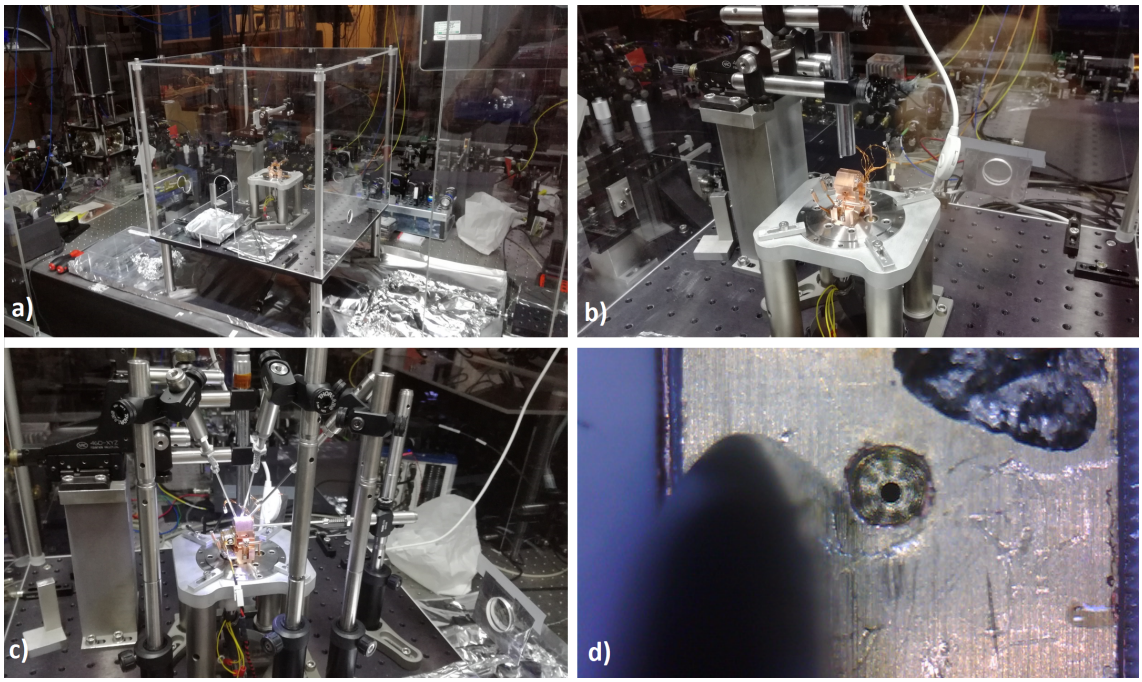

Figure 4.15: a)Here the protective cage surrounding the assembly is shown. b) The alignment of the top camera to the collimation axis can be seen c) The curing of the EPO-TEK® 301-2 using the resistive heater and the spring loaded pressure clamps are pictured. d) This shows the top view of the bottom dc electrode ensuring the collimator (centered) is not covered.

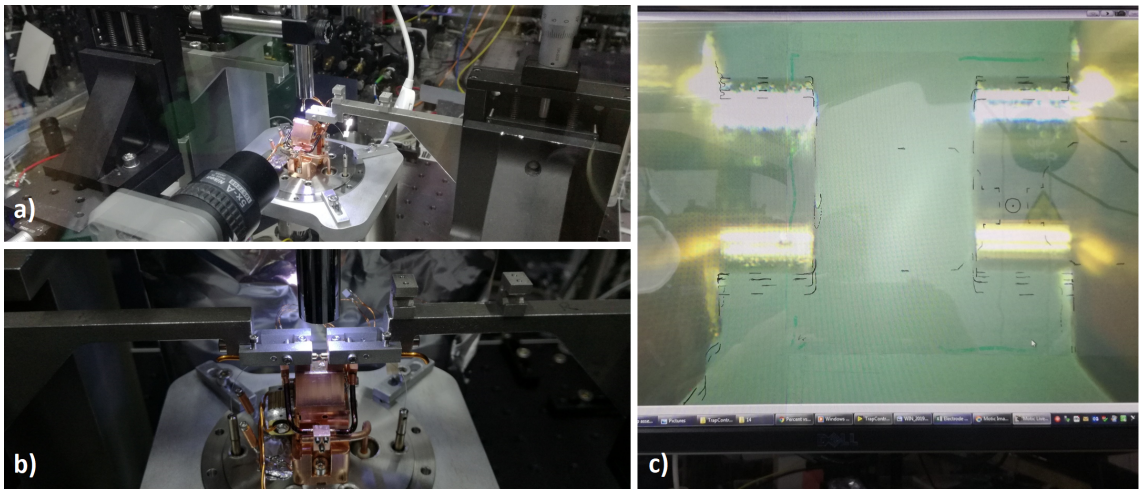

Figure 4.16: a)This shows the first electrode mounted to the translation stage. b) Both electrodes mounted and aligned are shown c) This pictures the marked edges of the electrode were used on a clear plastic sheet for alignment checking. The difference between before curing and whilst at 80° C can be seen by the lower markings and the current position of the electrode.

seen in figure 4.16.

The assemblies had to be inserted into the fiber feedthrough clamps, back to front. The furcation tube was cleaned prior to insertion. Once inserted, the assembly rests on the V-groove attached to the fiber feedthrough. A clamp on a single axis translation stage is used to attach the fiber feedthough on the atmosphere side. With the fiber feedthrough supported on the atmosphere side and the electrode supported by the three axis translation stage, the supporting wire is cut and removed along with the V-groove clamped on vacuum side attached to the fiber feedthrough. The electrode is now coarsely aligned and the feedthrough can be translated higher, if any tension is seen in the fiber or if any bowing of the fiber is seen due to too much slack. The feedthrough is now clamped. On each feedthrough tube there is a key at the furcation intersection, using a homemade tool, which is held in place while the swagelok is tightened. Without the use of this, we saw the swagelok could rotate by 90°, causing unwanted strain on the fiber. The clamp holding the feedthrough tube is now removed. This process is repeated for the other electrode assembly.

A microscope using five times objective is used to view the axis flat onto the electrodes.

The electrodes are aligned centrally between the oven collimator via the top camera. The electrodes are aligned to 200 μm from the oven collimation center. The front facing camera gives a further reference on electrode separation as well as giving a reference on

electrode height alignment. Once aligned a small application of degassed EPO-TEK® 301-2 is placed. To do this, each electrode is translated off the base and the epoxy is applied on the insulation pad, then the electrode is brought back into alignment. The ability to float each electrode ensures symmetric aliment reducing the error in the trap center prediction. The pads were cured using the resistive heater. During the cure the electrodes were readjusted. This was caused by some asymmetry in the insulation pads. This meant when the base was heated to 80°C one pad had more epoxy in-between compressing the epoxy. When the base was at temperature the electrodes were brought back to alignment and cured. Once cured and once the base was back at room temperature, the electrodes aliment was recorded.

The clamps holding the now epoxied V-grooves were removed, the translation stages for both electrodes were removed and the MM fiber shields were installed. These were temporarily placed to protect the bare MM fiber during further assembly.

The grounding capacitors are mounted using degassed EPO-TEK® H21D. This is a conductive epoxy that is UHV compatible and it cures at 80°C. The capacitors were placed using tweezers and clamped using a spring loaded pressure clamp.

The rf electrodes electrical connections were delicately mounted. This was done using tweezers and once hooked onto the electrodes, secured with a clamping screw.

The rf feedthrough is checked against the electrode tip and ground. For this a probe wire on a translation stage was carefully aligned to make a connection between the back surface at the tip of the electrode. Another test, using an inductor and driving the rf feed through with a sinusoidal function generator, was done.

Once tested the two PT100 thermistors and the two dc connection pads where epoxied to the back sides of each of the electrode V-grooves. This was done using a small application of degassed EPO-TEK® 301-2 and clamped using the spring loaded pressure clamps. The resistive heater was used to cure.

4.3.3.3 Beam delivery alignment

The beam delivery system needs to align each laser to the position of the ion, when trapped. This requires the knowledge of the trapping position and the ability to align each beam to that. The endcap trap has a 3D parabolic trapping profile, making the symmetric center of the electrodes the trap center. By aligning the beams to the electrode center, they will be next aligned to the trap center and then to the ion. To do this a scattering plate is aligned to the center of the trap electrodes, allowing the beam to be

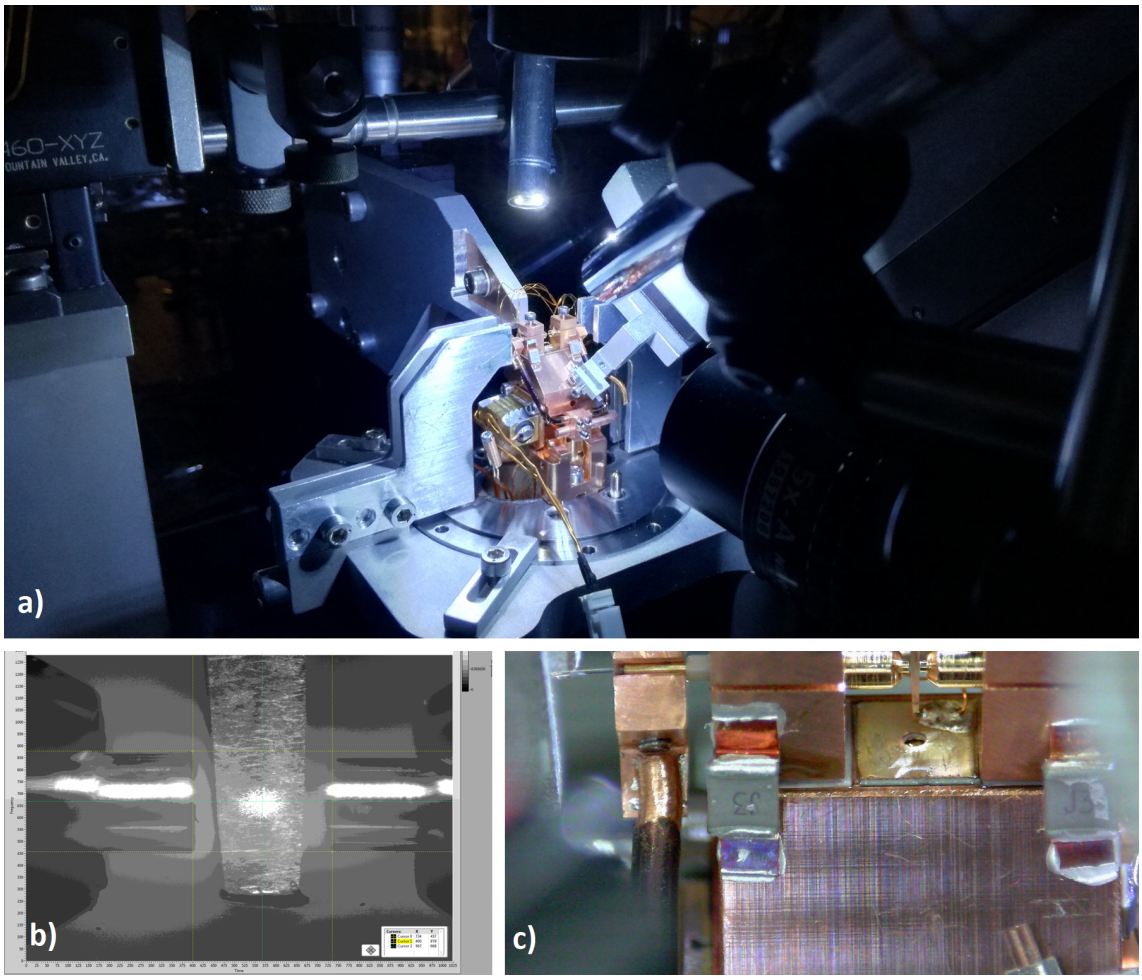

Figure 4.17: a)This shows the alignment of beam delivery fiber. b) The motic cameras view of the scattered light of the detector surface can be seen. c) The beam path length measurement based on the end surface of the GRIN lens and the scattered light of the detector screen using this image, is shown.

detected on a 2D plane at the trap center. The beam delivery optics are clamped, and using translation stages can be aligned to the center of the trap electrodes by detection of the plate. This method allows each beam to be individually aligned and characterised.

The beam delivery alignment starts by mounting the delivery feedthrough into a 45° clamping stage. This is designed to clamp the top part of the feedthrough tube and the V-groove, housing the lensing optics and securing the fiber at 45°. This mount stabilises the assembly during insertion into the swagelok and allows for mounting to the translation stages required for alignment. The beam delivery assemblies are inserted back to front into the swagelok with the furcation tube cleaned prior to insertion. Once mounted in the swagelok a clamp is used to hold the feedthrough tube on the atmosphere side of the swagelok. This is equipped with a linear translation stage to allow for fine adjustment

of the feedthrough tube height as to ensure the fiber is never in too much tension or to slack. The translation stage is secured on the V-groove clamp and the connecting wire is cut and removed as well as the vacuum side clamp. The beam delivery V-groove is now free to be aligned to the base plane.

The camera aligned to the oven center is used to align the detector screen to the electrode center. The front camera is parallel to the detector plate and detects the scattered beam. A further camera parallel to the mounting plane is used to gauge the distance of the beam from the lens, allowing the waist position of the beam to be accurately aligned.

The screen is a cleaved and etched piece of PCB with a substrate thickness of < 400 μm. The surface roughness made for a good scattering surface. The PCB is aligned using a three axis linear translation stage whereby the front surface using the top camera is aligned to the electrode center.

For each delivery beam the used frequency is coupled into the single mode fiber. The beam propagates to the screen, where the front camera picks up the scattered profile. A mask overlay is used on the image indicating the center of the electrodes. The beam is aligned to have a 30 μm waist at the trap center based on the assembly's beam profile measurement. This was chosen due to the error estimates. The errors in the screens position (± 7 μm), crossing point accuracy (± 2 μm), and anchor point accuracy (± 3 μm) the total error is ≈ 8 μm. A 30 μm waist gave a good overlap, while not comprising the background scatter rate.

The V-grooves are epoxied using a small application of degassed EPO-TEK® H21D. This was chosen, due to its high viscosity during cure, so it would not run and cause unwanted coverage. For the application, the V-grooves were translated directly off the surface and using a cleaned fiber a small amount of the epoxy was applied between the base and the V-groove. The restive heater was used to cure. During the curing process, small adjustments were made to maintain alignment. After curing, measurements were taken before and after the release of the clamp. This was to ensure that releasing the clamp did not interferer with the alignment. In some cases it did interfere and therefore the assembly had to be removed and a new assembly was mounted. To finish the setup, the shields were mounted around each fiber.

Due to the assembly environment, after the two delivery fibers were mounted, the flange holding the trap had to be rotated 180° to align the other two delivery fibers.

The dc electrode that spanned the trap V-groove was delicately placed using tweezers and held in place using a spring loaded pressure clamp. This was epoxied using degassed

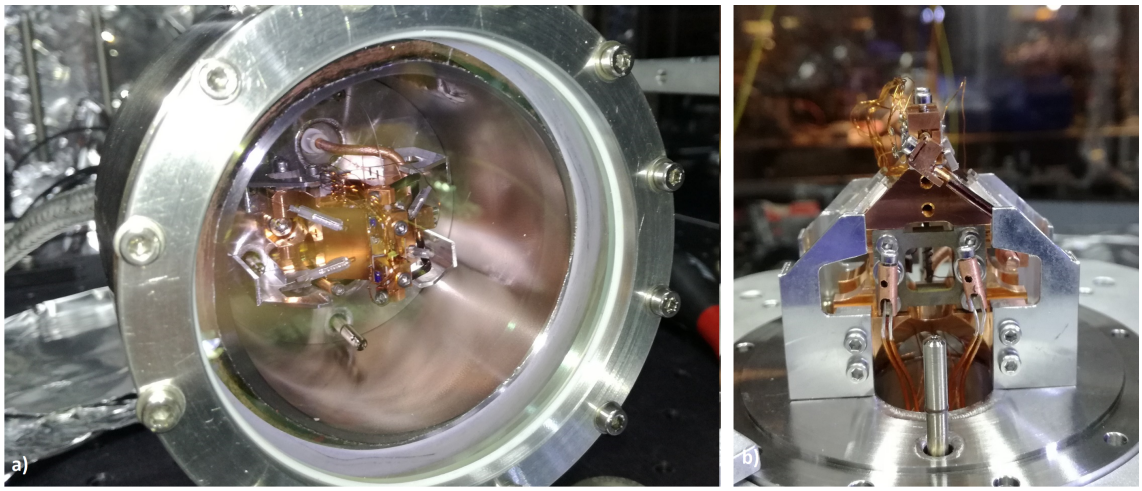

Figure 4.18: a) This shows the trap inside the test assembly vacuum chamber looking through the top window. b) The trap with its MM protectors removed and the oven mounted ready to be sealed up.

EPO-TEK® 301-2 and cured with the resistive heater. The electrode was designed to not interfere with the beams as they passed by, but the measurements for the background scatter were taken after mounting to ensure any interference was recorded. At this point it is worth highlighting that one of the mulit-mode fibers was snagged in alignment and consequently broke. Due to the system being able to function with just one MM fiber the build carried on.

The background scatter was measured as a function of power of the input beam. The scatter was found to be for UV1 2200-3000 cpsμW^{-1} and for UV2 720-1100 cpsμW^{-1}. The estimated SNR using just one collection fiber would be around 7.5 kcps meaning the signal to noise would be as little as 5 and as high as 22.

4.3.3.4 Oven and Closing

The oven was prepared before use. The oven consists of a tantalum tube pinched shut at one end. Tantalum wire is wound round the tube and spot-welded to it. Both ends of the tantalum wire are spot-welded to two washers. These act as electrical connection points. All the components making up the oven assembly are UVH washed and baked. Once assembled the oven is loaded with grated calcium and placed into a vacuum chamber. This chamber allows the oven to be fired and is pumped down under a roughing pump backed by a turbo pump. The oven is fired several times in vacuum to burn off any oxide formed. The oven remains pumped down in vacuum until needed.

The oven is mounted to the trap and electrically hooked up via two custom barrel

Figure 4.19: The trap before sealing up.

connectors. The mounting of the oven and sealing of the vacuum chamber needs to be done within a few hours to ensure the calcium does not over oxides.

To ease characterisation of the trap, it was mounted in a test chamber. The test chamber has a large optical window allowing each beam's power to be detected as well as having the ability to input beams if needed. The chamber was sealed using a gold wire seal and pumped down attached to a pumping station.

Chapter 5

Conclusion and outlook

The main focus of this thesis was to develop a highly compact ion trap and laser system to be used within a portable optical clock. The clock being developed clock is based on a single $^{40}Ca^{+}$ ion. Using a single ion has allowed us to benefit from its simple operation and more compact form factor compared to portable clocks based on atoms[32, 69, 70, 71].

By integrating fiberoptics directly into the trapping geometry a highly compact trap was realised. The trap, being formed with integrated large core multimode fibers housed directly into the trapping electrodes, can capture over two percent of the solid angle of the ions fluorescence without destabilising the trap. The monolithic beam delivery achieved alignment to the geometric trap center within an error of eight micrometers. This, with a beam width of 30 μm, ensured that the beam paths would overlap with the ion position with sufficient power to perform all the needed processes. This alignment was achieved with less than 10 mm of free space beam propagation per input, making the trap more vibration insensitive than a windowed ion trap. The use of gold coated copper trap electrodes with alumina spacers will reduce previous heating effects caused by stainless steel electrodes and macor spacers. The novel fiberoptic feedthroughs have allowed the vacuum system to be tightly fitted around the trapping structure, making the trap occupy less than two litres of volume. The current system is sealed and pumped by a large scale vacuum system made for ease of test. This system is in a state ready to begin testing. The next step is to perform the loading and ion trapping with the lab based laser systems. This will allow the needed frequencies to be calibrated and trap drive parameters measured. Next the system can be driven by the portable laser system and driven with our portable trap drive solution. Once the system is understood the system can be sealed with the finished low volume vacuum chamber and pumping solution.

$^{40}Ca^{+}$ only requires a total of six lasers: loading (423 nm + 375 nm), cooling (397

nm + 866 nm), clock state probing (729 nm), state detection (397 nm + 866 nm) and quenching (854 nm). This work has progressed all the needed laser except the probe/clock laser. The use of new commercially available fiberoptic integrated components along with highly stable DBR and micro cavity ECDL lasers has allowed this highly compact system to be realised. A system that occupies just four litres and has been shown to be able to trap and cool a single ion without stabilised feedback. One missing component in the laser system is the shutters needed for gating each laser. These shutters are required to be high speed (kHz extinction times), highly compact (fit within the volume of the laser system), low power consumption with extinction ratio greater than 80 dB. Preliminary work was done utilising a shutter design by Professor Keller and carried out by myself. This shutter utilised spliced fiber optic assemblies utilising a GRIN fiber section to lens the divergent profile from a single mode fiber. A pair of these GRIN fiber assemblies were coupled to create a narrow free space waist between the two assemblies. The assemblies were separated by a $\approx$ 800 um with a narrow waist of 13 um (FWHM). At the waist a blade attached to canter-leaver which was driven by piezoelectric actuator was aligned. This acted to gate the coupling when driven. Preliminary results showed extinction ratios of $>$ 85 dB and shutter speeds in the low kHz range. Unfortunately due to the unreliable formation of the GRIN fiber assemblies this work was discontinued. The GRIN lens assemblies shown in 4.2.1.2 could be used and the shutter could be revisited with a better outcome.

The ongoing work developing the autonomous control electronics needed to control the clock is progressing. Several key electronic boards are already under test (Laser driver board, USB connection board). Two different trap drives are in the position to be tested. My work on the development of a self resonating circuit driving at 24.6 MHz magic wavelength for $^{40}Ca^{+}$ was based on the work by Jao Y et al[72]. The drive was shown to achieve resonance at 21 MHz, driving a capacitor acting as the trap with room for tuning to the needed 24.6 MHz. A Q factor of $\approx$ 14 was measured and theoretically this would be enough to drive the trap. This needs testing with the real system to see if the quality factor is good enough or if the noise possesses a significant impact in driver quality resulting in unwanted broadening and shifts. The other drive solution designed by Professor Keller utilises a direct digital synthesis chip and amplifier. Future work on the intelligence of electronic control system to drive the needed loading profiles, cooling, interrogation, shift measurement and compensation schemes, and error readout.

Ongoing work on the clock laser in collaboration with the National Physics Laboratory

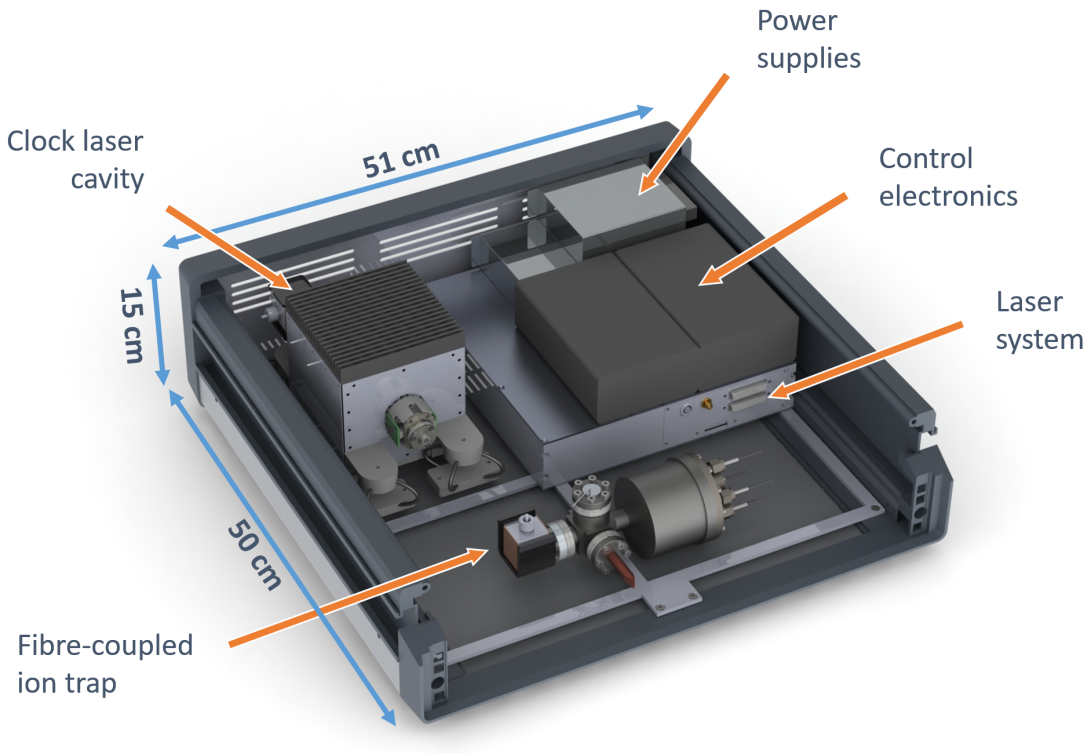

Figure 5.1: A spatial representation of the key components in the 4U rack mounted unit. Designed by Dr Gonzalvo

(NPL) will soon see a highly portable ultra stable laser based on NPLs force insensitive cube cavity[29]. This highly compact cavity and laser system will bridge the gap between portability and stability allowing this compact optical atomic clock to be created.

All of this past, present and future work will allow the formation of a portable optical clock based on a single $^{40}Ca^{+}$ ion. This truly portable envisioning all within a rack mounted unit of 4U (see figure 5.1).

The work done in this thesis will contribute to the formation of an even smaller generation of portable ion clocks. These clocks could open up new opportunities for navigation, communication, and scientific research bringing new technologies and understanding. Perhaps progressing humanity even if it is by a second in the age of the universe.

Bibliography

[1] R. Godun, "Trapped ion optical clocks." `http://empir.npl.co.uk/oc18/wp-content/uploads/sites/13/2018/09/1-Godun-Ion-Clocks_v2.pdf`, Last accessed June 2020. Cited on ix, 4

[2] W. J. Riley, *Handbook of frequency stability analysis*. U.S. Dept. of Commerce, National Institute of Standards and Technology, 2008. Cited on ix, 5, 6

[3] P. Gill, H. Margolis, A. Curtis, H. Klein, S. Lea, S. Webster, and P. Whibberley, "Optical atomic clocks for space," 11 2008. Cited on ix, 4, 5, 7

[4] W. Günther, V. N. Gheorghe, and F. G. Major, *Charged Particle Traps II Applications*. Springer Berlin, 2013. Cited on ix, 14, 15

[5] W. J. H. Andrewes, "A chronicle of timekeeping." `https://www.scientificamerican.com/article/a-chronicle-of-timekeeping-2006-02/`, Last accessed June 2020. Cited on 2

[6] N. F. Ramsey, "History of early atomic clocks," *Metrologia*, vol. 42, no. 3, pp. S1–S3, 2005. Cited on 2

[7] W. Thomson and P. G. Tait, *Treatise on Natural Philosophy*, vol. 1 of *Cambridge Library Collection - Mathematics*. Cambridge University Press, 2 ed., 2009. Cited on 2

[8] N. F. Ramsey, "History of atomic clocks," *Journal of Reaserch*, vol. 88, no. 5, 1983. Cited on 2

[9] J. V. L. Parry and L. Essen, "An atomic standard of frequency and time interval: A cæsium resonator," *Nature*, vol. 176, no. 4476, pp. 280–282, 1955. Cited on 2

[10] "The international system of units (si) 9th edition." `https://www.bipm.org/en/publications/si-brochure`, Last accessed June 2020. Cited on 2

[11] M. Abgrall, B. Chupin, L. De Sarlo, J. Guéna, P. Laurent, Y. Le Coq, R. Le Targat, J. Lodewyck, M. Lours, P. Rosenbusch, G. D. Rovera, and S. Bize, "Atomic fountains and optical clocks at syrte: Status and perspectives," *Comptes rendus. Physique*, vol. 16, no. 5, pp. 461–470, 2015. Cited on 3

[12] J. Levine, "Introduction to time and frequency metrology," *Review of Scientific Instruments*, vol. 70, no. 6, pp. 2567–2596, 1999. Cited on 3

[13] "International reference time scales." `https://www.bipm.org/en/time-metrology`, Last accessed June 2020. Cited on 3

[14] T. H. Maiman, "Stimulated optical radiation in ruby," *Nature (London)*, vol. 187, no. 4736, pp. 493–494, 1960. Cited on 3

[15] W. Tuma and C. J. van der Hoeven, "Helium-neon laser stabilized on iodine: design and performance," *Applied optics (2004)*, vol. 14, no. 8, pp. 1896–1897, 1975. Cited on 3

[16] W. G. Schweitzer, Jr, E. G. Kessler, Jr, R. D. Deslattes, H. P. Layer, and J. R. Whetstone, "Description, performance, and wavelengths of iodine stabilized lasers," *Applied optics (2004)*, vol. 12, no. 12, pp. 2927–2938, 1973. Cited on 3

[17] G. R. Hanes, K. M. Baird, and J. Deremigis, "Stability, reproducibility, and absolute wavelength of a 633-nm he-ne laser stabilized to an iodine hyperfine component," *Applied optics (2004)*, vol. 12, no. 7, pp. 1600–1605, 1973. Cited on 3

[18] W. Paul, "Electromagnetic traps for charged and neutral particles," *Reviews of modern physics*, vol. 62, no. 3, pp. 531–540, 1990. Cited on 3

[19] "The nobel prize in physics 1989." `https://www.nobelprize.org/prizes/physics/1989/summary/`, Last accessed June 2020. Cited on 3, 12

[20] "The nobel prize in physics 2012." `https://www.nobelprize.org/prizes/physics/2012/summary/`, Last accessed June 2020. Cited on 3

[21] P. A. Franken, A. E. Hill, C. W. Peters, and G. Weinreich, "Generation of optical harmonics," *Phys. Rev. Lett.*, vol. 7, pp. 118–119, Aug 1961. Cited on 3, 9

[22] T. Fortier and E. Baumann, "20 years of developments in optical frequency comb technology and applications," *Communications physics*, vol. 2, no. 1, pp. 1–16, 2019. Cited on 4, 9

[23] "The nobel prize in physics 2005." `https://www.nobelprize.org/prizes/physics/2005/summary/`, Last accessed June 2020. Cited on 4

[24] S. M. Brewer, J.-S. Chen, A. M. Hankin, E. R. Clements, C. W. Chou, D. J. Wineland, D. B. Hume, and D. R. Leibrandt, "$27al^+$ quantum-logic clock with a systematic uncertainty below 10^{-18}," *Physical review letters*, vol. 123, no. 3, pp. 033201–033201, 2019. Cited on 4, 9

[25] F. Riehle, "Towards a redefinition of the second based on optical atomic clocks," *Comptes rendus. Physique*, vol. 16, no. 5, pp. 506–515, 2015. Cited on 4

[26] E. Peik, T. Schneider, and C. Tamm, "Laser frequency stabilization to a single ion," *Journal of physics. B, Atomic, molecular, and optical physics*, vol. 39, no. 1, pp. 145–158, 2006. Cited on 5

[27] D. Świerad, S. Häfner, S. Vogt, B. Venon, D. Holleville, S. Bize, A. Kulosa, S. Bode, Y. Singh, K. Bongs, E. M. Rasel, J. Lodewyck, R. Le Targat, C. Lisdat, and U. Sterr, "Ultra-stable clock laser system development towards space applications," *Scientific reports*, vol. 6, no. 1, pp. 33973–33973, 2016. Cited on 6

[28] S. A. Webster, M. Oxborrow, S. Pugla, J. Millo, and P. Gill, "Thermal-noise-limited optical cavity," *Physical review. A, Atomic, molecular, and optical physics*, vol. 77, no. 3, 2008. Cited on 6

[29] S. Webster and P. Gill, "Force-insensitive optical cavity," *Optics letters*, vol. 36, no. 18, pp. 3572–3574, 2011. Cited on 6, 97

[30] E. D. Black, "An introduction to pound–drever–hall laser frequency stabilization," *American journal of physics*, vol. 69, no. 1, pp. 79–87, 2001. Cited on 6

[31] Q. F. Chen, A. Nevsky, and S. Schiller, "Locking the frequency of lasers to an optical cavity at the 1.61017 relative instability level," *Applied physics. B, Lasers and optics*, vol. 107, no. 3, pp. 679–683, 2012. Cited on 8

[32] N. Poli, M. Schioppo, S. Vogt, S. Falke, U. Sterr, C. Lisdat, and G. M. Tino, "A transportable strontium optical lattice clock," vol. 117, no. 4, pp. 1107–1116, 2014. Cited on 8, 95

[33] B. J. Bloom, T. L. Nicholson, J. R. Williams, S. L. Campbell, M. Bishof, X. Zhang, W. Zhang, S. L. Bromley, and J. Ye, "An optical lattice clock with accuracy and stability at the 10(-18) level," *Nature (London)*, vol. 506, no. 7486, pp. 71–75, 2014. Cited on 8

[34] S. Falke, N. Lemke, C. Grebing, B. Lipphardt, S. Weyers, V. Gerginov, N. Huntemann, C. Hagemann, A. Al-Masoudi, S. Häfner, S. Vogt, U. Sterr, and C. Lisdat, "A strontium lattice clock with 3 10 17 inaccuracy and its frequency," *New journal of physics*, vol. 16, no. 7, p. 073023, 2014. Cited on 8

[35] I. Ushijima, M. Takamoto, M. Das, T. Ohkubo, and H. Katori, "Cryogenic optical lattice clocks," *Nature photonics*, vol. 9, no. 3, pp. 185–189, 2015. Cited on 8

[36] P. Dubé, A. A. Madej, and B. Jian, "$sr+$ single ion clock," in *Journal of physics. Conference series*, vol. 723, p. 12018, 2016. Cited on 8, 13

[37] N. Huntemann, C. Sanner, B. Lipphardt, C. Tamm, and E. Peik, "Single ion atomic clock with $3x10^{-18}$ systematic uncertainty," 2016. Cited on 8, 13

[38] "Galileo's clocks." `https://www.esa.int/Applications/Navigation/Galileo/Galileo_s_clocks`, Last accessed June 2020. Cited on 10

[39] "Galileo starts to tell utc, the world's time." `https://www.esa.int/Applications/Navigation/Galileo_starts_to_tell_UTC_the_world_s_time`, Last accessed June 2020. Cited on 10

[40] "Delivering 5g 'right on time'." `https://newsroom.bt.com/delivering-5g-right-on-time/`, Last accessed June 2020. Cited on 10

[41] N. Seth and F. S. Kazi, "Vulnerability of intelligent electronic devices (ied) to time synchronization spoofing in power grid and jamming of gnss receiver," in *2018 IEEE 8th Power India International Conference (PIICON)*, pp. 1–6, IEEE, 2018. Cited on 10

[42] Y. Wang, J.-M. Hao, W.-P. Liu, and X. Wang, "Dynamic evaluation of gnss spoofing and jamming efficacy based on game theory," *IEEE access*, vol. 8, pp. 13845–13857, 2020. Cited on 10

[43] A. D. Ludlow, "An optical clock to go," *Nature physics*, vol. 14, no. 5, pp. 431–432, 2018. Cited on 10

[44] P. K. Ghosh, *Ion traps*. Clarendon press, 1995. Cited on 12

[45] C. J. Foot, *Atomic Physics*. 2005. Cited on 13, 18

[46] H. Häffner, C. Roos, and R. Blatt, "Quantum computing with trapped ions," *Physics reports*, vol. 469, no. 4, pp. 155–203, 2008. Cited on 13

[47] W. K. Hensinger, S. Olmschenk, D. Stick, D. Hucul, M. Yeo, M. Acton, L. Deslauriers, C. Monroe, and J. Rabchuk, "T junction ion trap array for two dimensional ion shuttling, storage, and manipulation," *Applied physics letters*, vol. 88, no. 3, pp. 034101–034101–3, 2006. Cited on 13

[48] D. Leibfried, R. Blatt, C. Monroe, and D. Wineland, "Quantum dynamics of single trapped ions," *Reviews of modern physics*, vol. 75, no. 1, pp. 281–324, 2003. Cited on 14

[49] T. Hänsch and A. Schawlow, "Cooling of gases by laser radiation," *Optics communications*, vol. 13, no. 1, pp. 68–69, 1975. Cited on 17

[50] D. J. Wineland and H. G. Dehmelt, "Principles of the stored ion calorimeter," *Journal of applied physics*, vol. 46, no. 2, pp. 919–930, 1975. Cited on 17

[51] D. J. Wineland, R. E. Drullinger, and F. L. Walls, "Radiation-pressure cooling of bound resonant absorbers," *Physical review letters*, vol. 40, no. 25, pp. 1639–1642, 1978. Cited on 17

[52] A. Urvoy, Z. Vendeiro, J. Ramette, A. Adiyatullin, and V. Vuletić, "Direct laser cooling to bose-einstein condensation in a dipole trap," *Physical review letters*, vol. 122, no. 20, pp. 203202–203202, 2019. Cited on 17

[53] L. Mandel, *Optical coherence and quantum optics*. C.U.P., 1995. Cited on 19

[54] J. Bernard, L. Marmet, and A. Madej, "A laser frequency lock referenced to a single trapped ion," *Optics Communications*, vol. 150, pp. 170–174, 05 1998. Cited on 28

[55] M. Chwalla, J. Benhelm, K. Kim, G. Kirchmair, T. Monz, M. Riebe, P. Schindler, A. S. Villar, W. Hänsel, C. F. Roos, R. Blatt, M. Abgrall, G. Santarelli, G. D. Rovera, and P. Laurent, "Absolute frequency measurement of the $40ca+4s(2)s_(1/2)-3d(2)d_(5/2)$ clock transition," *Physical review letters*, vol. 102, no. 2, pp. 023002–023002, 2009. Cited on 28

[56] C. F. Roos, M. Chwalla, K. Kim, M. Riebe, and R. Blatt, "'designer atoms' for quantum metrology," *Nature (London)*, vol. 443, no. 7109, pp. 316–319, 2006. Cited on 28

[57] P. Dubé, A. A. Madej, J. E. Bernard, L. Marmet, J.-S. Boulanger, and S. Cundy, "Electric quadrupole shift cancellation in single-ion optical frequency standards," *Physical review letters*, vol. 95, no. 3, pp. 033001–033001, 2005. Cited on 28

[58] D. J. Berkeland, J. D. Miller, J. C. Bergquist, W. M. Itano, and D. J. Wineland, "Minimization of ion micromotion in a paul trap," *Journal of applied physics*, vol. 83, no. 10, pp. 5025–5033, 1998. Cited on 28, 29

[59] F. Diedrich, J. Bergquist, W. Itano, and D. Wineland, "Laser cooling to the zero-point energy of motion," *Physical review letters*, vol. 62, no. 4, pp. 403–406, 1989. Cited on 29

[60] Y. Huang, H. Guan, W. Bian, L. Ma, K. Liang, T. Li, and K. Gao, "A comparison of two $40ca+$ single-ion optical frequency standards at the 5 x 1017 level and an evaluation of systematic shifts," *Applied physics. B, Lasers and optics*, vol. 123, no. 5, pp. 1–18, 2017. Cited on 30

[61] P. Zhang, J. Cao, H.-l. Shu, J.-b. Yuan, J.-j. Shang, K.-f. Cui, S.-j. Chao, S.-m. Wang, D.-x. Liu, and X.-r. Huang, "Evaluation of blackbody radiation shift with temperature-associated fractional uncertainty at 1018 level for 40ca+ ion optical clock," *Journal of physics. B, Atomic, molecular, and optical physics*, vol. 50, no. 1, p. 15002, 2017. Cited on 30

[62] N. R. Seymour-Smith, "Ion-trap cavity qed system for probabilistic entanglement," 2012. Cited on 50

[63] J. Noda, K. Okamoto, and Y. Sasaki, "Polarization-maintaining fibers and their applications," *Journal of lightwave technology*, vol. 4, no. 8, pp. 1071–1089, 1986. Cited on 61

[64] H. Takahashi, A. Wilson, A. Riley-Watson, F. Oručević, N. Seymour-Smith, M. Keller, and W. Lange, "An integrated fiber trap for single-ion photonics," *New Journal of Physics*, vol. 15, p. 053011, may 2013. Cited on 62, 63, 65

[65] M. Harlander, M. Brownnutt, W. Hänsel, and R. Blatt, "Trapped-ion probing of light-induced charging effects on dielectrics," *New journal of physics*, vol. 12, no. 9, p. 093035, 2010. Cited on 63

[66] G. Meng, Y. Liang, S. Sarsfield, W.-c. Jiang, R. Lu, J. T. Dudman, Y. Aponte, and N. Ji, "High-throughput synapse-resolving two-photon fluorescence microendoscopy for deep-brain volumetric imaging in vivo," *eLife*, vol. 8, 2019. Cited on 64

[67] M. Chen, D. Wen, S. Huang, S. Gui, Z. Zhang, J. Lu, and P. Li, "Laser speckle contrast imaging of blood flow in the deep brain using microendoscopy," *Optics letters*, vol. 43, no. 22, p. 5627, 2018. Cited on 64

[68] Y.-H. Seo, K. Hwang, and K.-H. Jeong, "1.65 mm diameter forward-viewing confocal endomicroscopic catheter using a flip-chip bonded electrothermal mems fiber scanner," *Optics express*, vol. 26, no. 4, p. 4780, 2018. Cited on 64

[69] D. T. Swierad, *Stable and ultra-stable laser systems for a mobile strontium optical clock*. PhD thesis. Cited on 95

[70] B. O. Kock, *Magneto optical trapping of strontium for use as a mobile frequency reference*. PhD thesis, 2013. Cited on 95

[71] L. L. Smith, *A transportable strontium optical lattice clock towards space*. PhD thesis. Cited on 95

[72] Y. Y. Jau, F. M. Benito, H. Partner, and P. D. D. Schwindt, "Low power high performance radio frequency oscillator for driving ion traps," *Review of Scientific Instruments*, vol. 82, no. 2, pp. 023118–023118–5, 2011. Cited on 96